CONTENTS

ABSTRACTS

Mirosław Bocian, Jerzy Kaleta, Daniel Lewandowski, Michał Przybylski
Design Concept of Test Stand for Determining Properties of Magnetorheological Elastomers

Magnetorheological elastomers (MRE) are "SMART" materials that change their mechanical properties under influence of magnetic field. Thanks to that ability it is possible to create adaptive vibration dampers based on the MRE. To test vibration damping abilities of this material special test stand is required. This article presents design concept for such test stand with several options of testing.

Janette Brezinová, Anna Guzanová, Dagmar Draganovská, Marián Egri
Assessment Tribological Properties of Coatings Applied by HVOF Technology

In this article, the attention is paid to the HVOF (High Velocity Oxygen Fuel) thermal spraying method by which the progressive coatings are applied on basic material C15E (STN 412020). These coatings are based on C-17CO, WC-CO-Cr and Cr3C2-25NiCr. There was made determination of the chemical composition of the coatings and assessment of coatings quality - adhesion, microhardness, porosity and wear resistance at room temperature (21°C) and also at operational elevated temperature (900°C). Results of adhesive wear showed high quality of all evaluated coatings and their suitability to extreme tribological conditions.

Andrzej Kaczyński
An Anticrack in Transversely Isotropic Space

An absolutely rigid inclusion (anticrack) embedded in an unbound transversely isotropic elastic solid with the axis of elastic symmetry normal to the inclusion plane is considered. A general method of solving the anticrack problem is presented. Effective results have been achieved by constructing the appropriate harmonic potentials. With the use of the Fourier transform technique, the governing system of two-dimensional equations of Newtonian potential type for the stress jump functions on the opposite surfaces of the inclusion is obtained. For illustration, a complete solution to the problem of a penny-shaped anticrack under perpendicular tension at infinity is given and discussed from the point of view of material failure.

Cezary Kownacki
Real Flight Demonstration of Pitch and Roll Control for UAV Canyon Flights

The paper presents results of an experiment prepared to validate the autonomous control of obstacle avoidance designed for a micro UAV to fly in urban canyons. The idea of the obstacle avoidance assumes usage of two miniature laser rangefinders responsible for obstacle detection and range measurement. Measured ranges from obstacles placed on both sides of UAV can be used to simultaneous control of desired roll and pitch angles. Such combination of controls allows achieving high agility of UAV, because during a maneuver of obstacle avoidance UAV can make a turn and climb at the same time. In the experiment, controls of roll and pitch angles were verified separately to ensure high reliability of results and clearance of UAV behavior in the real flight. Because of lack of appropriate objects, which can be used as obstacles, laser rangefinders were directed vertically to the ground instead of the original horizontal configuration. So sensors determine ranges from the ground during a descent flight of UAV, and if their values are lower than defined threshold, it could be interpreted as obstacle detection. The experiment results present UAV behavior adequate to designed controls of roll and pitch angle. The vehicle turns in the opposite direction to the sensing axis of laser rangefinder detecting an obstacle and starts climbing when both sensors detect obstacles at the same range below the threshold.

Magdalena Łępicka, Małgorzata Grądzka-Dahlke
Effect of Heat Treatment and Plasma Nitriding on Corrosion Resistance of X90CrMoV18 Martensitic Stainless Steel

Reliability and durability assurance poses a serious challenge for surgical instruments manufacturers. Hard working conditions, such as intermittent contact with body fluids and hard bone tissues, as well as necessity to undergo frequent sterilisation processes, induce constant research into solutions capable of ensuring high wear resistance while maintaining satisfactory imperviousness to corrosion. Plasma nitriding is marked as the modern corrosion resistance improving method suitable for surgical instruments steels. The paper presents findings from the heat treated and plasma nitrided AISI 440B (PN EN or DIN X90CrMoV18) steel corrosion resistance studies. Three conventionally heat treated (quenched with tempering in 250, 390 or 605°C) and three additionally plasma nitrided in N2:H2 reaction gas mixture (50:50, 35:65 and 20:80 ratio, respectively) specimens groups were examined. Furthermore, the authors evaluated the effect of machining - polishing and sandblasting - on investigated steel corrosion resistance. Microscopic observations and electrochemical corrosion tests were performed using a variety of analytical techniques. Results showed that, in comparison to conventional heat treatment, plasma nitriding of 440B stainless steel does not significantly affect its corrosive characteristics as far as the uniform nitride layer over the entire detail surface is obtained. The layer heterogeneity results in intensification of corrosion processes, making the material even more susceptible to corrosion than after conventional heat treatment, and contributing to severe, visible even with the unaided eye damages development.

Łukasz Mazurkiewicz, Jerzy Małachowski, Krzysztof Damaziak, Paweł Baranowski, Paweł Gotowicki
Identification of Layers Distribution in the Composite Coupon Using Finite Element Method and Three Point Bending Test

The main objective of the study is to develop experimentally validated FE model and perform numerical analysis of layered composites made by hand lay-up techniques during tension and bending test. The research object is glass - polyester laminate made of four unidirectional layers. In order to validate the numerical models experimental test were performed. Due to the very different stiffness modulus in tension and bending loading the material properties obtained from standard test are not suitable to apply in numerical model. Significantly different behaviour compared to experimental test was obtained for tree point bending where the numerical model becomes too stiff. Simple coupons, relatively easy to manufacture presented in the paper have very low quality. The differences in actual and theoretical bending stiffness (obtained from tension stiffness) exceed 70%. In order to represent the actual structure the layers of the composite were divided by resin layers and also additional resin layer at the top and bottom of the model were defined. Single stage optimization process was used to adjust the material layout. After layer set-up modification very significant improvement can be seen for flexural behaviour.

Krzysztof Nowak
Dependence of Creep Failure Probability on the Length of Metallic Specimens

The occurrence of statistical size effect is considered for damage in creep conditions. The numerical and experimental analysis have been performed. The obtained results are ambiguous. Numerical models confirm the scale effect which can be statistical or deterministic one. But this effect has no experimental verification. It may suggest that the weakest link model cannot be applied in creep conditions. Explanation of this needs further investigations.

Yuriy Pyryev, Zofia Maria Piętak
The Analysis of Tribological Processes in the Inking Unit of the Offset Printing Machine

In this paper is proposed the mathematical description of the temperature distribution resulting from the friction between the two inking rollers (one of which is made off steel and the second one has elastic layer) in the offset printing machine. So-called in printing industry steel vibrator roller perform simultaneously rotary and reciprocating motion. This reciprocating motion is the main source of the heat generation. Using the Laplace transform method for heat conduction equations with boundary conditions taking into account the real processes taking place in the inking unit in contact area we obtained and analyzed the solution that could be useful for determination and regulation of parameters in order to decrease time of process stabilization.

Jerzy Rojek, Szymon Nosewicz, Katarzyna Pietrzak, Marcin Chmielewski
Simulation of Powder Sintering Using a Discrete Element Model

This paper presents numerical simulation of powder sintering. The numerical model introduced in this work employs the discrete element method which assumes that material can be modelled by a large assembly of discrete elements (particles) of spherical shape interacting among one another. Modelling of sintering requires introduction of the cohesive interaction among particles representing inter-particle sintering forces. Numerical studies of sintering have been combined with experimental studies which provided data for calibration and validation of the model. In the laboratory tests evolution of microstructure and density during sintering have been studied. Comparison of numerical and experimental results shows a good performance of the numerical model developed.

Bogdan Sapiński, Marcin Szczęch
CFD Model Of A Magnetorheological Fluid In The Squeeze Mode

The study briefly outlines a CFD model of a magnetorheological (MR) fluid operated in squeeze mode with a constant interface area using the CFD (Computational Fluid Dynamics) approach. The underlying assumption is that the MR fluid is placed between two surfaces of which at least one can be subject to a prescribed displacement or a force input. The widely employed Bingham model, which fails to take into account the yield stress variations depending on the height of the gap, has been modified. Computation data obtained in the ANSYS CFX environment are compared with experimental results.

DESIGN CONCEPT OF TEST STAND FOR DETERMINING PROPERTIES OF MAGNETORHEOLOGICAL ELASTOMERS

Mirosław BOCIAN*, Jerzy KALETA*, Daniel LEWANDOWSKI*, Michał PRZYBYLSKI*

*Institute of Material Science and Applied Mechanics, Wroclaw University of Technology,
ul. Smoluchowskiego 25, 50-370 Wrocław, Poland

miroslaw.bocian@pwr.wroc.pl, jerzy.kaleta@pwr.wroc.pl, daniel.lewandowski@pwr.wroc.pl, michal.przybylski@pwr.wroc.pl

Abstract: Magnetorheological elastomers (MRE) are "SMART" materials that change their mechanical properties under influence of magnetic field. Thanks to that ability it is possible to create adaptive vibration dampers based on the MRE. To test vibration damping abilities of this material special test stand is required. This article presents design concept for such test stand with several options of testing.

Key words: MRE, Vibration Damping, SMART Materials, Halbach Array

1. INTRODUCTION

In the modern world there is a great potential for the effective vibration damping. All of us are exposed to vibrations all of the time. Source of vibrations can be anything starting from small electromechanical equipment through all kind of transportation systems and heavy machinery, ending on natural causes like earthquake. All vibrations, regardless its source, can be harmful if they last long enough. The stronger the vibration the smaller time they need to do the damage, for example combustion engines vibrates constantly while vehicle they operate last years undamaged comparing to the Bucket-wheel excavators at open-pit mines that frequently get damaged due to strong vibrations they experience.

Group of the modern materials presenting promising properties in terms of vibration damping are magnetorheological elastomers (MRE). Those are materials that change their mechanical properties under influence of external magnetic field (Kaleta et al., 2011). They are categorized as magneto-mechanical materials, often referred as "SMART" magnetic materials. As MRE presents changing mechanical properties depending on magnetic field the test stand for determining their vibration damping properties have to be adjusted to the need of use variable magnetic field.

The article presents the design concept for the test stand for determining damping and stiffness properties of magnetorheological elastomers that can work with several types of excitation and measurement methods.

2. TEST METHODOLOGY

The idea of the test stand is based on the one degree of freedom system presented in Fig. 1. Such system is very useful in testing vibration damping as there is just one damping element and all the results refers to it. Thanks to such approach effects not related to tested object can be neglected as they do not interfere with actual results on the frequency response function (FRF).

Except the tested element test stand requires method for excitation of the vibrations, response gathering device and signal processor that will collect input and output data of the vibrating test stand. For vibration excitation impact hammer or shaker can be used. In the case of desired test stand impact hammer has advantage over the shaker as it is fast and easy to use technique that does not require variable loading of the system to be applied. The transducer is the universal device used to collect acceleration signal from both impact hammer and shaker excitation. The signal processor have to gather data but also process it in terms of FRF and phase shift angle so the output data will be reliable and easy to analyze. HP 35665A Dynamic Signal Analyzer meets the requirements.

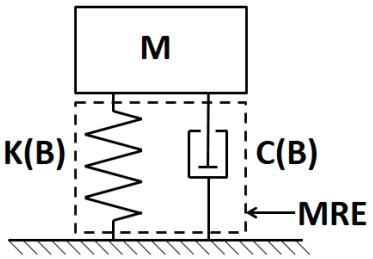

Fig. 1. One degree of freedom system where K(B) and C(B) are the MRE material

Frequency response function is necessary for the analysis of the properties of the system. On its base following parameters can be obtained: damping ratio ζ, structural damping ratio η, damping C and stiffness K. To calculate the damping ratio peak picking method is useful as it is based on the resonance presented in FRF (Olmos and Roesset, 2010). To obtain the value of the ζ it is necessary to find the frequency of the maximum value of the resonance and the frequencies corresponding to the values of $A_{max}/\sqrt{2}$. Using equation presented in Fig. 2 it is possible to get damping ratio of the system. To obtain structural damping ratio damping and stiffness resonance occurring in the FRF have to be approximated with use of the circle fit method. The Modified Least Square Method is very accurate and uses simple function, easy to implement in the software (Umbach and Jones, 2003).

On base of the approximated circle it is possible to get the desired values of η, C and K. Fig. 3 presents how structural damping can be obtained from the circle fitted to the experimental data.

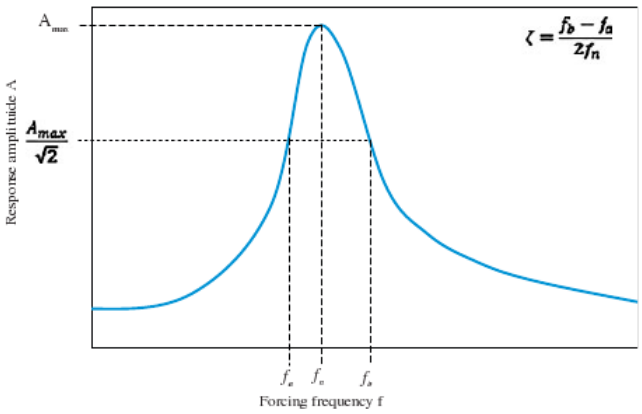

Fig. 2. Peak picking method for obtaining damping ratio of the system from the FRF (Umbach and Jones, 2003)

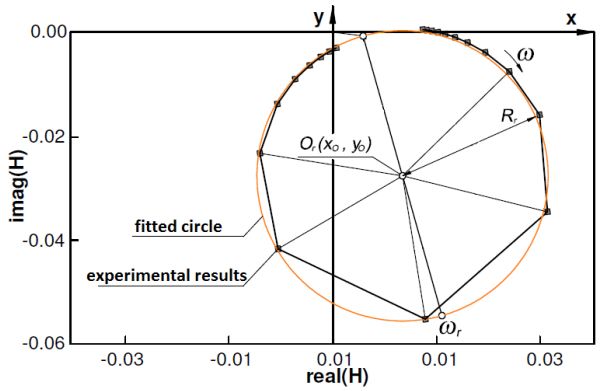

Fig. 3. The circle fit method for obtaining structural damping ratio, damping and stiffness of the system from the FRF (Maia, 1999), where O_r is a center, R_r is radius, ω_r is frequency of the resonsce, ω is increasing frequency of fitted circle

3. DESIGN CONCEPT OF THE TEST STAND

To design desired test stand some issues have to be taken into consideration to assure its proper work. First of all, as it was mentioned in previous section the test stand for determining properties of the MRE should have only one degree of freedom. Such situation happens only in the simulations and is used for simplification of the calculations. Real systems have many degrees of freedom, however this disadvantage can be overcome. Therefore the construction have to work as it would have only one degree of freedom with minimal reactions in other degrees of freedom.

Second important aspect of the test stand is that it have to be nonmagnetic as it will work with strong magnetic fields acting on the MRE material and on the construction of the test stand. Any magnetic element in the test stand that would be attracted or repelled by magnetic field generators would interfere with the test results, therefore the test stand have to be made out of nonmagnetic materials.

Third aspect that have to be considered is vibration isolation of the test stand, as external vibrations can interfere with the test results. The test stand should not require any specialized construction like floating floor that would mitigate the external vibrations originated out of the test stand.

3.1. Construction

The construction of the test stand should work as it has only one degree of freedom, therefore two plates placed one on top of another with tested material in between should work fine. Such solution will allow the MRE material to work in shear in the direction of the excitation (Giraudeua and Pierron, 2005). Such solution allows various setups of the MRE samples in the test stand. Thanks to such approach not only parameters connected with the material itself but also with shape, size and number of samples used in the experiment can be obtained. To mitigate external vibrations lower plate can be suspended on the elastic bands what should isolate the test stand from the vibrations not originated in the test stand. In such case test stand will behave as pendulum and during the experiment it will oscillate, therefore mass of whole system have to be big enough so the frequency of the oscillation will be below 1 Hz. The idea for such test stand is presented in the Fig. 4. The lower plate M1 would be hanged in the air to isolate it form the external vibrations and to minimalize effects of its own vibrations. Also the mass of plate M1 should be much greater than that of plate M2 to move part of the FRF corresponding to plate M1 toward zero what would separate peaks visible on frequency response function.

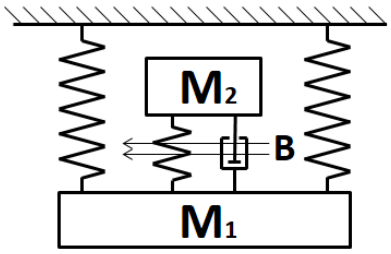

Fig. 4. Scheme of the concept of the test stand for determining damping of the magnetorheological elastomers, where M_1 is lower plate, M_2 is upper plate, B is magnetic field

The shape of the tested MRE should be cylindrical as such shape will allow to uniformly expose it to the magnetic field. Number of the test samples used simultaneously for testing depend on the need and can vary from one to many, however at least three test samples will guaranty stability of the upper plate M2 and will prevent it from rocking from side to side.

As the test stand will work in high magnetic field all elements have to be nonmagnetic, in such case stone (i.e.: granite or marble) would work perfect for both plates. In such case there would be no problem with obtaining high masses of both plates. All other elements of the test stand will have to be made out of other nonmagnetic and nonconductive materials as eddy currents can also effect the tests.

3.2. Magnetic field source

Magnetorheological elastomers require source of the variable magnetic field to work as adjustable material. The magnetic field

can be applied to the material using few approaches: magnetic coils, permanent magnets or controllable magnetic matrix. Magnetic field that will stimulate MRE material should be uniform in the area where material will work and easy to change. Permanent magnets does not meet those requirements on the other hand magnetic coils can create easy to change uniform field however they would have large dimensions if generated field would have to be more than couple of mT. The solution is magnetic matrix that is small and can generate magnetic field over 100 mT with possibility for easy adjustment. Fig. 5 presents various ring magnetic matrices known as Halbach arrays. Depending on the setup of magnets creating the array it can create different shape of magnetic field inside the ring.

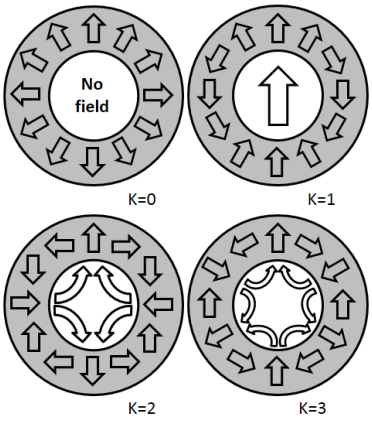

Fig. 5. Possible setups of round Halbach arrays that generate magnetic field in specyfic direction, where K=0, K=1, K=2, K=3 are types of magnet setups. K represents number of phases of the array

Fig. 6. Example of Halbach magnetic matrix with K=1

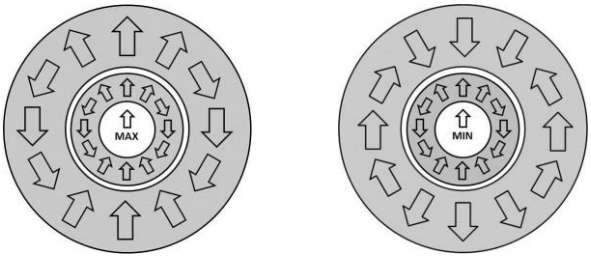

Fig. 7. Setup of magnets in double round Halbach array for obtaining minimum and maximum magnetic field inside of it

Fig. 6 presents an example of the round Halbach array with K=1. This specific array creates uniform magnetic field inside of it. However to have possibility to change the value of magnetic field inside the matrix there is an idea to place two or more round Halbach arrays around one another and rotate them around each other to change magnetic field inside (Choi and Yoo, 2008). In the two-ring Halbach array change of the angle of the outer element from 0° to 180° causes change from maximum to minimum value of the created magnetic field. To determine maximal and minimal values of magnetic field inside the double matrix simulation using FEMM software was created, Fig. 7 presents setup of magnets in double array.

Fig. 8 presents extreme positions of the magnetic matrix. FEMM software allows to create only 2D simulations therefore the device was simulated in most useful view which is from the top. Magnets used in the simulations were square 7x7 mm NdFeB N40 neodymium magnets, and the opening inside had diameter of 25 mm. The inner element was constructed out of 12 magnets and outer one out of 20 neodymium magnets. Simulation indicated that the maximum magnetic field that can be obtained using such system of magnets can create inside almost uniform magnetic field with maximum absolute value of about 650 mT and minimum of about 100 mT what gives a change in the value of the absolute magnetic field of 550 mT.

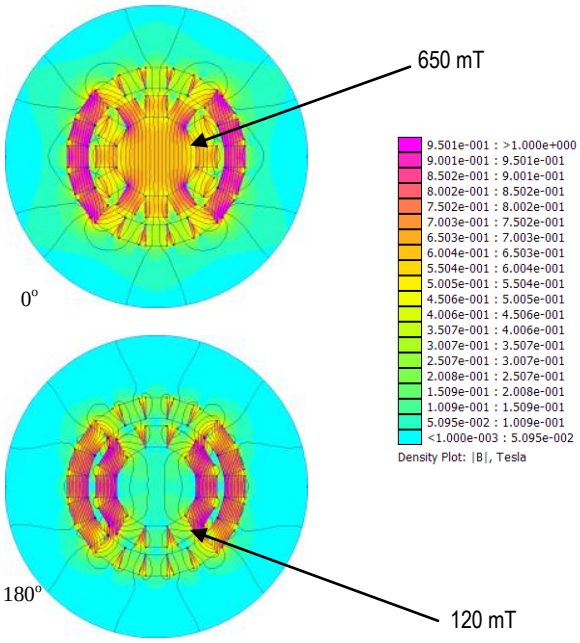

Fig. 8. Simulation of double Halbach magnetic matrix with outer part rotated with respect to the inner part what changes generated magnetic field

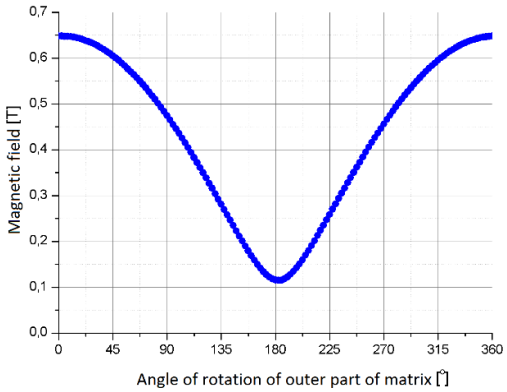

Fig. 9. Change of the magnetic field inside double Halbach matrix with the change of the angle of the outer element

The simulation was also performed for the change of the angle of the outer array by 2.5° and the values of the absolute mag-

netic field in tesla [T] in the center point was read. Graph in Fig. presents how changes the absolute value of magnetic field inside the double Halbach array with the change of the angle. In Fig. 9 is presented graph of the absolute value of magnetic field in the center of the double round Halbach array versus the angle of rotation of the outer part of the array.

3.3 Sketch of the test stand

On bases of the previous assumptions a sketch of the test stand was prepared. The sketch presents the setup of all of the elements and signals that will be present in the real test stand. Model presents two stone plates with MRE material placed in between them with round double Halbach arrays around them. At one end of the upper plate accelerometer is placed that will be collecting data from the upper plate, on the other side of that plate there is a place that will be excited using impact hammer. Both accelerometer and impact place are aligned and in the symmetry line of the setup. The double Halbach arrays that surround the MRE cylinders are placed on the bottom of the sample and on the top of the lower plate to ensure its vibrations will not interfere with the upper plates vibrations. The hanging of the test stand is presented only symbolically. Fig. 10 presents the model with the description of all the elements.

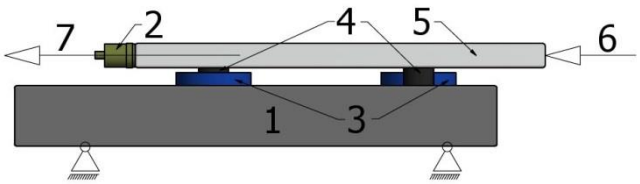

Fig. 10. Sketch of the test stand for determining properties of magnetorehological elastomers prepared using Autodesk Inventor software, where: 1 – lower plate; 2 – accelerometer; 3 – double Halbach arrays; 4 – MRE samples; 5 – upper plate; 6 – exitation signal from impact hammer; 7 – response signal

4. SUMMARY

The design concept of test stand presented in the article covers all aspects of the design process of the desired test stand. The basic idea of the test stand is to utilize the principle of modal analysis in the test stand for examining damping properties of magnetorheological elastomers. For this purpose single degree of freedom system was adapted to increase the effectiveness of the test stand and reduce interferences that might appear during the test. The great advantage of the one degree of freedom test stand is that it presents single result that can be easily interpreted and analyzed using the peak picking method and the circle fit method.

As the stand requires use of strong magnetic field all its elements were designed as nonmagnetic and nonconductive so the magnetic field would not distort the results. Also the external vibrations would strongly interfere with the results therefore design provides suspension for the test stand such that will eliminate all the effects related to the external vibrations.

The magnetic field presented in the article is a promising idea of mechanically controlled magnetic array that creates uniform magnetic field. The double round Halbach array presented in the article have been adapted for the demanding conditions of the test stand including small size of the device, ease of the control and creation of relatively high magnetic field and significant change in the created magnetic field. The array have been also modeled using FEMM software.

All those aspects were joined together and the model of the test stand have been prepared to present how it will be constructed and how it will operate. On base of this design concept the real test stand will be constructed according to the specification presented in the article. The results obtained using the test stand will help to designing working and applicable vibration dampers based on the MRE material.

REFERENCES

1. **Choi J. S., Yoo J.** (2008), Design of a Halbach Magnet Array Based on Optimization Techniques, *Magnetics*, 44, 10, 2361-2366.
2. **Giraudeau A., Pierron F.** (2005), Identification of stiffness and damping properties of thinisotropic vibrating plates using the virtual fields method: theory and simulations, *Journal of Sound and Vibration*, 284, 757–781.
3. **H. Raich and P. Blümler** (2004), Design and construction of a dipolar halbach array with a homogeneous field from identical bar magnets: Nmr mandhalas. *Concepts in Magnetic Resonance Part B: Magnetic Resonance Engineering*, 23B (1):16–25.
4. **I. Kasa** (1976), A circle fitting procedure and its error analysis, *IEEE Trans. Instrum. Meas.*, Vol. 25, 8–14.
5. **Kaleta J., Królewicz M., Lewandowski D.** (2011), Magnetomechanical properties of anisotropic and isotropic magnetorheological composites with thermoplastic elastomer matrices, *Smart Materials & Structures*, 20, 1–12.
6. **Liao G. J., Gong X. L., Kang C. J., Xuan S. H.** (2011), The design of an active-adaptive tuned vibration absorber based on magnetorheological elastomer and its vibration attenuation performance, *Smart Materials and Structures,* 20:75015-75024.
7. **Maia N. M. M.** (1999), Modal Identification Methods in the Frequency Domain, *Modal Analysis and Testing*, 363, 251-264.
8. **Olmos B. A., Roesset J. M.** (2010), Evaluation of the half-power bandwidth method to estimate damping in system without real modes, *Earthquake Engineering and Structural Dynamics*, 39, 1671–1686.
9. **Umbach D., Jones K.** (2003), A Few Methods for Fitting Circles to Data, *Instrumentation and Measurement*, 52, 1881-1885.
10. **Zhu Z. Q., Howe D.** (2001), Halbach permanent magnet machines and applications: a review, *IEE Proceedings - Electric Power Applications*, Vol. 148, No. 4, 299-308.

This research was partly supported by Wrocław Research Centre EIT + within the project 'The Application of Nanotechnology in Advanced Materials'–NanoMat (POIG.01.01.02-02-002/08) financed by the European Regional Development Fund (Innovative Economy OperationalProgramme, 1.1.2).

ASSESSMENT TRIBOLOGICAL PROPERTIES OF COATINGS APPLIED BY HVOF TECHNOLOGY

Janette BREZINOVÁ[*], Anna GUZANOVÁ[*], Dagmar DRAGANOVSKÁ[*], Marián EGRI[**]

[*]Faculty of Mechanical Engineering, Department of Technology and Materials, Technical University of Košice, Mäsiarska 74, 040 01 Košice, Slovakia
[**]SLOVNAFT Montáže a Opravy, a.s., Vlčie hrdlo, P.O.Box 52, 820 03 Bratislava, Slovakia

janette.brezinova@tuke.sk, anna.guzanova@tuke.sk, dagmar.draganovska@tuke.sk, marian.egri@slovnaft.sk

Abstract: In this article, the attention is paid to the HVOF (High Velocity Oxygen Fuel) thermal spraying method by which the progressive coatings are applied on basic material C15E (STN 412020). These coatings are based on C-17CO, WC-CO-Cr and Cr3C2-25NiCr. There was made determination of the chemical composition of the coatings and assessment of coatings quality - adhesion, microhardness, porosity and wear resistance at room temperature (21°C) and also at operational elevated temperature (900°C). Results of adhesive wear showed high quality of all evaluated coatings and their suitability to extreme tribological conditions.

Key words: HVOF Coatings, Adhesion, Hardness, Porosity, Wear Resistance

1. INTRODUCTION

The progressive coatings become an alternative for prospective application in various fields of industry because of their flexibility, high quality combined with durability in real and highly demanding conditions. Thermally-sprayed coatings belong to the dynamically developing field of surface engineering (Sahraoui et al., 2004; González-Hermosilla et al., 2010; Hadad et al., 2008; Fang, 2009; Bolelli, 2009). These high-quality functional coatings are applied in the basic industry, as well as in renovations (Tan et al., 1999), mainly due to their excellent properties, which are characterized by high wear resistance, corrosion resistance and resistance against high temperatures (Sahraoui et al., 2004; Ramesh et al., 2010; Boleli et al., 2007; Thakur et al., 2011l Lee et al., 2010; Maiti et al., 2007; Venkateswarlu et al., 2009). Thanks to wide range of different combinations coating–substrate material, thermal spraying offers as many possibilities as no other technology of coatings deposition. HVOF (High Velocity Oxygen Fuel) is one of the technology, which formed coatings with very small porosity (<1 %) compared with the basic material and high adhesion strength (> 80 MPa). There are minimal thermal changes of substrate during spraying and also roughness of coating surface is low. It is possible to deposit wide spectrum materials, from pure metals up to special alloys. Resistance of coating based on cermets is determined predominantly by type, morphology and size of hard particles and their volume fraction in a tough matrix.

The paper presents experimentally obtained results aimed at assessing selected coatings applied by HVOF technology: C-17CO, WC-CO-Cr and Cr_3C_2-25NiCr. The coatings were subjected to couple of tests. Their tribological properties were evaluated by pin-on-disc test. The quality of coatings was evaluated by pull-off test, measuring the microhardness, and by EDX analysis. Conditions of experimental works were chosen in order to simulate operating conditions, namely wear in elevated temperature (900°C).

2. EXPERIMENTAL PROCEDURE

Substrate for application the coatings was made of structural carbon steel C15E. Chemical composition of the steel is listed in Tab. 1.

Tab. 1. Chemical composition of the steel substrate (wt. %)

C	Mn	Si	P	S
0.12–0.18	0.30–0.60	0.15–0.40	max 0.035	max 0.035

Mechanical properties of the steel substrate: tensile strength 740 – 880 MPa, yield strength ≥440 MPa. The substrates for test samples were made from round bar Ø50 mm with a height of 15 mm.

Substrate pre-treatment

Test samples were pre-treated by air grit blasting: air pressure of 0.5 MPa, abrasive - brown corundum, grain size 1.00 mm.

Material of coatings

There were deposited three types of coatings by HVOF technology on pretreated samples. On the first group of samples, coating of 1343 (C-17Co) was applied, on the second group of= samples coating of 1350 (WC-Co-Cr) was deposited and on the third group of samples coating 1375 (Cr_3C_2-25NiCr) was deposited. Materials of coatings were supplied as a powder, agglomerated and sintered, produced by Praxair, Inc., USA. Tab. 2 shows chemical composition of the powders.

Tab. 2. Chemical composition of the powders sprayed

Coating	C	Co	Fe	W	Cr	Ni
1343	5.5	16.2	0.036	78.4		
1350	5.5	9.9	0.02	80.6	3.9	
1375	10				68.5	21

For the coating deposition equipment JP-5000, Praxair TA was used; it deposits coatings using system HP/HVOF (High

Pressure/High Velocity Oxygen Fuel) with System Powder Feeder 1264. The surface of deposited coatings was not further modified after spraying. Parameters of spraying are listed in Tab. 3.

Tab. 3. Parameters of spraying and properties of coatings

Particle velocity [m/s]	600 ÷ 1000
Adhesion [MPa]	< 70
Oxide content [%]	1 - 2
Porosity [%]	1 - 2
Deposition power [kg/h]	3 - 6
Typical coating thickness [mm]	0.2 - 2

Testing of coatings properties

Thickness of the coating was determined by magnetic thickness gauge. Construction, structure and chemical analysis of examined coatings was studied using scanning electron microscopy (SEM) JEOL JSM – 7 000 F. Chemical analysis was conducted using the EDX analyzer INCA, which allows local EDX chemical analysis of the material.To determine the basic properties of coatings, microhardness was measured according to STN ISO 4516 on Shimadzu HMV-2E test equipment, load 980,7 mN (10 g), dwell time 15 s. Porosity of coatings was determined by mercury porosimetry using PoreMaster porosimeter. Adhesion of coatings was evaluated by pull-off test according to STN EN 582. After pull-off adhesion test, tensile stress necessary to rupture the weakest inter-phase (adhesive fracture) or the weaker component (cohesive fracture) were determined.

To simulate the working conditions, coatings were subjected to adhesive wear using pin-on-disc test (ISO 20808) at 21°C and 900°C. Testing conditions: relative humidity 21%, atmosphere: air, test ball diameter ø6 mm, radius of ball track was 5.01 mm, linear velocity 10.00 cm.s-1, normal load 5N, stop condition 300 m.

3. RESULTS AND DISCUSSION

In Tab. 4 are presented values of thickness, microhardness and open porosity of evaluated coatings.

Tab. 4. Thickness, microhardness and total porosity of evaluated coatings

Coating	1343	1350	1375
Thickness [μm]	234	356	393
Microhardness HV0,1	1010	1447	975
Open porosity [%]	0.16	0.88	0.17
Adhesion [MPa]	18.5	31.6	31.6

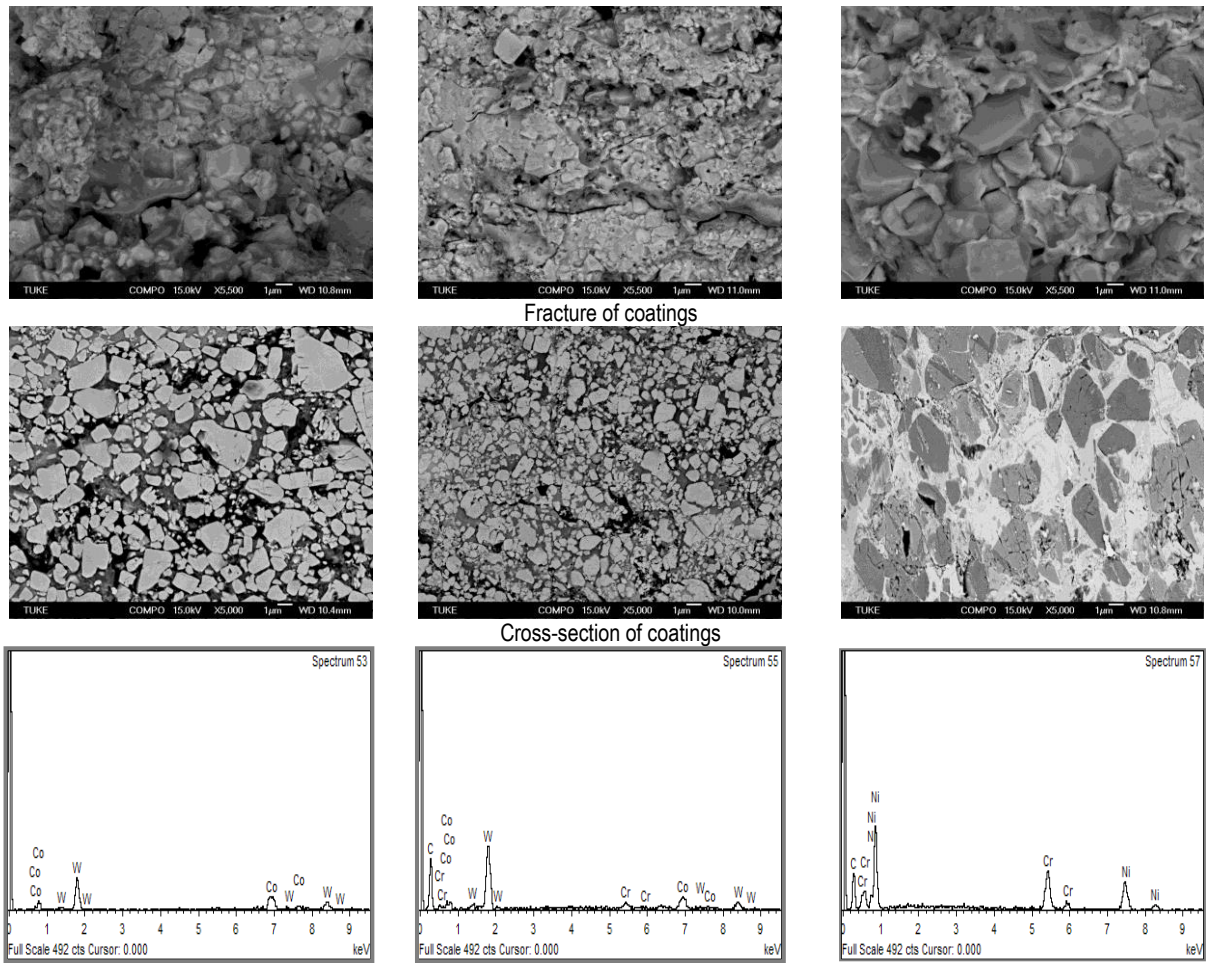

Fig. 1. Fractures, cross-sections and EDX analysis of coatings

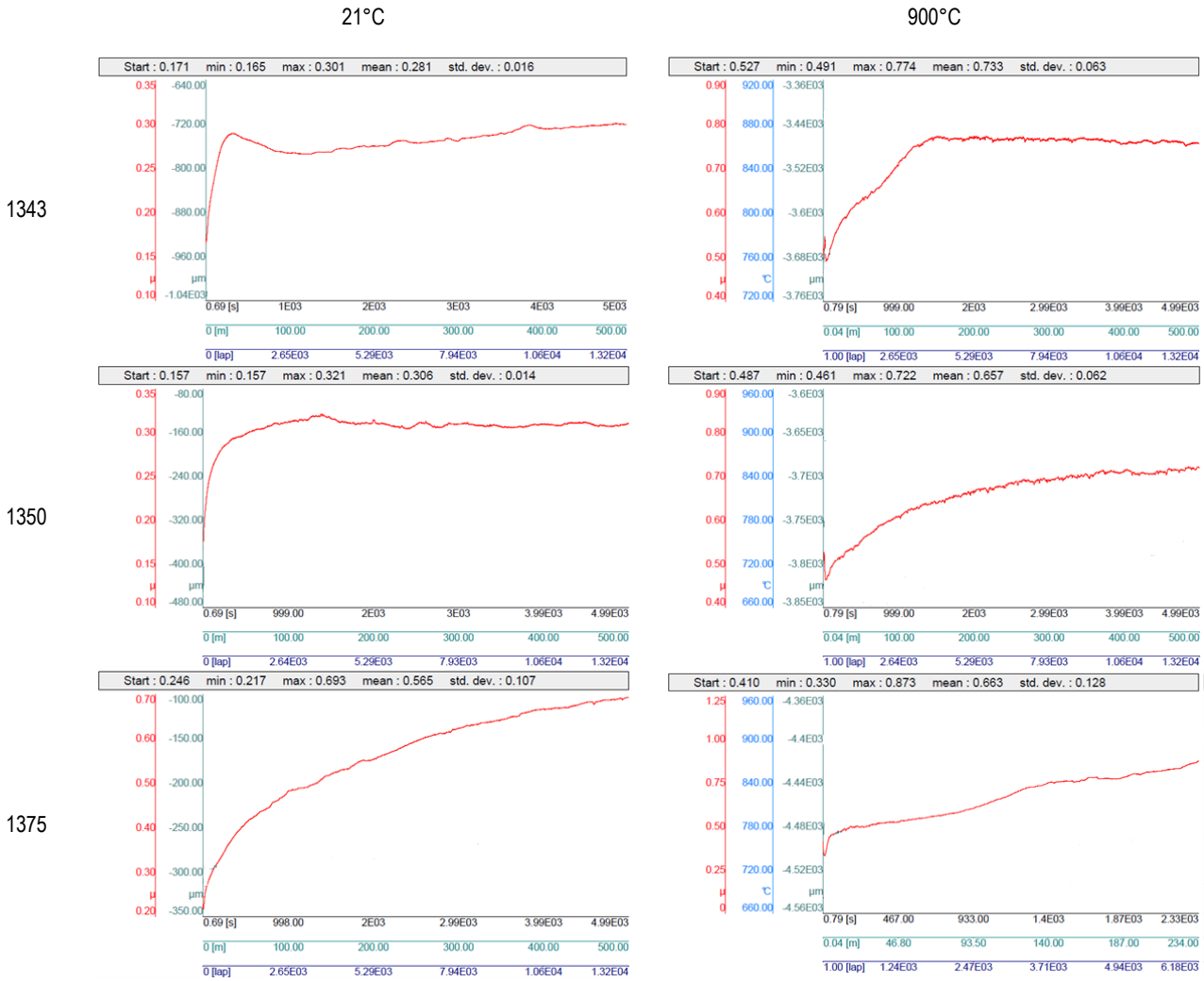

Fig. 2. Friction cefficient of coatings

Authors (Lee et al., 2009) stated porosity of coating 1350 (WC-Co-Cr) in the range of 0.6 to 2.7 % depending on whether the powder is monodisperse or poly-disperse and on various portions of powder grain size in mixtures. Porosity was assessed by image analysis on cross-sections that included open and closed porosity together. Results of our research indicate that if we evaluate the porosity of the coating as a 3D body (in our case using mercury porosimetry), porosity of the coating is less (0.88 %), because the measure reflects only open pores.

Porosity of the coating 1375 (Cr_3C_2 – 25NiCr) according the authors (Sidhu et al., 2006) is between 2.5-3.5 % for the same reasons. Our research has confirmed the open porosity of the coating (1375) 0.17 %. The authors (Bolelli et al., 2009) who investigated the effect of the number of torch scans to the coating porosity have reached similar conclusions. It revealed that increasing thickness (number of torch scans) of coating lead to porosity decrease. However, they again found higher porosity on metallographic sections by image analysis than we by mercury porosimetry. Divergence of obtained porosity values results from different principle from the methods used.

The highest microhardness values was shown by coating 1350 (1447 HV 0,1) which was caused by a high content of tungsten and addition of cobalt compared to the coating 1343, which also contains tungsten but at lower concentrations and had lower values of microhardness (1010 HV 0,1). The lowest microhardness values were shown by coating 1375 with a high content of chromium, tungsten-free (975 HV 0,1). The assessment of porosity showed that coating 1350 is more porous compared to the other two coatings which have almost the same porosity considering the structure of a coating and its chemical composition.

Coating 1343 reached a lower coating adhesion compared to coatings 1350 and 1375. Fractures, cross-sections and results of EDX analysis are shown in Fig. 1.

EDX spectral analysis of the coating 1343 showed the presence of two basic phases – solid particles WC and cobalt surrounding WC particles, which corresponds to the chemical composition of powders for coatings production. EDX spectral analysis of the coating 1350 shows the presence of WC particles and chrome and cobalt matrix surrounding WC particles. EDX spectral analysis of the coating 1375 again confirmed the presence of large particles of Cr_3C_2 and the most extensive component of coating 1375 - nickel-chromium matrix. Matrix and hard particles of WC and Cr_3C_2 are well visible on cross-sections and also on fractures of the coatings.

The pin-on-disc test was realized at temperatures of the samples 20°C and 900°C. Referred experiment temperature of 900°C was chosen because of simulation in real conditions in practice. It was evaluated and compared coefficient of friction [-], Fig. 2, the wear volume of disc specimen V_{disc} [mm^3] and specific wear rate of disc specimen W [$mm^3.N^{-1}.m^{-1}$] at selected pressures and temperatures specified.

The coefficient of friction at 21°C was for the coating 1343

and 1350 almost the same (~ 0.3±0.016), for the coating 1375 was more than twice and throughout the test continuously increased (>0.7±0.107). At the test temperature 900°C, all coatings achieved a considerably higher coefficient of friction than at room temperature. Fig. 3 shows wear traces of coatings.

After pin-on-disc test of all coatings at 21°C and 900°C were evaluated volume of material removal (V_{disc}) and the specific wear rate (W_{disc}) from the depth profile of wear trace, Fig. 4.

Results of coatings wear test at 900°C showed that the wear rate of coatings 1343 and 1375 is extremely small, just a roughness change in wear track occured. The coating 1350 showed higher removal of material, $V_{disc,900°C}$ = 0.056 mm^3, $W_{disc,900°C}$ = 3.7.10^{-5} mm^3.N^{-1}.m^{-1}. For other coatings was not observed measurable weight loss of coating material. During the tribological tests the transfer of ball material to the surface of the tested coatings occured.

The authors (Bolelli et al., 2009) indicate wear reate of coating WC-Co-Cr (1350) at room temperature cca n.10^{-8}mm^3.N^{-1}m^{-1}. Given the available weighing machine with a resolution of 10^{-5} kg weight we brand mass loss of evaluated coatings as unmeasurable (using our device), so we assumed mass loss below 10^{-5} kg, which is consistent with the results of authors mentioned above. However, we also evaluated the wear rate at 900°C, which were found higher wear rate of coating 1350: 3.7.10^{-5} mm^3.N^{-1}.m^{-1}.

Results of adhesion test pointed on high quality of evaluated coatings and their suitability for extreme tribological conditions.

4. CONCLUSIONS

The paper discusses evaluation of selected properties of three types of cermet coatings applied by HVOF technology designed for high tribocorrosive conditions. The highest hardness showed coating WC-Co-Cr, which showed simultaneously the highest porosity.

This porosity was probably the cause of higher specific wear rate compared with other assessed coatings. Coatings C-17Co and Cr3C2-25NiCr despite of lower hardness achieved a higher resistance to the adhesive wear due to their chemical composition and structure of the coatings. In terms of frictional properties, the highest friction coefficient at 21°C showed coating Cr3C2-25NiCr, at 900°C a significant increasing in the friction coefficient for all coatings occured.

The results of experimental measurements showed that all investigated coatings, which showed a high quality and wear resistance, can be suggested to tribodegradation conditions at high temperatures.

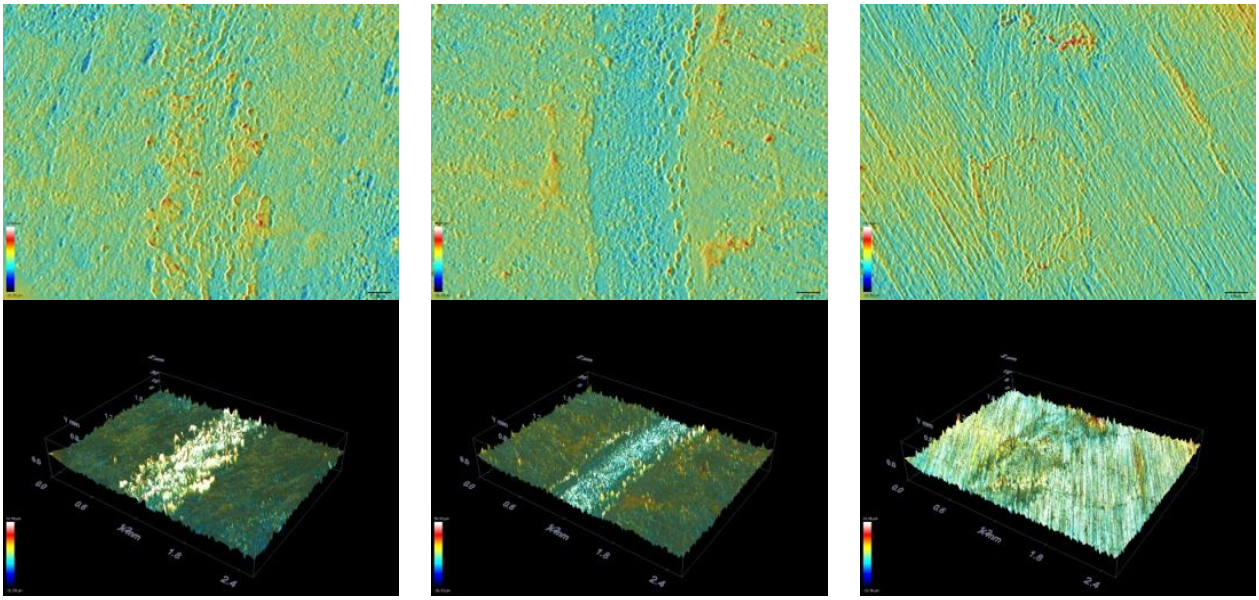

Fig. 3 Wear traces of coatings

Fig. 4 Depth profile of coating 1350 wear trace

REFERENCES

1. **Bolelli G**. (2009), HVOF-sprayedWC–CoCr coatings on Al alloy: Effect of the coating thickness on the tribological properties, *Wear,* Vol. 267, 944-953.
2. **Bolelli G. et al**. (2007), Microstructural and tribological comparison of HVOF-sprayed and post-treated M–Mo–Cr–Si (M=Co, Ni) alloy coatings, *Wear*, Vol. 263, 1397-1416.
3. **Bolelli G., Lusvarghi L., Barletta M.** (2009), HVOF-sprayedWC–CoCr coatings on Al alloy: Effect of the coating thickness on the tribological properties, *Wear,* Vol. 267, 944–953.
4. **Fang W.** (2009)**,** Processing optimization, surface properties and wear behavior of HVOF spraying WC–CrC–Ni coating, *Journal of Materials Processing Technology,* Vol. 209, 3561-3567.
5. **González-Hermosilla W. A. et al.** (2010), Effect of substrate roughness on the fatigue behavior of a SAE 1045 steel coated with a WC–10Co–4Cr cermet, deposited by HVOF thermal spray, *Materials Science and Engineering A*, Vol. 527, 6551-6561.
6. **Hadad M. et al.** (2008), Adhesion evaluation of multilayered based WC–Co–Cr thermally sprayed coatings, *Surface and Coatings Technology,* Vol. 202, 4399-4405.
7. **Lee C.W., Han J.H., Yoon J., Shin M.C., Kwun S.I**. (2010), A study on powder mixing for high fracture toughness and wear resistance of WC–Co–Cr coatings sprayed by HVOF, *Surface and Coatings Technology*, Vol. 204, 2223-2229.
8. **Lee C.W., Han J.H., Yoon J., Shin M.C., Kwun S.I.** (2010), A study on powder mixing for high fracture toughness and wear resistance of WC–Co–Cr coatings sprayed by HVOF, *Surface and Coatings Technology*, Vol. 204, 2223–2229.
9. **Maiti A.K., Mukhopadhyay N., Raman R.** (2007), Effect of adding WC powder to the feedstock of WC–Co–Cr based HVOF coating and its impact on erosion and abrasion resistance, *Surface and Coatings Technology,* Vol. 201, 7781-7788.
10. **Ramesh M.R. et al**. (2010), Solid particle erosion of HVOF sprayed WC-Co/NiCrFeSiB coatings, *Wear*, Vol. 269 197-205.
11. **Sahraoui T., Guessasma S., Fenineche N. E., Montavon G., Coddet C.** (2004), Friction and wear behaviour prediction of HVOF coatings and electroplated hard chromium using neural computation, *Materials Letters,* Vol. 58, 654-660.
12. **Sidhu H. S., Sidhu B. S., Prakash S.** (2006), Mechanical and microstructural properties of HVOF sprayed WC–Co and Cr_3C_2–NiCr coatings on the boiler tube steels using LPG as the fuel gas, *Journal of Materials Processing Technology*, Vol. 171, 77–82.
13. **Tan J.C., Looney L., Hashmi M.S.J.** (1999), Component repair using HVOF thermal spraying, *Journal of Materials Processing Technology,* Vol. 92-93, 203-208.
14. **Thakur L., Arora N., Jayaganthan R., Sood R.** (2011), An investigation on erosion behavior of HVOF sprayed WC–CoCr coatings, *Applied Surface Science*, Vol. 258 1225-1234.
15. **Venkateswarlu K. et al.** (2009), Abrasive wear behavior of thermally sprayed diamond reinforced composite coating deposited with both oxy-acetylene and HVOF techniques, *Wear,* Vol. 266, 996-1002.

This contribution was supported by Grant Agency VEGA No. 1/0600/13. The authors are grateful to APVV for support of experimental work under grant APVV-0682-11 - Application of progressive tool coatings for increasing the effectiveness and productivity of forming sheets made of modern materials.

AN ANTICRACK IN A TRANSVERSELY ISOTROPIC SPACE

Andrzej KACZYŃSKI

Faculty of Mathematics and Information Science, Warsaw University of Technology, ul. Koszykowa 75, 00-662 Warszawa, Poland

akacz@mini.pw.edu.pl

Abstract: An absolutely rigid inclusion (anticrack) embedded in an unbound transversely isotropic elastic solid with the axis of elastic symmetry normal to the inclusion plane is considered. A general method of solving the anticrack problem is presented. Effective results have been achieved by constructing the appropriate harmonic potentials. With the use of the Fourier transform technique, the governing system of two-dimensional equations of Newtonian potential type for the stress jump functions on the opposite surfaces of the inclusion is obtained. For illustration, a complete solution to the problem of a penny-shaped anticrack under perpendicular tension at infinity is given and discussed from the point of view of material failure.

Key words: Three-Dimensional Elasticity, Transversely Isotropic Material, Plane Anticrack, Singular Integral Equations, Stress Singularity

1. INTRODUCTION

The study of the redistribution of stresses due to the presence of different kinds of defects in elastic bodies merit attention of specialists from many branches, such as geomechanics, metallurgy, material science. From the viewpoint of inhomogeneities in solids, cracks characterized by the displacement discontinuity and flat rigid inclusions (called anticracks) with the traction discontinuity are the two dangerous extremes. Although the crack problems have been studied extensively over the past 50 years, research on the corresponding anticrack problems have been rather limited and mainly concentrated on two-dimensional problems related to rigid line inclusions (see the monographs by Berezhnitskii et al. (1983) and Ting (1996)). The corresponding three-dimensional analysis of a penny-shaped anticrack (absolutely rigid circular lamella) has been performed to a much lesser extent. Detailed account of elastostatic problems involving planar rigid inclusions embedded in homogeneous media is given in the studies by Kassir and Sih (1968), Selvadurai (1982), Silovanyuk (1984, 2000), Podil'chuk (1997), Rahman (1999, 2002), Chaudhuri (2003, 2012), Shodja and Ojaghnezhad (2007), and in the monographs by Mura (1981), Panasyuk et al. (1986), Khai (1993), Rogowski (2006), Kanaun and Levin (2008).

This paper is devoted to a three-dimensional static problem in linear elasticity theory of an infinite transversely isotropic body containing an arbitrarily shaped rigid inclusion lying in a plane of isotropy and subjected to some external loads. In Section 2 the basic equations with the potential representations of their general solution are reported. Besides, the anticrack problem is formulated. Section 3 presents a general method of solving the resulting boundary value problems. The governing 2-D singular integral equations are obtained in terms of the stress discontinuities across inclusion faces. As an illustration, a closed-form solution is given and discussed in Section 4 for a circular rigid inclusion subjected to tension at infinity. Finally, Section 5 concludes the paper.

2. STATEMENT OF THE PROBLEM

2.1. Basic equations and general potential solutions

The results of comprehensive research on the theory and applications of the mechanics of transversely isotropic elastic materials can be found in the book by Ding et al. (2006).

Referring to the rectangular Cartesian coordinate system (x_1, x_2, x_3) denote at the point $\mathbf{x} = (x_1, x_2, x_3)$ the displacement vector by $\mathbf{u} = (u_1, u_2, u_3)$ and the stresses by $\sigma_{11}, \sigma_{12}, \sigma_{22}, \sigma_{13}, \sigma_{23}, \sigma_{33}$.

Throughout the considerations the following notations will be used: Latin subscripts always assume values 1, 2, 3 and the Greek ones 1, 2. The Einstein summation convention holds and subscripts preceded by a comma indicate partial differentiation with respect to the corresponding coordinates.

Consider a homogeneous transversely isotropic space assuming that the axis of elastic symmetry of the material coincides with the x_3-axis. Then the number of independent elastic stiffness constants (moduli) in the generalized Hooke's low reduces to five: $c_{11}, c_{12}, c_{13}, c_{33}, c_{44}$. The stress-displacement equations are the following:

$$\sigma_{\alpha 3} = c_{44}\left(u_{\alpha,3} + u_{3,\alpha}\right), \ \alpha = 1, 2 \tag{1}$$

$$\sigma_{33} = c_{13}\, u_{\gamma,\gamma} + c_{33}\, u_{3,3} \tag{2}$$

$$\sigma_{11} = c_{11}\, u_{1,1} + c_{12}\, u_{2,2} + c_{13}\, u_{3,3} \tag{3}$$

$$\sigma_{22} = c_{12}\, u_{1,1} + c_{11}\, u_{2,2} + c_{13}\, u_{3,3} \tag{4}$$

$$\sigma_{12} = 0{,}5\left(c_{11} - c_{12}\right)\left(u_{1,2} + u_{2,1}\right) \tag{5}$$

Inserting the above expressions into equilibrium equations in the absence of body forces

$$\sigma_{jk,k} = 0 \tag{6}$$

a governing system of three linear partial differential equations of second order with constant coefficients for displacements is obtained:

$$0{,}5(c_{11}+c_{12})u_{\gamma,\gamma\alpha}+0{,}5\,(c_{11}-c_{12})\,u_{\alpha,\gamma\gamma}+c_{44}\,u_{\alpha,33}+ \\ +(c_{13}+c_{44})\,u_{3,3\alpha}=0\,,\ \alpha=1,2 \tag{7}$$

$$(c_{13}+c_{44})\,u_{\gamma,\gamma 3}+c_{44}\,u_{3,\gamma\gamma}+c_{33}\,u_{3,33}=0 \tag{8}$$

According to the results obtained by Kaczyński (1993) with some modifications, the general solution of the above equations is found in terms of three potential functions $\varphi_j \equiv \varphi_j(x_1, x_2, z_j)$, $j = 1,2,3$ with $z_j = t_j x_3$ which are harmonic in the appropriate coordinate systems(x_1, x_2, z_j), i.e.

$$\varphi_{j,\gamma\gamma}+\frac{\partial^2\varphi_j}{\partial z_j^2}=0,\ j=1,2,3;\ \text{no sum on } j \tag{9}$$

The form of displacement representation is dependent on the three material characterizing parameters t_j. The constant t_3 is given as:

$$t_3=\sqrt{(c_{11}-c_{12})/2c_{44}}>0 \tag{10}$$

while the constants $t_\alpha(\alpha = 1,2)$ are the roots with positive real part of the following eigen-equation:

$$c_{33}c_{44}t^4+\left[(c_{13})^2+2c_{13}c_{44}-c_{11}c_{33}\right]t^2+c_{11}c_{44}=0 \tag{11}$$

The analysis of modulus restrictions based on the positive definiteness of the stress energy leads to two cases (Ding et al.; 2006):

Case 1: $t_1 \neq t_2$ when $A_- \neq 2c_{44}$

$$A_->2c_{44}\Rightarrow\begin{cases}t_1=0{,}5(t_+-t_-)>0\\ t_2=0{,}5(t_++t_-)>0\end{cases} \tag{12}$$

or

$$A_-<2c_{44}\Rightarrow\begin{cases}t_1=0{,}5(t_+-it^*)\\ t_2=0{,}5(t_++it^*)\end{cases},\ i^2=-1 \tag{13}$$

where:

$$A_\pm=\sqrt{c_{11}c_{33}}\pm c_{13}\\ t_\pm=\sqrt{(A_\pm\pm 2c_{44})A_\mp/c_{33}c_{44}}\\ t^*=\sqrt{(2c_{44}-A_-)A_+/c_{33}c_{44}} \tag{14}$$

Case 2: $t_1=t_2$

$$A_-=2c_{44}\Rightarrow t_1=t_2=\sqrt[4]{c_{11}/c_{33}}\equiv t_0 \tag{15}$$

In the case when the material is isotropic it is found that:

$$t_0=t_3=1\\ c_{11}=c_{33}=\lambda+2\mu=\frac{2\mu(1-\nu)}{1-2\nu}\\ c_{12}=c_{13}=\lambda=\frac{2\mu\nu}{1-2\nu},\quad c_{44}=\mu \tag{16}$$

Here, λ, μ are Lamé constants, and ν is Poisson's ratio.

For the sake of simplicity, hereinafter we proceed to consider the case with distinct eigenvalues (Case 1). Then the displacements and stresses can be represented in terms of potentials as follows:

$$u_\alpha=(\varphi_1+\varphi_2)_{,\alpha}+\in_\alpha^\gamma\varphi_{3,\gamma}\,,\ \alpha=1,2 \tag{17}$$

$$u_3=m_\gamma t_\gamma\frac{\partial\varphi_\gamma}{\partial z_\gamma} \tag{18}$$

$$\frac{\sigma_{3\alpha}}{c_{44}}=(1+m_\gamma)t_\gamma\frac{\partial^2\varphi_\gamma}{\partial z_\gamma\partial x_\alpha}+\in_\alpha^\gamma t_3\frac{\partial^2\varphi_3}{\partial z_3\partial x_\gamma} \tag{19}$$

$$\frac{\sigma_{33}}{c_{44}}=(1+m_\gamma)\frac{\partial^2\varphi_\gamma}{\partial z_\gamma^2} \tag{20}$$

$$\sigma_{11}=-c_{44}(1+m_\gamma)t_\gamma^2\frac{\partial^2\varphi_\gamma}{\partial z_\gamma^2}+ \\ -(c_{11}-c_{12})\left[(\varphi_1+\varphi_2)_{,22}+\varphi_{3,12}\right] \tag{21}$$

$$\sigma_{22}=-c_{44}(1+m_\gamma)t_\gamma^2\frac{\partial^2\varphi_\gamma}{\partial z_\gamma^2}+ \\ -(c_{11}-c_{12})\left[(\varphi_1+\varphi_2)_{,11}-\varphi_{3,12}\right] \tag{22}$$

$$\sigma_{12}=(c_{11}-c_{12})\left[(\varphi_1+\varphi_2)_{,12}+0{,}5(\varphi_{3,11}-\varphi_{3,22})\right] \tag{23}$$

Here $\in_2^1=1, \in_1^2=-1$, $\in_1^1=\in_2^2=0$ and the constants m_1, m_2 related to t_1, t_2 are defined as:

$$m_\alpha=\frac{c_{11}-t_\alpha^2c_{44}}{(c_{13}+c_{44})t_\alpha^2}=\frac{c_{13}+c_{44}}{t_\alpha^2c_{33}-c_{44}}\,,\ \alpha=1,2 \tag{24}$$

It is worth noting that:

$$\begin{cases}c_{33}m_\alpha t_\alpha^2-c_{13}=c_{44}(1+m_\alpha)\\ c_{11}-c_{13}m_\alpha t_\alpha^2=c_{44}t_\alpha^2(1+m_\alpha)\end{cases},\ \alpha=1\text{ or }2,\text{ no sum on }\alpha\\ m_1m_2=1\\ t_1t_2=\sqrt{c_{11}/c_{33}}\\ (t_1)^2+(t_2)^2=\left(c_{11}c_{33}-c_{13}^2-2c_{13}c_{44}\right)/c_{33}c_{44} \tag{25}$$

2.2. Formulation

Consider a transversely isotropic space with the axis of symmetry as the x_3- axis and the isotropic plane as the x_1, x_2 - plane. Suppose that this body is weakened by a rigid-sheet like inclusion (anticrack) occupying a certain domain S with a smooth boundary at the plane $x_3 = 0$ and subjected to some external loads.

It is known that an anticrack problem can be regarded as the superposition of two problems. One (labelled by the subscript 0) is no inclusion problem with the given applied loadings and the other is the perturbed problem in which the displacements along the anticrack S are prescribed as the negative of those generated in the first problem. Thus, the total displacement-stress field (denoted by $u_j^{(t)}$and $\sigma_{jk}^{(t)}$) can be expressed as:

$$u_j^{(t)} = u_j^{(0)} + u_j\,, \quad \sigma_{jk}^{(t)} = \sigma_{jk}^{(0)} + \sigma_{jk} \tag{26}$$

Moreover, we assume that $u_j^{(0)}$and $\sigma_{jk}^{(0)}$)are known from the solution to the 0-problem. As a matter of fact, only the values of displacements $\bar{u}_j^{(0)} \equiv u_j^{(0)}(x_1, x_2, 0), (x_1, x_2) \in S$ are needed in the subsequent analysis.

Next, we concentrate attention on the non-trivial perturbed problem, solution to which tends to zero at infinity and satisfies the necessary boundary conditions on S:

$$u_1 = -\bar{u}_1^{(0)} + \varepsilon_1 - \omega_3 x_2 \tag{27}$$

$$u_2 = -\bar{u}_2^{(0)} + \varepsilon_2 + \omega_3 x_1 \tag{28}$$

$$u_3 = -\bar{u}_3^{(0)} + \varepsilon_3 - \omega_2 x_1 + \omega_1 x_2 \tag{29}$$

in which also the unknown small displacements ε_j and rotations ω_j are included to describe a motion of the inclusion as a rigid unit. These parameters will be determined later in solving the problem in hand from the equilibrium conditions of the anticrack (no resultant forces and zero-moments).

Now we proceed to the reduction of the above anticrack problem to some mixed boundary-value problems of potential theory related to the one of a half-space (say, $x_3 \geq 0$). From the relevant symmetry properties about the plane $x_3 = 0$ follows the division of the problem into antisymmetric (A) and symmetric ones (B).

In the antisymmetric part (A) of the problem, the mixed conditions on the plane of antisymmetry may be written as

$$u_3 = -\bar{u}_3^{(0)} + \varepsilon_3 - \omega_2 x_1 + \omega_1 x_2\,, \ (x_1, x_2) \in S \tag{30}$$

$$u_1 = u_2 = 0\,, \ (x_1, x_2) \in R^2 \tag{31}$$

$$\sigma_{33} = 0, \ (x_1, x_2) \in R^2 - S \tag{32}$$

and are supplemented by the corresponding equilibrium conditions to determine the unknown parameters $\varepsilon_3, \omega_\alpha (\alpha = 1,2)$:

$$\iint_S \left[\sigma_{33}\left(x_1, x_2, 0^+\right) - \sigma_{33}\left(x_1, x_2, 0^-\right)\right] dx_1 dx_2 = 0 \tag{33}$$

$$\iint_S x_{3-\alpha} \left[\sigma_{33}\left(x_1, x_2, 0^+\right) - \sigma_{33}\left(x_1, x_2, 0^-\right)\right] dx_1 dx_2 = 0 \tag{34}$$

The symmetric part (B) of the problem leads to the following mixed conditions

$$u_1 = -\bar{u}_1^{(0)} + \varepsilon_1 - \omega_3 x_2\,, (x_1, x_2) \in S \tag{35}$$

$$u_2 = -\bar{u}_2^{(0)} + \varepsilon_2 + \omega_3 x_1, \ (x_1, x_2) \in S \tag{36}$$

$$u_3 = 0, \ (x_1, x_2) \in R^2 \tag{37}$$

$$\sigma_{31} = \sigma_{32} = 0, \ (x_1, x_2) \in R^2 - S \tag{38}$$

and additional conditions to determine the unknown parameters $\varepsilon_\alpha (\alpha = 1,2), \ \omega_3$:

$$\iint_S \left[\sigma_{3\alpha}\left(x_1, x_2, 0^+\right) - \sigma_{3\alpha}\left(x_1, x_2, 0^-\right)\right] dx_1 dx_2 = 0 \tag{39}$$

$$\begin{aligned} &\iint_S x_2 \left[\sigma_{31}\left(x_1, x_2, 0^+\right) - \sigma_{31}\left(x_1, x_2, 0^-\right)\right] dx_1 dx_2 + \\ &-\iint_S x_1 \left[\sigma_{32}\left(x_1, x_2, 0^+\right) - \sigma_{32}\left(x_1, x_2, 0^-\right)\right] dx_1 dx_2 = 0 \end{aligned} \tag{40}$$

In addition to these boundary conditions, the displacement and stress fields must vanish at infinity.

3. SOLUTION METHOD

The above-mentioned problems (A) and (B) are now reducing to some mixed boundary-value problems of potential theory by constructing the potentials functions well suited to the boundary conditions (30)-(32) and (35)-(38), respectively. Further, an integral equation formulation is given for these problems.

3.1. Antisymmetric problem

It is expedient to choose in the displacement-stress representations (17)-(23) only one harmonic function $f(x_1, x_2, x_3)$ such that:

$$\begin{aligned} &\varphi_1(x_1, x_2, z_1) \equiv -f(x_1, x_2, z_1) \\ &\varphi_2(x_1, x_2, z_2) \equiv f(x_1, x_2, z_2) \\ &\varphi_3(x_1, x_2, z_3) \equiv 0 \end{aligned} \tag{41}$$

Then the corresponding displacement and stress components become:

$$u_\alpha = (-1)^\beta \left[f(x_1, x_2, z_\alpha)\right]_{,\beta}\,, \ \alpha = 1,2 \tag{42}$$

$$u_3 = (-1)^\beta \, m_\beta t_\beta \, \frac{\partial f\left(x_1, x_2, z_\beta\right)}{\partial z_\beta} \tag{43}$$

$$\frac{\sigma_{3\alpha}}{c_{44}} = (-1)^\beta \left(1 + m_\beta\right) t_\beta \frac{\partial^2 f\left(x_1, x_2, z_\beta\right)}{\partial z_\beta \partial x_\alpha}, \ \alpha = 1,2 \tag{44}$$

$$\frac{\sigma_{33}}{c_{44}} = (-1)^\beta \left(1 + m_\beta\right) \frac{\partial^2 f\left(x_1, x_2, z_\beta\right)}{\partial z_\beta^2} \tag{45}$$

$$\begin{aligned} \sigma_{11} = &-c_{44}(-1)^\beta \left(1 + m_\beta\right) t_\beta^2 \frac{\partial^2 f}{\partial z_\beta^2} + \\ &-(c_{11} - c_{12})(-1)^\beta \left[f\left(x_1, x_2, z_\beta\right)\right]_{,22} \end{aligned} \tag{46}$$

$$\begin{aligned} \sigma_{22} = &-c_{44}(-1)^\beta \left(1 + m_\beta\right) t_\beta^2 \frac{\partial^2 f}{\partial z_\beta^2} + \\ &-(c_{11} - c_{12})(-1)^\beta \left[f\left(x_1, x_2, z_\beta\right)\right]_{,11} \end{aligned} \tag{47}$$

$$\sigma_{12} = (c_{11} - c_{12})(-1)^\beta \left[f\left(x_1, x_2, z_\beta\right)\right]_{,12} \tag{48}$$

In the limit as $x_3 \to 0^\mp$, the above equations reduce to:

$$u_1 = u_2 = 0 \tag{49}$$

$$u_3 = \left(m_2 t_2 - m_1 t_1\right)\left[f_{,3}\left(x_1, x_2, x_3\right)\right]_{x_3=0} \tag{50}$$

$$\frac{\sigma_{3\alpha}}{c_{44}} = \left(m_2 t_2 - m_1 t_1 + t_2 - t_1\right)\left[f_{,3\alpha}\left(x_1, x_2, x_3\right)\right]_{x_3=0} \tag{51}$$

$$\frac{\sigma_{33}^{\pm}}{c_{44}} = \left(m_2 - m_1\right)\left[f_{,33}\left(x_1, x_2, x_3\right)\right]_{x_3=0^{\pm}} \tag{52}$$

$$\sigma_{11}^{\pm} = \sigma_{22}^{\pm} = -c_{44}\left[m_2 (t_2)^2 - m_1 (t_1)^2 + (t_2)^2 - (t_1)^2\right] \cdot \left[f_{,33}\left(x_1, x_2, x_3\right)\right]_{x_3=0^{\pm}} \tag{53}$$

$$\sigma_{12} = 0 \tag{54}$$

A glance at equations (37)-(39) reveals that the potential $f(x_1, x_2, x_3)$ is governed by:

– for $(x_1, x_2) \in S$

$$\left[f_{,3}\left(x_1, x_2, x_3\right)\right]_{x_3=0^{+}} = \frac{-\bar{u}_3^{(0)} + \varepsilon_3 - \omega_2 x_1 + \omega_1 x_2}{m_2 t_2 - m_1 t_1} \tag{55}$$

– for $(x_1, x_2) \in R^2 - S$

$$\left[f_{,33}\left(x_1, x_2, x_3\right)\right]_{x_3=0^{+}} = 0 \tag{56}$$

3.2. Symmetric problem

This problem is substantially more complex (see the corresponding skew-symmetrical crack problem considered in Kassir and Sih (1975)). We choose the potential functions in the general representation (16)-(22) such that:

$$\begin{aligned} \varphi_1 &= -\frac{m_2 t_2}{m_2 t_2 - m_1 t_1}\left(G_{1,1} + H_{1,2}\right) \equiv -\frac{m_2 t_2}{m_2 t_2 - m_1 t_1} F_1 \\ \varphi_2 &= \frac{m_1 t_1}{m_2 t_2 - m_1 t_1}\left(G_{2,1} + H_{2,2}\right) \equiv \frac{m_1 t_1}{m_2 t_2 - m_1 t_1} F_2 \\ \varphi_3 &= G_{3,2} - H_{3,1} \equiv F_3 \end{aligned} \tag{57}$$

where $G_j \equiv G(x_1, x_2, z_j)$ and $H_j \equiv H(x_1, x_2, z_j)$, $j = 1,2,3$ are harmonic functions in the corresponding systems of coordinates. Then, the corresponding displacement-stress field becomes:

$$u_\alpha = \frac{\left[m_1 t_1 F_2 - m_2 t_2 F_1\right]_{,\alpha}}{m_2 t_2 - m_1 t_1} + \epsilon_\alpha^\gamma F_{3,\gamma}, \ \alpha = 1,2 \tag{58}$$

$$u_3 = \frac{t_1 t_2}{m_2 t_2 - m_1 t_1}\left(\frac{\partial F_2}{\partial z_2} - \frac{\partial F_1}{\partial z_1}\right) \tag{59}$$

$$\frac{\sigma_{3\alpha}}{c_{44}} = \frac{t_1 t_2}{m_2 t_2 - m_1 t_1}\left[\left(1 + m_1\right)\frac{\partial F_2}{\partial z_2} - \left(1 + m_2\right)\frac{\partial F_1}{\partial z_1}\right]_{,\alpha} + \epsilon_\alpha^\gamma t_3 \frac{\partial^2 F_3}{\partial z_3 \partial x_\gamma}, \ \alpha = 1,2 \tag{60}$$

$$\frac{\sigma_{33}}{c_{44}} = \frac{1}{m_2 t_2 - m_1 t_1}\left[t_1\left(1 + m_1\right)\frac{\partial^2 F_2}{\partial z_2^2} - t_2\left(1 + m_2\right)\frac{\partial^2 F_1}{\partial z_1^2}\right] \tag{61}$$

$$\begin{aligned} \sigma_{11} = \frac{-c_{44} t_1 t_2}{m_2 t_2 - m_1 t_1}&\left[t_2\left(1 + m_1\right)\frac{\partial^2 F_2}{\partial z_2^2} - t_1\left(1 + m_2\right)\frac{\partial^2 F_1}{\partial z_1^2}\right] \\ &-\left(c_{11} - c_{12}\right)\left[\frac{\left(m_1 t_1 F_2 - m_2 t_2 F_1\right)_{,22}}{m_2 t_2 - m_1 t_1} + F_{3,12}\right] \end{aligned} \tag{62}$$

$$\begin{aligned} \sigma_{22} = \frac{-c_{44} t_1 t_2}{m_2 t_2 - m_1 t_1}&\left[t_2\left(1 + m_1\right)\frac{\partial^2 F_2}{\partial z_2^2} - t_1\left(1 + m_2\right)\frac{\partial^2 F_1}{\partial z_1^2}\right] \\ &-\left(c_{11} - c_{12}\right)\left[\frac{\left(m_1 t_1 F_2 - m_2 t_2 F_1\right)_{,11}}{m_2 t_2 - m_1 t_1} - F_{3,12}\right] \end{aligned} \tag{63}$$

$$\frac{\sigma_{12}}{c_{11} - c_{12}} = \frac{\left(m_1 t_1 F_2 - m_2 t_2 F_1\right)_{,12}}{m_2 t_2 - m_1 t_1} + 0{,}5\left(F_{3,11} - F_{3,22}\right) \tag{64}$$

It is seen that the above expressions simplify across the plane $x_3 = 0$ since the subscripts j can be dropped for G_j and H_j, so we get $F_1 = F_2 = G_{,1} + H_{,2}$, $F_3 = G_{,2} - H_{,1}$. Introducing the notation:

$$\begin{aligned} g\left(x_1, x_2, x_3\right) &= \frac{\partial G\left(x_1, x_2, x_3\right)}{\partial x_3} \\ h\left(x_1, x_2, x_3\right) &= \frac{\partial H\left(x_1, x_2, x_3\right)}{\partial x_3} \end{aligned} \tag{65}$$

the displacements and stresses in the plane of symmetry are found as:

$$\begin{aligned} u_1 &= \left[g_{,3}\left(x_1, x_2, x_3\right)\right]_{x_3=0} \\ u_2 &= \left[h_{,3}\left(x_1, x_2, x_3\right)\right]_{x_3=0} \\ u_3 &= 0 \end{aligned} \tag{66}$$

$$\frac{\sigma_{31}^{\pm}}{c_{44}} = C^*\left[g_{,33} + \kappa\left(g_{,22} - h_{,12}\right)\right]_{x_3=0^{\pm}} \tag{67}$$

$$\frac{\sigma_{32}^{\pm}}{c_{44}} = C^*\left[h_{,33} + \kappa\left(h_{,11} - g_{,12}\right)\right]_{x_3=0^{\pm}} \tag{68}$$

$$\frac{\sigma_{33}}{c_{44}} = -D^*\left[g_{,31} + h_{,32}\right]_{x_3=0} \tag{69}$$

$$\sigma_{11} = E^*\left[g_{,31} + h_{,32}\right]_{x_3=0} - \left(c_{11} - c_{12}\right)\left[h_{,32}\right]_{x_3=0} \tag{70}$$

$$\sigma_{22} = E^*\left[g_{,31} + h_{,32}\right]_{x_3=0} - \left(c_{11} - c_{12}\right)\left[g_{,31}\right]_{x_3=0} \tag{71}$$

$$\sigma_{12} = 0{,}5\left(c_{11} - c_{12}\right)\left[g_{,32} + h_{,31}\right]_{x_3=0} \tag{72}$$

where:

$$\begin{aligned} C^* &= \frac{t_1 t_2\left(m_2 - m_1\right)}{m_2 t_2 - m_1 t_1} = \frac{\sqrt{c_{11} c_{33}}\ t_+}{\sqrt{c_{11} c_{33}} + c_{44}} \\ \kappa &= 1 - \frac{t_3}{C^*} \\ D^* &= \frac{A_-}{\sqrt{c_{11} c_{33}} + c_{44}}, \quad E^* = \sqrt{\frac{c_{11}}{c_{33}}}\ \frac{A_-\left(A_+ + c_{44}\right)}{\sqrt{c_{11} c_{33}} + c_{44}} \end{aligned} \tag{73}$$

It follows immediately from the boundary conditions (35)-(38) that the unknown potentials g and h can be determined from:

$$\left.\begin{aligned}\left[g_{,3}(x_1,x_2,x_3)\right]_{x_3=0^+} &= -\bar{u}_1^{(0)}+\varepsilon_1-\omega_3 x_2\\ \left[h_{,3}(x_1,x_2,x_3)\right]_{x_3=0^+} &= -\bar{u}_2^{(0)}+\varepsilon_2+\omega_3 x_1\end{aligned}\right\}(x_1,x_2)\in S \quad (74)$$

$$\left.\begin{aligned}\left[g_{,33}+\kappa\left(g_{,22}-h_{,12}\right)\right]_{x_3=0^+}&=0\\ \left[h_{,33}+\kappa\left(h_{,11}-g_{,12}\right)\right]_{x_3=0^+}&=0\end{aligned}\right\}(x_1,x_2)\in R^2-S \quad (75)$$

It is easy to seen from a comparison of the above conditions that the formulation given by Eqs. (74) and (75) is inverse to that for the crack problem involving shear tractions (Kassir and Sih, 1975).

To obtain integral equations, the two-dimensional Fourier technique will be used (see the method developed by Kaczyński (1999)). The space harmonic functions f, g and h are represented by Fourier's integrals (Sneddon, 1972):

$$\begin{bmatrix}f(\mathbf{x})\\ g(\mathbf{x})\\ h(\mathbf{x})\end{bmatrix}=\iint_S \frac{\exp\left[-x_3|\boldsymbol{\xi}|+i(x_\alpha\xi_\alpha)\right]}{|\boldsymbol{\xi}|^2}\begin{bmatrix}A_f(\boldsymbol{\xi})\\ A_g(\boldsymbol{\xi})\\ A_h(\boldsymbol{\xi})\end{bmatrix}dS_{\boldsymbol{\xi}} \quad (76)$$

where $\boldsymbol{\xi}=(\xi_1,\xi_2)\in S$, $|\boldsymbol{\xi}|=\sqrt{(\xi_1)^2+(\xi_2)^2}$.

From the boundary condition (56), in view of (52), one finds immediately that:

$$A_f(\xi_1,\xi_2)=\frac{1}{4\pi^2 c_{44}(m_2-m_1)}\iint_S \sigma_{33}^+(\eta_1,\eta_2)\exp\left[-i(\eta_\alpha\xi_\alpha)\right]d\eta_1 d\eta_2 \quad (77)$$

Accordingly, the conditions in equation (75) yield a system for the remaining unknown functions $A_g(\boldsymbol{\xi})$ and $A_h(\boldsymbol{\xi})$:

$$\begin{bmatrix}1-\frac{\kappa(\xi_2)^2}{|\boldsymbol{\xi}|^2} & \frac{\kappa\xi_1\xi_2}{|\boldsymbol{\xi}|^2}\\ \frac{\kappa\xi_1\xi_2}{|\boldsymbol{\xi}|^2} & 1-\frac{\kappa(\xi_1)^2}{|\boldsymbol{\xi}|^2}\end{bmatrix}\begin{bmatrix}A_g(\xi_1,\xi_2)\\ A_h(\xi_1,\xi_2)\end{bmatrix}= \quad (78)$$
$$=\frac{1}{4\pi^2 c_{44}C^*}\iint_S\begin{bmatrix}\sigma_{31}^+(\eta_1,\eta_2)\\ \sigma_{32}^+(\eta_1,\eta_2)\end{bmatrix}\exp\left[-i(\eta_\alpha\xi_\alpha)\right]d\eta_1 d\eta_2$$

which has the solution:

$$4\pi^2 c_{44}C^*(1-\kappa)\begin{bmatrix}A_g(\boldsymbol{\xi})\\ A_h(\boldsymbol{\xi})\end{bmatrix}=\begin{bmatrix}1-\frac{\kappa(\xi_1)^2}{|\boldsymbol{\xi}|^2} & -\frac{\kappa\xi_1\xi_2}{|\boldsymbol{\xi}|^2}\\ -\frac{\kappa\xi_1\xi_2}{|\boldsymbol{\xi}|^2} & 1-\frac{\kappa(\xi_2)^2}{|\boldsymbol{\xi}|^2}\end{bmatrix}\cdot \quad (79)$$
$$\cdot\iint_S\begin{bmatrix}\sigma_{31}^+(\eta_1,\eta_2)\\ \sigma_{32}^+(\eta_1,\eta_2)\end{bmatrix}\exp\left[-i(\eta_\alpha\xi_\alpha)\right]d\eta_1 d\eta_2$$

Equations (77) and (79) may be substituted into (76) to give:

$$2\pi c_{44}(m_2-m_1)f_{,3}(\mathbf{x})=-\iint_S\frac{\sigma_{33}^+(\boldsymbol{\xi})}{|\mathbf{x}-\boldsymbol{\xi}|}dS_{\boldsymbol{\xi}} \quad (80)$$

$$-2\pi t_3 c_{44}g_{,3}(\mathbf{x})=\iint_S\frac{\sigma_{31}^+(\boldsymbol{\xi})}{|\mathbf{x}-\boldsymbol{\xi}|}dS_{\boldsymbol{\xi}}-\kappa\iint_S\frac{\sigma_{31}^+(\boldsymbol{\xi})(x_2-\xi_2)^2}{|\mathbf{x}-\boldsymbol{\xi}|^3}dS_{\boldsymbol{\xi}} \quad (81)$$
$$+\kappa\iint_S\frac{\sigma_{32}^+(\boldsymbol{\xi})(x_1-\xi_1)(x_2-\xi_2)}{|\mathbf{x}-\boldsymbol{\xi}|^3}dS_{\boldsymbol{\xi}}$$

$$-2\pi t_3 c_{44}h_{,3}(\mathbf{x})=\iint_S\frac{\sigma_{32}^+(\boldsymbol{\xi})}{|\mathbf{x}-\boldsymbol{\xi}|}dS_{\boldsymbol{\xi}}-\kappa\iint_S\frac{\sigma_{32}^+(\boldsymbol{\xi})(x_1-\xi_1)^2}{|\mathbf{x}-\boldsymbol{\xi}|^3}dS_{\boldsymbol{\xi}} \quad (82)$$
$$+\kappa\iint_S\frac{\sigma_{31}^+(\boldsymbol{\xi})(x_1-\xi_1)(x_2-\xi_2)}{|\mathbf{x}-\boldsymbol{\xi}|^3}dS_{\boldsymbol{\xi}}$$

where $\sigma_{3j}^+(\boldsymbol{\xi})=\sigma_{3j}(\xi_1,\xi_2,0^+), \boldsymbol{\xi}=(\xi_1,\xi_2,0)\in S$ and $|\mathbf{x}-\boldsymbol{\xi}|$ is a distance between the field point $\mathbf{x}=(x_1,x_2,x_3)$ and the integration point $\boldsymbol{\xi}=(\xi_1,\xi_2,0)$. Moreover, in deriving the above expressions, use has been made of the following integrals (Erdelyi, 1954):

$$\iint_{R^2}\frac{\exp i\left[(x_\alpha-\eta_\alpha)\xi_\alpha\right]}{|\boldsymbol{\xi}|}d\xi_1 d\xi_2=\frac{2\pi}{\sqrt{(x_1-\eta_1)^2+(x_2-\eta_2)^2}}$$
$$\iint_{R^2}\frac{\exp i\left[(x_\alpha-\eta_\alpha)\xi_\alpha\right](\xi_1)^2}{|\boldsymbol{\xi}|^3}d\xi_1 d\xi_2=\frac{2\pi(x_2-\eta_2)}{\left(\sqrt{(x_1-\eta_1)^2+(x_2-\eta_2)^2}\right)^3}$$
$$\iint_{R^2}\frac{\exp i\left[(x_\alpha-\eta_\alpha)\xi_\alpha\right](\xi_2)^2}{|\boldsymbol{\xi}|^3}d\xi_1 d\xi_2=\frac{2\pi(x_1-\eta_1)}{\left(\sqrt{(x_1-\eta_1)^2+(x_2-\eta_2)^2}\right)^3} \quad (83)$$
$$\iint_{R^2}\frac{\exp i\left[(x_\alpha-\eta_\alpha)\xi_\alpha\right]\xi_1\xi_2}{|\boldsymbol{\xi}|^3}d\xi_1 d\xi_2=\frac{-2\pi(x_1-\eta_1)(x_2-\eta_2)}{\left(\sqrt{(x_1-\eta_1)^2+(x_2-\eta_2)^2}\right)^3}$$

Now enforcing the displacement boundary conditions (55) and (74), we arrive at the governing singular integral equations of Newtonian potential type to determine the interface stresses $\sigma_{3j}^+|s, j=1,2,3$:

$$A\iint_S\frac{\sigma_{33}^+(\xi_1,\xi_2)d\xi_1 d\xi_2}{\sqrt{(x_1-\xi_1)^2+(x_2-\xi_2)^2}}=\bar{u}_3^{(0)}-\varepsilon_3+\omega_2 x_1-\omega_1 x_2 \quad (84)$$

$$B\iint_S\left\{\frac{\sigma_{31}^+(\xi_1,\xi_2)}{\sqrt{(x_1-\xi_1)^2+(x_2-\xi_2)^2}}\left[1-\kappa\frac{(x_2-\xi_2)^2}{(x_1-\xi_1)^2+(x_2-\xi_2)^2}\right]+\right.$$
$$\left.+\kappa\frac{\sigma_{32}^+(\xi_1,\xi_2)(x_1-\xi_1)(x_2-\xi_2)}{\left(\sqrt{(x_1-\xi_1)^2+(x_2-\xi_2)^2}\right)^3}\right\}d\xi_1 d\xi_2=\bar{u}_1^{(0)}-\varepsilon_1+\omega_3 x_2$$

(85)

$$B\iint_S \left\{ \frac{\sigma_{32}^+(\xi_1,\xi_2)}{\sqrt{(x_1-\xi_1)^2+(x_2-\xi_2)^2}}\left[1-\kappa\frac{(x_1-\xi_1)^2}{(x_1-\xi_1)^2+(x_2-\xi_2)^2}\right]+ \right.$$

$$\left. +\kappa\frac{\sigma_{31}^+(\xi_1,\xi_2)(x_1-\xi_1)(x_2-\xi_2)}{\left(\sqrt{(x_1-\xi_1)^2+(x_2-\xi_2)^2}\right)^3}\right\} d\xi_1 d\xi_2 = \bar{u}_2^{(0)} - \varepsilon_2 - \omega_3 x_1 \tag{86}$$

in which κ is given by Eqs. (73), and the material constants A, B are:

$$A=\frac{m_2 t_2 - m_1 t_1}{2\pi c_{44}(m_2-m_1)}=\frac{\sqrt{c_{11}c_{33}}+c_{44}}{2\pi c_{44}c_{33}t_+}$$
$$B=\frac{1}{2\pi c_{44}t_3}=\frac{1}{\pi\sqrt{2c_{44}(c_{11}-c_{12})}} \tag{87}$$

It is worth mentioning that the results obtained can be used in the case of isotropic material (see the relations (16)). Then the constants in the governing equations become:

$$\kappa=\frac{\lambda+\mu}{2(\lambda+2\mu)}=\frac{1}{4(1-\nu)}$$
$$A=\frac{\lambda+3\mu}{4\pi\mu(\lambda+2\mu)}=\frac{3-4\nu}{8\pi\mu(1-\nu)} \tag{88}$$
$$B=\frac{1}{2\pi\mu}$$

which are in agreement with those obtained by Silovanyuk (1984).

After the stresses σ_{3j} acting on the inclusion side S^+ have been determined from the solution of the above integral equations, the full-space elastic field can be calculated from the harmonic potentials f, g, h via relations (80)-(83) with the use of Eqs. (42)-(48) and (57)-(64). For completeness, the kinematical parameters of the inclusion ε_j and ω_j can be found from the conditions (33), (39) and (34), (40), respectively.

For an arbitrary simply connected domain S bounded by a smooth contour the governing equations can be solved by an analytic-numerical method developed in Kit et al. (1989). Explicit solutions are possible for elliptical shapes of S by assuming polynomial right-hand sides. The typical case of a circular anticrack in a uniform normal tension at infinity will be considered in the next section.

4. EXAMPLE

The stress state of a transversely isotropic space containing in the plane of isotropy a sealed circular rigid inclusion (anticrack) $s=\left\{(x_1,x_2,0): r\equiv\sqrt{(x_1)^2+(x_2)^2}\le a\right\}$ is investigated by assuming that:

$$\sigma_{33}^{(t)}(\infty)=\sigma_3=\text{const.}>0,\quad \sigma_{31}^{(t)}(\infty)=\sigma_{32}^{(t)}(\infty)=0 \tag{89}$$

The displacement solution to the basic equations (7) and (8) of 0-problem with conditions (89) is readily obtained as:

$$u_\alpha^{(0)}(x_1,x_2,x_3)=-D\sigma_3 x_\alpha,\ \alpha=1,2$$
$$u_3^{(0)}(x_1,x_2,x_3)=D_3\sigma_3 x_3 \tag{90}$$

Where:

$$D=\frac{c_{13}}{c_{33}(c_{11}+c_{12})-2(c_{13})^2}$$
$$D_3=\frac{c_{11}+c_{12}}{c_{33}(c_{11}+c_{12})-2(c_{13})^2} \tag{91}$$

Now invoking the displacement boundary conditions (see Eqs. (27)-(29)), we are dealing with the symmetric part of the perturbed problem described by Eqs. (35)-(40) in which

$$\bar{u}_\alpha(x_1,x_2)=-D\sigma_3 x_\alpha,\ \alpha=1,2 \tag{92}$$

The exact analytical solution of the governing system (85) and (86) with the RHS given by (92) is achieved if we take the unknown stresses in the form

$$\sigma_{3\alpha}^+(x_1,x_2)=\frac{b_{0\alpha}+b_{1\alpha}x_1+b_{2\alpha}x_2}{\sqrt{a^2-r^2}},\ \alpha=1,2 \tag{93}$$

where $b_{j\alpha},\ j=0,1,2,\ \alpha=1,2$ are unknown constants.

Substituting these expressions into Eqs. (85) and (86), and next using the formulas for resulting integrals given by Vorovich et al. (1974), the equality of two polynomials of the first order is obtained. Equating the terms of the left and right hands with the same powers of x_1 and x_2 yields a system of linear algebraic equations, solving which we get the following formulas for the unknown coefficients $b_{j\alpha}$:

$$b_{0\alpha}=-\frac{4c_{44}t_3}{\pi(2-\kappa)}\varepsilon_\alpha,\ \alpha=1,2$$
$$b_{12}=-b_{21}=\frac{4}{\pi}c_{44}t_3\omega_3 \tag{94}$$
$$b_{11}=b_{22}=-\frac{4}{\pi}c_{44}DC^*\sigma_3$$

Now the equilibrium conditions provided in (39) and (40) can be employed, from which we get (as might be expected):

$$\varepsilon_1=\varepsilon_2=\omega_3=0 \tag{95}$$

Thus, expression (93) can be simplified as:

$$\sigma_{3\alpha}^+(x_1,x_2)=-\frac{4c_{44}DC^*\sigma_3 x_\alpha}{\pi\sqrt{a^2-r^2}},\ \alpha=1,2 \tag{96}$$

From above it follows that the problem in hand is axially symmetric.

On substitution of formulas (96) into Eqs. (81) and (82), we find:

$$g_{,3}(\mathbf{x})=\frac{2DC^*\sigma_3}{\pi^2 t_3}\left(\psi_1+\kappa\psi_{1,2}x_2-\kappa\psi_{2,2}x_1\right)$$
$$h_{,3}(\mathbf{x})=\frac{2DC^*\sigma_3}{\pi^2 t_3}\left(\psi_2+\kappa\psi_{2,2}x_1-\kappa\psi_{1,1}x_2\right) \tag{97}$$

Here $\psi_\alpha, \alpha = 1,2$ are the simple-layer potentials defined by:

$$\psi_\alpha(\mathbf{x})=\iint_S \frac{\xi_\alpha\, d\xi_1\, d\xi_2}{|\mathbf{x}-\boldsymbol{\xi}|\sqrt{a^2-(\xi_1)^2-(\xi_2)^2}} \tag{98}$$

They can be expressed in elementary functions by utilizing the results of Fabrikant (1989, 1991) as:

$$\psi_\alpha(\mathbf{x}) = \pi x_\alpha \left[\sin^{-1}\left(\frac{a}{l_2}\right) - \frac{a\sqrt{(l_2)^2 - a^2}}{(l_2)^2} \right] \tag{99}$$

where $l_2 = 0{,}5\left[\sqrt{(r+a)^2 + (x_3)^2} + \sqrt{(r-a)^2 + (x_3)^2} \right]$.

Having the above explicit expressions, a complete solution to the problem under study is available. Since the resulting formulas are lengthy, we omit them here to save the space of the paper. To investigate the singular behavior of anticrack-border stresses, however, the shear radial and normal stresses in the plane $x_3 = 0^{\mp}$ are calculated as follows:

$$\sigma_{3r}\left(r, 0^{\pm}\right) = \begin{cases} \mp \dfrac{\beta_r \sigma_3 r}{\pi\sqrt{a^2 - r^2}}, & 0 \le r < a \\ 0, & r > a \end{cases} \tag{100}$$

$$\sigma_{33}\left(r, 0^{\pm}\right) = \begin{cases} -\dfrac{1}{2}\beta_3 \sigma_3, & 0 \le r < a \\ \dfrac{\beta_3 \sigma_3}{\pi}\left[\dfrac{a}{\sqrt{r^2 - a^2}} - \sin^{-1}\left(\dfrac{a}{r}\right) \right], & r > a \end{cases} \tag{101}$$

in which β_r, β_3 are given by:

$$\beta_r = \frac{4c_{13}\sqrt{c_{11}c_{44}\left[c_{11}c_{33} - c_{13}(2c_{44} + c_{13}) + 2c_{44}\sqrt{c_{11}c_{33}}\right]}}{\left[c_{33}(c_{11} + c_{12}) - 2(c_{13})^2\right]\left(\sqrt{c_{11}c_{33}} + c_{44}\right)} \tag{102}$$

$$\beta_3 = \frac{4c_{13}\, c_{44}\left(\sqrt{c_{11}c_{33}} - c_{13}\right)}{\left[c_{33}(c_{11} + c_{12}) - 2(c_{13})^2\right]\left(\sqrt{c_{11}c_{33}} + c_{44}\right)} \tag{103}$$

These results reveal that the stresses near the anticrack front $r = a$ have the classical singularity $r^{-1/2}$ as in the fracture mechanics of conventional elastic materials. Strictly speaking, singularities in σ_{3r} occur at the points on the edge of the disc where $r = a^-$, and in σ_{33} – at the points exterior to the disc where $r = a^+$. It indicates that there are two major mechanisms controlling the material cracking around the inclusion front:

– exfoliation of the material from the surface of the inclusion described by the stress singularity coefficients:

$$S_{\mathrm{II}}^{\pm} = \lim_{r \to a^-} \sqrt{2\pi(a - r)}\, \sigma_{3r}\left(r, 0^{\pm}\right) = \mp \beta_r \sigma_3 \sqrt{a/\pi} \tag{104}$$

– mode I fracture in the immediate vicinity of the edge of the disc characterized by the stress intensity factor:

$$K_{\mathrm{I}} = \lim_{r \to a^+} \sqrt{2\pi(r - a)}\, \sigma_{33}(r, 0) = \beta_3 \sigma_3 \sqrt{a/\pi} \tag{105}$$

The above-mentioned parameters can be used in conjunction with a suitable failure criterion.

Finally, in the special case of isotropy (see (16)), we arrive at the solution in which the constants β_r, β_3 become:

$$\beta_r = \frac{4\lambda(\lambda + 2\mu)}{(\lambda + 3\mu)(3\lambda + 2\mu)} = \frac{8\nu(1 - \nu)}{(1 + \nu)(3 - 4\nu)} \tag{106}$$

$$\beta_3 = \frac{4\lambda\mu}{(\lambda + 3\mu)(3\lambda + 2\mu)} = \frac{4\nu(1 - 2\nu)}{(1 + \nu)(3 - 4\nu)} \tag{107}$$

in complete agreement with Kassir and Sih (1968).

5. CONCLUSIONS

In the present paper we have studied the elastostatic three-dimensional problem of an anticrack of arbitrary shape embedded in a transversely isotropic space and subjected to external loads. Using the method of potential functions, the mixed boundary-value problems in the antisymmetric and symmetric statement have been reduced to some mixed problems of potential theory. Further, the governing boundary integral equations were obtained with the unknown stress jumps across the rigid inclusion. As an illustration, a closed-form solution was given and discussed for a circular rigid inclusion subjected to normal tension at infinity. The analytical expressions of stress fields in the anticrack plane show the characteristic $r^{-1/2}$ singular behaviour near the edge of the disc and indicate that either the matrix fractures near the inclusion according to mode I or the mechanism of shear fracture acts (separation of the material from the inclusion surface).

REFERENCES

1. **Berezhnitskii L.T., Panasyuk V.V. , Stashchuk N.G.** (1983), *The Interaction of Rigid Linear Inclusions and Cracks in a Deformable Body* (in Russian), Naukova Dumka, Kiev.
2. **Chaudhuri R.A**. (2003), Three-dimensional asymptotic stress field in the vicinity of the circumference of a penny-shaped discontinuity, *International Journal of Solids and Structures*, Vol. 40, 3787-3805.
3. **Chaudhuri R.A**. (2012), On three-dimensional singular stress field at the front of a planar rigid inclusion (anticrack) in an orthorhombic mono-crystalline plate, *International Journal of Fracture*, Vol. 174, 103-126.
4. **Ding H., Chen W., Zhang L.** (2006), Elasticity of Transversely Isotropic Materials*, Solid Mechanics and its Applications*, Vol. 126, Springer, The Netherlands.
5. **Erdelyi A.** (1954), *Tables of Integral Transforms,* Vol.1, McGraw-Hill, New York.
6. **Fabrikant V.I.** (1989), *Applications of Potential Theory in Mechanics: A Selection of New Results*, Kluwer Academic Publishers, Dordrecht.
7. **Fabrikant V.I.** (1991), *Mixed Boundary Value Problems of Potential Theory and their Applications*, Kluwer Academic Publishers, Dordrecht.
8. **Kaczyński A.** (1993),On the three-dimensional interface crack problems in periodic two-layered composites, *International Journal of Fracture*, Vol. 62, 283-306.
9. **Kaczyński A.** (1999), Rigid sheet-like interface inclusion in an infinite bimaterial periodically layered composite, *Journal of Theoretical and Applied Mechanics,* Vol. 37, 81-94.
10. **Kanaun S.K., Levin V.M. (**2008), *Self-Consistent Methods for Composites. Vol. 1: Static Problems*, *Solid Mechanics and its Applications*, Vol. 148, Springer,The Netherlands, Dordrecht.
11. **Kassir M.K., Sih G.C.** (1968), Some three-dimensional inclusion problems in elasticity, *International Journal of Solids and Structures*, Vol. 4, 225-241.
12. **Kassir M.K., Sih G.C.** (1975), *Three-Dimensional Crack Problems,* Mechanics of Fracture 2, Noordhoof Int. Publ., Leyden.
13. **Khai M.V.** (1993), *Two-Dimensional Integral Equations of the Newton-Potential Type and their Applications* (in Russian), Naukova Dumka, Kiev.
14. **Kit G.S., Khai M.V.** (1989), *Method of Potentials in Three-Dimensional Problems of Thermoelasticity of Bodies with Cracks* (in Russian), Naukova Dumka, Kiev.
15. **Mura T.** (1982), *Micromechanics of Defects in Solids*, Martinus Nijhoff, The Hague.

16. **Panasyuk V.V., Stadnik M.M., Silovanyuk V.P.** (1986), *Stress Concentrations in Three-Dimensional Bodies with Thin Inclusions* (in Russian), Naukova Dumka, Kiev.
17. **Podil'chuk Y.N.** (1997), Stress state of a transversely-isotropic body with elliptical inclusion, *International Applied Mechanics,* Vol. 33, 881-887.
18. **Rahman M**. (1999), Some problems of a rigid elliptical disc-inclusion bonded inside a transversely isotropic space, *Transactions of the ASME Journal of Applied Mechanics,* Vol. 66, 612-630.
19. **Rahman M**. (2002), A rigid elliptical disc-inclusion, in an elastic solid, subjected to a polynomial normal shift, *Journal of Elasticity*, Vol. 66, 207-235.
20. **Rogowski B.** (2006), *Inclusion Problems for Anisotropic Media*, Technical University of Lodz, Lodz.
21. **Selvadurai A.P.S.** (1982),On the interaction between an elastically embedded rigid inhomogeneity and a laterally placed concentrated force, *Journal of Applied Mathematics and Physics (ZAMP),* Vol. 33, 241-250.
22. **Shodja H.M., Ojaghnezhad F.** (2007), A general unified treatment of lamellar inhomogeneities, *Engineering Fracture Mechanics*, Vol. 74, 1499-1510.
23. **Silovanyuk V.P.** (1984), A rigid lamellar inclusion in elastic space, *Materials Science,* Vol. 20, 482-485.
24. **Silovanyuk V.P.** (2000), *Fracture of Prestressed and Transversely Isotropic Bodies with Defects*, National Academy of Science of Ukraine, Physico-Mechanical Institute named G.V. Karpenko, Lviv.
25. **Sneddon I.N.** (1972), *The Use of Integral Transforms*, McGraw-Hill, New York.
26. **Ting T.C.T.** (1996), *Anisotropic Elasticity: Theory and Applications*, Oxford University Press, New York.
27. **Vorovich I.I., Alexandrov V. V., Babeshko V. A.** (1974), *Non-classical Mixed Boundary Problems of Theory of Elasticity* (in Russian), Nauka, Moscow.

REAL FLIGHT DEMONSTRATION OF PITCH AND ROLL CONTROL FOR UAV CANYON FLIGHTS

Cezary KOWNACKI*

*Faculty of Mechanical Engineering, Department of Automatics and Robotics, Bialystok University of Technology,
ul. Wiejska 45C, 15-351 Bialystok, Poland

c.kownacki@pb.edu.pl

Abstract: The paper presents results of an experiment prepared to validate the autonomous control of obstacle avoidance designed for a micro UAV to fly in urban canyons. The idea of the obstacle avoidance assumes usage of two miniature laser rangefinders responsible for obstacle detection and range measurement. Measured ranges from obstacles placed on both sides of UAV can be used to simultaneous control of desired roll and pitch angles. Such combination of controls allows achieving high agility of UAV, because during a maneuver of obstacle avoidance UAV can make a turn and climb at the same time. In the experiment, controls of roll and pitch angles were verified separately to ensure high reliability of results and clearance of UAV behavior in the real flight. Because of lack of appropriate objects, which can be used as obstacles, laser rangefinders were directed vertically to the ground instead of the original horizontal configuration. So sensors determine ranges from the ground during a descent flight of UAV, and if their values are lower than defined threshold, it could be interpreted as obstacle detection. The experiment results present UAV behavior adequate to designed controls of roll and pitch angle. The vehicle turns in the opposite direction to the sensing axis of laser rangefinder detecting an obstacle and starts climbing when both sensors detect obstacles at the same range below the threshold.

Key words: Obstacle Avoidance, Autonomous Control, Unmanned Air Vehicle, Reactive Control, Urban Canyon

1. INTRODUCTION

Unmanned aerial vehicles have become increasingly popular within the last few years. They are applicable successfully in many different areas of civil engineering and research fields where fast, reliable and low cost inspection is expected (Campoy et al., 2009). Most common use of micro and mini UAVs is undertaking patrol flights for police, fire-brigades and foresters. Using UAVs allows observing with much wider field of vision than it is possible on the ground. Even so UAV is still associated mostly with military applications such as intelligence where only larger vehicle can be used. To change this meaning, micro and mini UAV must become more autonomous and intelligent to be able to operate in zone nearby humans being, i.e. in urban environments. It would be possible if UAV was able to fly autonomously and safely for surrounding objects ensuring the lowest risk of collision. So the primary aim of autonomous UAV is being able to see and avoid any obstacle. Today technology still seems to be limiting possibilities to solve this problem entirely for micro UAV. In spite of that many researchers are still attempting to demonstrate autonomous UAV having at least partial possibilities of obstacle avoidance (Beyeler et al., 2009; Griffiths et al., 2007]. Such case of partial obstacle avoidance is an autonomous flight in unknown canyons (Kownacki, 2009; Kownacki, 2010; Kownacki, 2011; Hrabar et al., 2006). It assumes that UAV flies between obstacles like buildings or canyon walls. Therefore, it requires continuous determining ranges from two obstacles on both sides of the canyon. Then the main task of control system is to place flying vehicle in the center of canyon. Ranges from canyon walls can be determined by Fig. 1):

- a pair of laser rangefinders (Kownacki, 2009; 2010; 2011),
- optical flow sensors or miniature cameras (Beyeler et al., 2009; Griffiths et al., 2007; Hrabar et al., 2006; 2009),
- a single camera and optical flow processing (Andert et al., 2010).

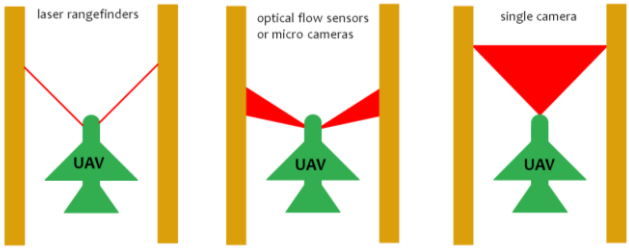

Fig. 1. Range measurement applied in realization of the flight in a canyon

In (Hrabar et al., 2009) authors presented results of vehicle flights in urban canyons using two miniature cameras and optical flow image processing. The results were impressive, but in this case the authors used a vertical taking off and landing vehicle, which are able to hover or to fly extremely slowly. So it was much easier than realizing an autonomous flight in a canyon with a fixed wing vehicle. Therefore, more attractive results, there are in (Griffiths et al., 2007) where authors used a delta wing vehicle equipped with a laser rangefinder applied to the frontal obstacle avoidance, and two optical flow sensor applied to the flight in a canyon. The idea of vehicle control is similar as in the previous work, but this time the vehicle flies much faster. Both works use the range measurement derived from optical flow technique. Similarly to the others optical measurements, it also remains sensitive to exposure parameters like a light intensity and diversity of the image frame. Hence, we aim to realize the control of UAV flight across the canyon in a little bit different way. Instead

of optical flow sensors or cameras we employed two tiny laser rangefinders (MLR100) (Kownacki, 2009; 2010; 2011). These robust sensors determine ranges from obstacles at the vehicle front on both sides of the canyon (Fig. 2) (Kownacki, 2009; 2010; 2011). The effective sensing range is about 150 meters without disturbances. The limitation of proposed method is that it is blind to narrow frontal obstacles. It can be accepted since the method was designed especially for canyon flights, where the obstacles are to the sides. So it is well suited to autonomous urban flights and this is the main aim of the research.

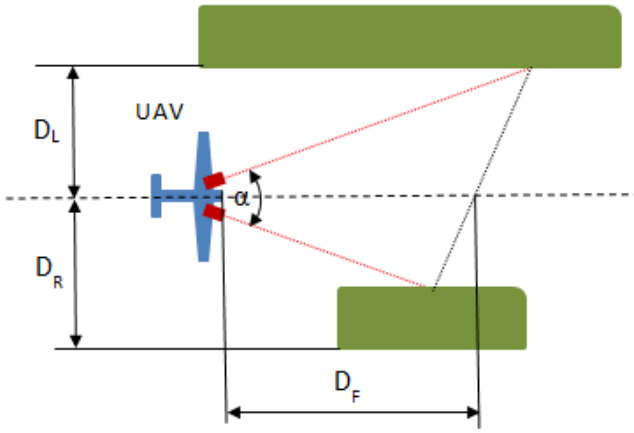

Fig. 2. The idea of flight in a canyon based on two laser rangefinders

The whole idea of the proposed concept of autonomous obstacle avoidance and flight in urban canyons was already fully described in the author's pervious works (Kownacki, 2009; 2010; 2011). Results derived from flight simulations present perfect possibilities of the concept, and it state, that it can be implemented in a real micro UAV easily. Now we would like to show results from the experiment using a real micro UAV, which verifies usefulness of the concept.

2. THE CONTROL OF ROLL AND PITCH ANGLES

According to the concept presented in (Kownacki, 2011), ranges from obstacles acquired by two laser rangefinders can be used as inputs of the roll angle control. The roll angle control splits into two levels. The high level contains two PID loops responsible for determining desired roll angles corresponding to the appropriate sensor. Range from the left sensor expressed in y axis of the vehicle body frame is the input of the first PID loop producing positive desired roll angle, what will make UAV turning right. Similarly, range from the right sensor expressed in y axis of the vehicle body frame is the input of the second loop with negative desired roll angle on the output and this time it will make UAV turning left. Of course, the resultant desired roll angle is a sum of both PID loops' outputs. The low level of roll angle control keeps the error between actual and desired angle nearby zero, and it is a part of original autopilot firmware. If both PIDs' outputs are zero, the low level roll control will acquire desired roll angle from navigation task. The avoidance controller toggles the source of desired roll angle (Kownacki, 2011). The high and low level of roll angle control required a modification of original autopilot firmware code, what was possible using software delivered by autopilot manufacturer. Figure 3 presents the high of control of roll angle designed for autonomous flight in urban canyon. Work (Kownacki, 2011) present in details all necessary calculations applied in two blocks called respectively: frame translation and filtration, and avoidance controller. The first block is responsible for disturbances filtration and translation of measured ranges from body frame to the north east down frame. In this way, we eliminate roll and pitch angle impact on obstacle relative position. In turn, the second block i.e. avoidance controller is responsible for switching the roll control from navigation mode to obstacle avoidance mode (Kownacki, 2011).

The control of roll angle is responsible for turns, and it operates in both cases: obstacle avoidance and flight in urban canyon. What will happen, when frontal obstacle is appearing, and both sensors are measuring the same range? If the PIDs have the same output values only with opposite signs, the resultant desired roll angle will be equal zero and the vehicle will not turn. To solve this problem, we extend the obstacle avoidance control described in works (Kownacki, 2009; 2010) with the control of desired pitch angle (Kownacki, 2011).

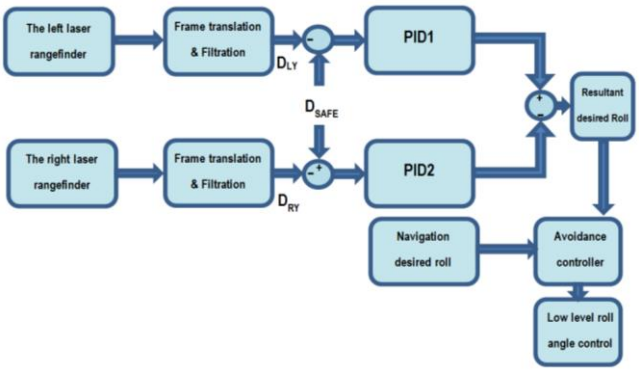

Fig. 3. The structure of high level of designed roll angle control

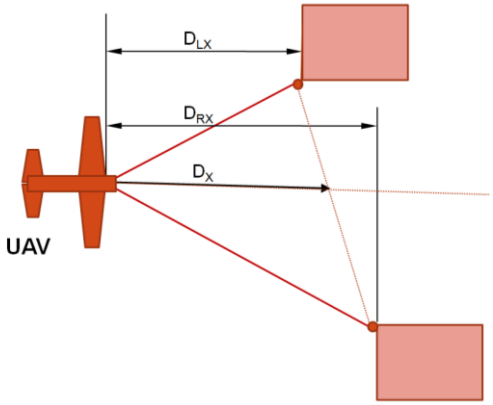

Fig. 4. The averaged range D_X from obstacles expressed in *x* axis of UAV body frame

The control of desired pitch angle uses the averaged value of ranges from obstacles expressed in x axis of the vehicle body frame (Fig. 4). It also splits into two levels. The high level contains one PID loop, which generates a positive desire pitch angle, when the average range value in x axis droops below the threshold value. Hence UAV is able to climb without making a turn. The roll angle control and pitch control angle operates simultaneously, so it is possible to combine turning with climbing. This is a significant advantage of the proposed obstacle avoidance control. The averaged range in x axis is the input of the PID loop. The low level control of pitch angle is responsible for realizing desired pitch

angle derived from the PID or navigation task of autopilot. The avoidance controller also toggles the source of desired pitch.

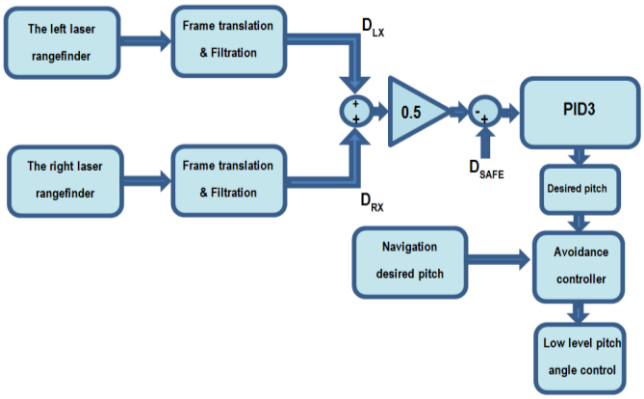

Fig. 5. The structure of high level of designed pitch angle control

Because both designed roll and pitch controls are inputs for the low level control loops, it secures aircraft against unstability in the case of severe roll or pitch command.

Fig. 5 presents the diagram explaining the structure of the high level of desired pitch control.

3. REAL FLIGHT EXPERIMENT

A real flight experiments verify both controls of pitch and roll angles. The serious problem of scenario setting can be met in experiments respecting obstacle avoidance with fixed wing UAV. Nobody wants to crash vehicle during the first flight or to make any damage in third party objects. Fixed wing UAV flies safely at minimum altitude about 50 meters. It ensures that the vehicle will not be under the influence of turbulence created by lifting wind from the warm ground. Hence obstacles should have with 50 meters height at least. Because of lack of such objects satisfying safety conditions, we decided to test pitch and roll controls with distinctive sensors assembly. Measurement axes of both sensors are directed vertically to the ground level instead of the original horizontal placement from figure 2. Measurement axes were turned outside slightly about 20^0 (Fig. 6) to decrease accidental reflections of laser beams from the vehicle body.

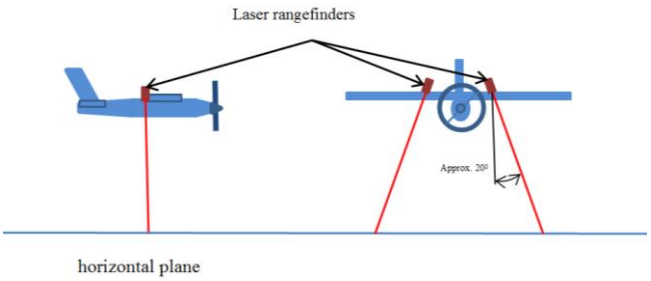

Fig. 6. The laser rangefinders assembly applied in the experiment

The sensors assembly allows applying the ground level as an obstacle, when UAV will be decreasing its altitude. Because the maximum measurement range is about 150 meters, UAV can fly safely at altitudes higher than 50 meters during the experiment. Of course it will not be the case with tall obstacles such as trees, but it will be well suited to urban canyon flights above trees-tops level. Fig. 7 presents the principle of the experiment. The experiment splits into two parts. The first part verifies the roll control, and we test the pitch control in the second.

During both parts of the experiment, UAV receives a command from GCS (Ground Control Station) to lower its altitude. It causes decrement of measured range, and this is synonymous with obstacle detection. In the first part of the experiment we disabled the left laser rangefinder, so the UAV behavior should be the same as in the case of obstacle detection on the vehicle right. UAV should start turning left when measured range droops below the threshold value Dsafe.

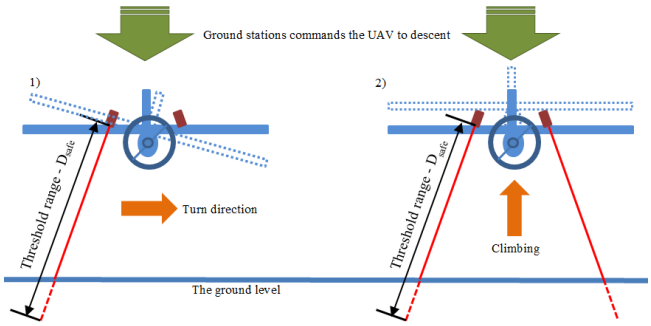

Fig. 7. The verification of roll and pitch controls designed for obstacle avoidance and flight in urban canyon. Orange arrows present expected response of UAV control to actual range measurement: 1) the roll control part of the experiment, 2) the pitch control part of the experiment

In the second part of the experiment, both sensors are left enabled. Then only the desired pitch angle derived from the high level of pitch control should be different from zero. The resultant desired roll angle should be zero, because the left and the right sensor measure the same range. It results only in UAV climbing, what overrides the command from GCS.

Fig. 8. Test UAV with two laser rangefinders fixed to its wings

4. RESULTS

Fig. 8 presents the flight path recorded during the first part of the experiment, i.e. verification of the roll control. We used four waypoints to create requested flight path to be realized

by autopilot navigation task.

Fig. 9 clearly presents a turn associated with obstacle avoidance (marked dashed line in yellow color) produced by the designed roll control, while the vehicle is flying below 79 meters, the altitude related with threshold Dsafe = 85 meters (79 /cos 20^0) (Fig. 6 and 10). The desired altitude set up by GCS command is equal 60 meters (at 390 second) and next 45 meters (at 410 second) (Fig. 10). When the vehicle returns to fly at an altitude higher than 79 meters, the requested flight path becomes valid again (orange dashed line in Fig. 9). Next Figures present flight parameters stored in the data log of autopilot. They describe the roll control operation and the vehicle behavior in details.

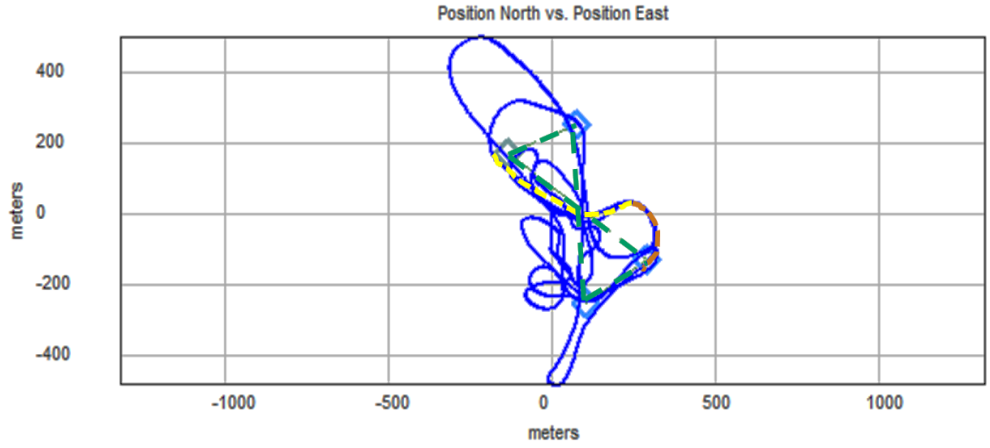

Fig. 9. The flight path recorded during verification of the roll control. The green dashed line represents the requested flight path to be realized by the autopilot navigation task. The yellow dashed line represents turn corresponding to obstacle avoidance, while UAV is flying at an altitude below 79 meters (related with Dsafe=85 meters). The orange dashed line represents a return to realize the requested flight path after climbing above the altitude of 79 meters

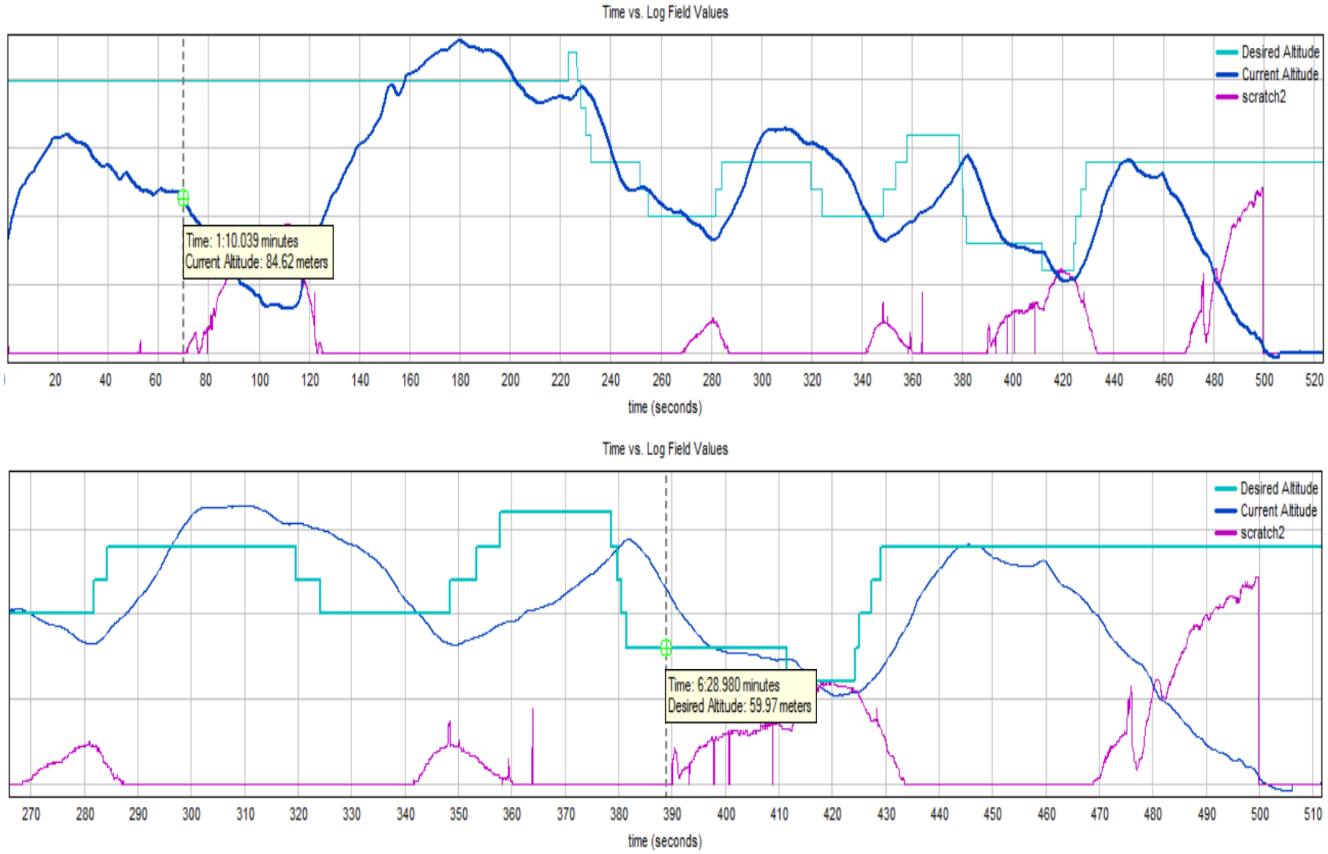

Fig. 10. The flight parameters recorded during the roll control verification. The current altitude plot is navy blue, the desired altitude plot is blue and the plot of current error value (scratch2) of PID associated with the right sensor is violet

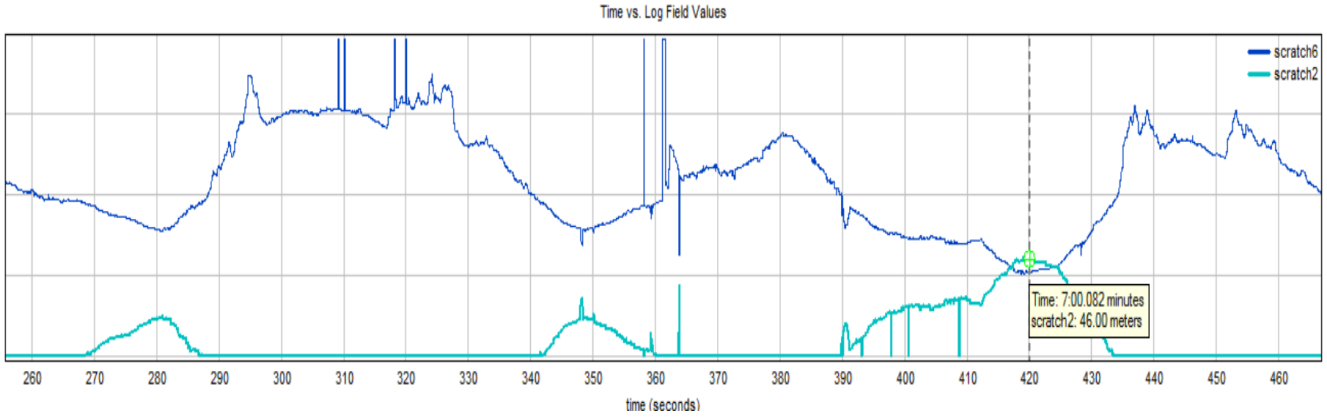

Fig. 11. Plots of scratch2 and scratch6 are respectively the current error value of PID associated with the right sensor and the range measured by the right sensor

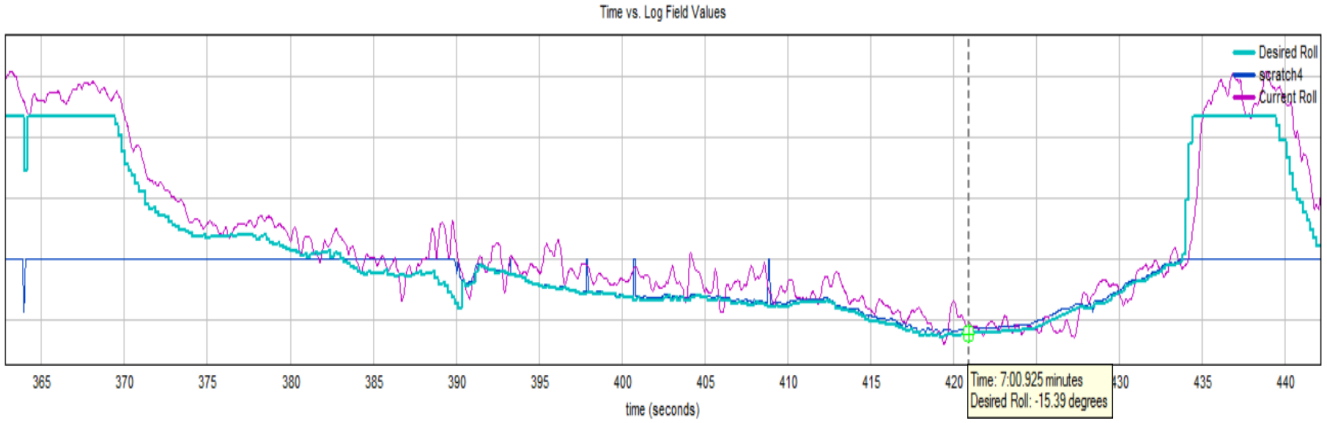

Fig. 12. Plots of the desired roll angle, the current roll angle and scratch4 – the current output value of PID associated with the right sensor. The current PID output value is the same as the resultant desired roll angle, i.e. the output of the high level of roll control

In Fig. 10 we can see, that the current error value of the PID is greater than zero, while the current altitude is lower than 79 meters. The error reaches a maximum value 47 meters at the current altitude being equal 40 meters, while the measured range is 38 meters (419 second of the flight) (Fig. 11). The turn presented in Fig. 9 takes place between 390 and 433 second of the experiment flight. So we can notice in Fig. 12, that the output of PID associated with the right sensor is different from zero in the time range between 390 and 433 second of the flight. In the same range of time, the desired roll angle is equal the PID output. After the 430 second of the flight, UAV climbs above 79 meters (the desired altitude is 105 meters), and the low level of roll control is switched to navigation task. UAV returns to realize the requested flight path.

Fig. 13 presents the flight path recorded during the second part of the experiment. A red line represents the part of flight path where the pitch control was tested. The vehicle was flying over flat terrain.

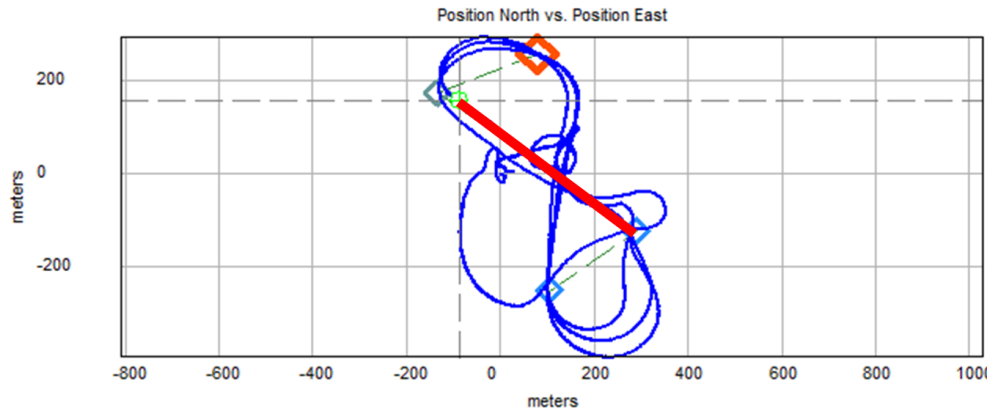

Fig. 13. The flight path recorded during verification of the pitch control

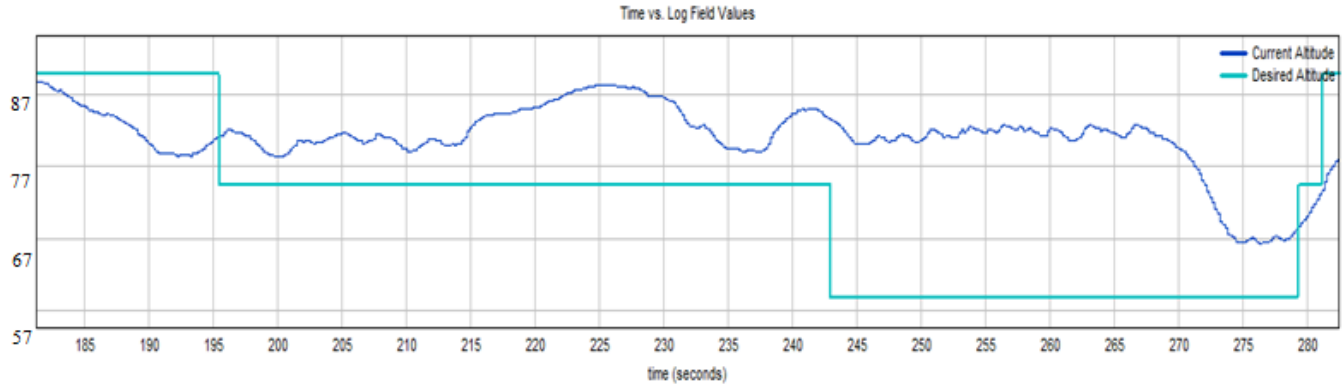

Fig. 14. The upper graph is a plot of current altitude and the bottom graph is a plot of desired altitude.
The current altitude never decreased below 80 meters even the desired altitude was 60 meters (at 243 second of the flight)

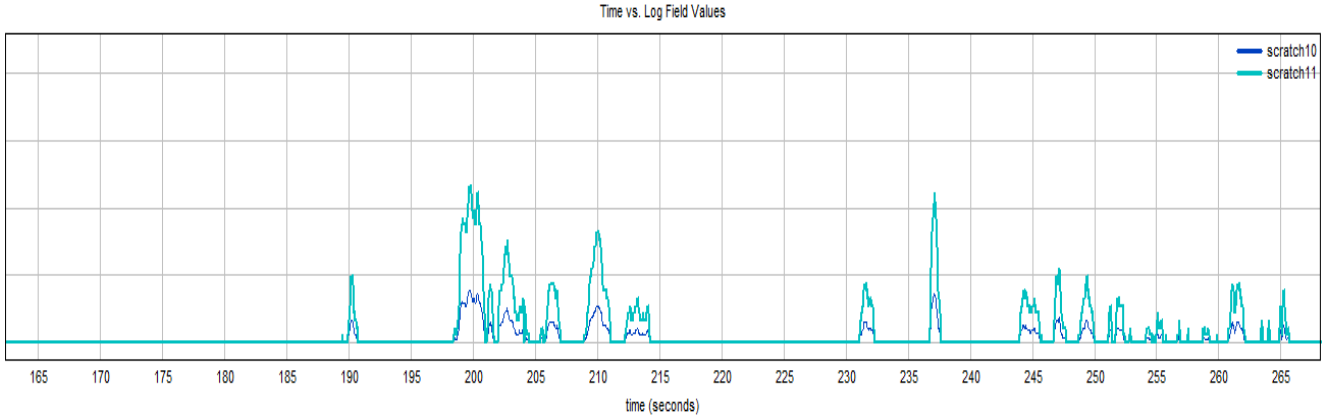

Fig. 15. Plots of scratch 10 and scratch 11 represents respectively the current error and the current output of the PID from the high level of pitch control

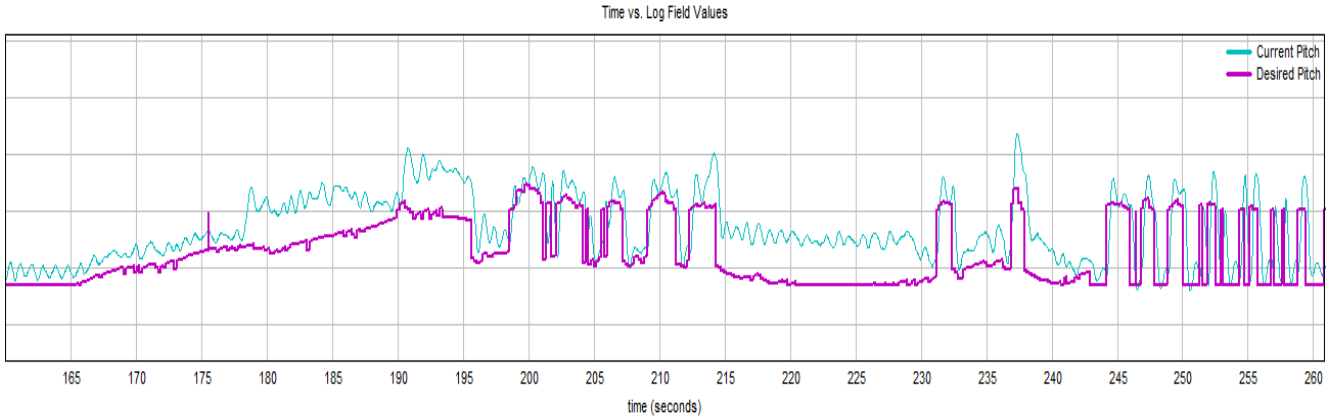

Fig. 16. Plots of current pitch and desired pitch related with Fig. 15

This time also the change of flight altitude simulates the obstacle detection. Fig. 14 presents the plot of current altitude and the plot of desired altitude recorded during the second part of the experiment.

It can be clearly underscore that the current altitude never decreased below 80 meters, while the desire altitude was decreasing from 90 to 60 meters with 15 meters steps. The current altitude oscillates around approx. 81 meters, what means that, the pitch control is being switched from obstacle avoidance to navigation task periodically. The altitude level equals 81 meters defines the moment of switching. Fig.15 presents plots of scratch 10 and scratch 11, which are standing respectively for the current error and the current output of the PID from the high level of pitch control. It is obvious that these plots correlate directly with the oscillation of current altitude.

The second part of experiment presents reliable view of UAV behavior and the pitch control operation. We can see that, in spite of command of desired altitude decreasing, UAV is not able to fly below specified level. This is a strong proof of the pitch control effectiveness, because the test flight can be easily compared with UAV level flight over a hill. In the test, we decreased desired altitude and UAV was not able to descent, what corresponds to UAV climbing as a consequence of measured range decreasing while desired altitude is constant.

5. CONCLUSIONS

Results of the both parts of the experiments present that the roll and pitch controls operation meets fully and unquestionably all assumptions made during the design stage of proposed obstacle avoidance. UAV behavior was exactly the same as it should be in real obstacle avoidance. If the one laser rangefinder detects the range from obstacle below the safe threshold, UAV will make a turn in the opposite direction to the obstacle location. If both laser rangefinders detect the same low range from obstacles, UAV will climb to fly over them. These two possibilities of flight control are fundamentals of autonomous flight of unmanned aerial vehicle. Moreover, the simultaneous combination of turn and climbing is available using the proposed obstacle avoidance strategy, what increases vehicle agility. It is because of the obvious fact that climbing can highly reduce the ground projection of turn radius. The equipment used in the experiment can be easily built into micro unmanned aerial vehicle with a wing span about 1 meter, and it is truly impressive success of the research.

REFERENCES

1. **Andert F., Adolf F., Goormann L., Dittrich J.** (2010), Autonomous Vision-Based Helicopter Flights Through Obstacle Gates, *Journal of Intelligent & Robotic Systems*, Vol. 57, Issue 1-4, 259-280.
2. **Beyeler A., Zufferey J.C., Floreano D.** (2009), Vision based control of near-obstacle flight, *Autonoums Robots*, Vol. 27, No 3, 201-219.
3. **Campoy P., Correa J. F., Mondragón I., Martínez C., Olivares M., Mejías L., Artieda J., Valavanis K., Oh P., Pieg L.** (2009), *Computer Vision Onboard UAVs for Civilian Tasks, Unmanned Aircraft Systems*, Springer Netherlands, Vol. 54, Issue 1-3, 105-135.
4. **Griffiths S., Saunders J., Curtis A., Barber B., McLain T., Beard R.** (2007), *Obstacle and Terrain Avoidance for Miniature Aerial Vehicles, Advances in Unmanned Aerial Vehicles, State of the Art and the Road to Autonomy*, Spinger, 2007, 213-244.
5. **Hrabar S. E., Sukhatme G. S.** (2006), Optimum camera angle for optic flow-based centering response, *IEEE/RSJ International Conference on Intelligent Robots and Systems (IROS)*, 3922 – 3927.
6. **Hrabar S. E., Sukhatme G. S.** (2009), Vision-Based Navigation Through Urban Canyons, *Journal of Field Robotics*, Vo.26, Issue 5, 431 – 452.
7. **Kownacki C.** (2009), Guidance and obstacle avoidance of MAV in uncertain urban environment, *European Micro Aerial Vehicle Conference and Flight Competition 2009: EMAV'2009 Delft*, CD-ROM.
8. **Kownacki C.** (2010), Algorithm development for flight control of micro aircraft in uncertain urban environment, Acta Mechanica et Automatica, Vol. 4, No. 3, 87-93, (in Polish).
9. **Kownacki C.** (2011), *Obstacle avoidance strategy for Micro Aerial Vehicle, Advances in aerospace guidance, navigation and control*, Berlin: Springer-Verlag, 117-135.
10. **Todorovic S., Nechyba M.C.** (2004), A Vision System for Intelligent Mission Profiles, *IEEE Transactions On Vehicular Technology*, Vol. 53, No. 6, 1713–1725.

The research was funded by funds of the Polish Ministry of Science and Higher Education for science in 2008-2010 as a developmental project No O R00 0059 06. Very big thanks to Jaroslaw Hajduk for his invaluable help in flights and vehicle assembling.

EFFECT OF HEAT TREATMENT AND PLASMA NITRIDING ON CORROSION RESISTANCE OF 440B MARTENSITIC STAINLESS STEEL

Magdalena ŁĘPICKA*, Małgorzata GRĄDZKA-DAHLKE*

*Faculty of Mechanical Engineering, Department of Materials and Biomedical Engineering, Bialystok University of Technology, ul. Wiejska 45 C, 15-351 Bialystok, Poland

m.lepicka@doktoranci.pb.edu.pl, m.dahlke@pb.edu.pl

Abstract: Reliability and durability assurance poses a serious challenge for surgical instruments manufacturers. Hard working conditions, such as intermittent contact with body fluids and hard bone tissues, as well as necessity to undergo frequent sterilisation processes, induce constant research into solutions capable of ensuring high wear resistance while maintaining satisfactory imperviousness to corrosion. Plasma nitriding is marked as the modern corrosion resistance improving method suitable for surgical instruments steels. The paper presents findings from the heat treated and plasma nitrided AISI 440B (PN EN or DIN X90CrMoV18) steel corrosion resistance studies. Three conventionally heat treated (quenched with tempering in 250, 390 or 605°C) and three additionally plasma nitrided in N_2:H_2 reaction gas mixture (50:50, 35:65 and 20:80 ratio, respectively) specimens groups were examined. Furthermore, the authors evaluated the effect of machining - polishing and sandblasting - on investigated steel corrosion resistance. Microscopic observations and electrochemical corrosion tests were performed using a variety of analytical techniques. Results showed that, in comparison to conventional heat treatment, plasma nitriding of 440B stainless steel does not significantly affect its corrosive characteristics as far as the uniform nitride layer over the entire detail surface is obtained. The layer heterogeneity results in intensification of corrosion processes, making the material even more susceptible to corrosion than after conventional heat treatment, and contributing to severe, visible even with the unaided eye damages development.

Key words: Stainless Steels, Corrosion, Heat Treatment, Plasma Nitriding, Surgical Instruments

1. INTRODUCTION

Reliability and durability are the most important factors in surgical instruments manufacturing. Hard working conditions, such as intermittent contact with body fluids and hard bone tissues, necessity to undergo sterilisation processes, impose constant research into solutions able to ensure high wear resistance while maintaining resistance to corrosion (Marciniak, 1992; Paszenda and Tyrlik-Held, 2003). To assure the required durability of surgical instruments, cutting instruments are often made of martensitic stainless steels (PN-EN ISO 7153-1:2002; PN-EN 10088-1:2005; Paszenda and Tyrlik-Held, 2003). Made of these, the instruments are subjected to heat treatment to obtain high hardness and, as a result, sufficient wear resistance (Marciniak, 1992). Moreover, thermo chemical surface modification techniques such as anti-wear layers deposition are commonly applied in the technological process (Głowacka, 1996; Rudnik, 1996). Alas, not all solutions traditionally used in machining are allowed in biomedical applications because of the peril of corrosion characteristics deterioration. Therefore, when searching for ways to improve operative surgical instruments characteristics, resistance to wear and corrosion ought be accounted.

Considering cutting surgical instruments, the commonly used surface modification technique is the plasma nitriding. The method can be briefly described as impingement of a flux of ions to the surface of the treated parts. The treated batch surface is activated by glow discharge which increases the efficiency of the process. Due to the concentration gradient, nitrogen diffuses into the treated workpiece. As a result of chemical reactions, the mechanical properties of the material are modified at both the top and subsurface level (Tuckart et al., 2007).

Conventional plasma nitriding conducted in the temperatures from 500 to 600°C significantly improves the microhardness and the tribological properties of stainless steels (Tuckart et al., 2007), but also causes a significant decrease in their corrosion resistance (Li and Bell, 2006; Hi et al., 2008a; Xi et al., 2008b). Corrosion resistance reduction is due to the exudation of CrN precipitates, which creation results in the chromium content depletion in the nitrided surface matrix (Xi et al., 2008a). This phenomenon can be observed only in certain treatment temperature range, causing the sensitivity of steel to intergranular corrosion. To avoid this negative effect, a thermo chemical heat treatment method called low temperature plasma nitriding (LTN) has been established (Bell and Sun, 2002). The highest corrosion resistance of martensitic stainless steels is usually obtained when tempering below 425°C (Grubb, 2011). Typically, the LTN nitriding is carried out at a temperature of about 420°C, since it allows to obtain phase called nitrogen expanded austenite – γ_N (Mingolo et al., 2006; Samandi et al., 1993). Its main features include very high hardness, high wear resistance, and – above all – excellent corrosion resistance (Li and Bell, 2006; Xi et al., 2008a). As opposed to, the martensitic stainless steels heat treatment at the temperatures in the range from 245 to 540°C may lead to increased susceptibility to stress corrosion or hydrogen embrittlement (Grubb, 2011). The direct cause of this phenomena are the chromium-rich α' phase precipitates in the ferritic matrix. This

formation, likewise the occurring at above 20% chromium content hard and brittle α-phase formation, can be characterised by low transformation kinetics and can often be avoided (Hedström, 2007). The ensuing α' precipitates cause not only grain boundaries chromium content depletion, but also induce considerable internal stresses. Occurence of the tensile stress in the material fosters hydrogen, fatigue and stress corrosion processes existence (Baszkiewicz and Kamiński, 2006). In consequence, the stainless steel is no longer stainless.

The substantiation for tempering temperatures exceeding 245°C avoidance of martensitic stainless steels is precipitation of chromium carbide $Cr_{23}C_6$ (Yang et al., 2007). Typically, it is formed at temperatures from 500 to 800°C, but if the grain boundaries contain carbides seeds its precipitation can begin even at 300°C (Baszkiewicz and Kamiński, 2006). In case of chromium carbide presence, steel becomes susceptible to intergranular corrosion. Chromium diffusion from grain interiors to their boundaries is characterised by much greater dynamics than the carbon diffusion. This directly causes chromium content reduction; in the adjacent to the grain boundary layer total chromium content can reach even nought, on average remains at the level of 2% (Baszkiewicz and Kamiński, 2006). Chemical segregation leads to formation of anodic areas – the low in chrome boundaries – and cathodic areas – chromium-rich grain interiors. Moreover, the anode to cathode ratio is highly disadvantageous – cathodic areas are many times larger than the anodic ones, leading to a dynamic material dissolution at the grain boundaries.

In view of this information, selection of appropriate heat treatment parameters for steels used for surgical instruments appears as an important issue when ensuring optimal performance characteristics.

The aim of this study was to evaluate the corrosion resistance of heat treated at different temperatures and then plasma nitrided martensitic stainless steel.

2. MATERIALS AND METHODS

AISI 440B (PN-EN X90CrMoV18) stainless steel was selected as the substrate material. The chemical composition of the tested material is presented in Tab. 1.

Tab. 1. 440B stainless steel chemical compotision (wt%)[21]

	C	Mn	Si	S	P
EDX	0.95	-	0.40	0.39	0.30
PN-EN 10088 -1:2005	0.85 ÷0.95	max 1.00	max 1.00	max 0.040	max 0.030
	Cr	**Mo**	**V**	**Fe**	
EDX	18.00	0.95	0.06	remnant	
PN-EN 10088 -1:2005	17.00 ÷19.00	0.90 ÷1.30	0.07 ÷0.12	remnant	

The research material has been prepared accordingly to the technological process applied for surgical drill bits manufacturing. The substrate material was heat treated (series 1-6) and plasma nitrided (series 7-12). The effect of tempering temperature and surface modification on subjected material corrosion resistance has been investigated.

Specimens were subjected to heat treatment, consisting of quenching in oil, from an austenitising temperature of 1030°C, and tempering. The tempering temperature is extremely important when considering desired properties of the steel. Tempering in low temperatures (up to 250°C) provides the highest hardness. However, the following procedure, plasma nitriding, is performed at higher temperatures. Nevertheless, a fairly wide heat treatment temperature range is not recommended for martensitic stainless steels due to their corrosion resistance, as it was described in the Introduction. Therefore, in this study three tempering temperatures: 250, 390 and 605°C were considered. Samples were prepared in form of discs with 8 mm diameter and 6 mm height. They were subjected to mechanical surface treatment consisting of sandblasting, typical for surgical instruments manufacturing process, or polishing, to assess if lesser surface roughness provides significantly better corrosion resistance.

Specimens from series 7 to 12 were additionally subjected to plasma nitriding carried out at temperature from 380 to 400°C, under working pressure of 200 Pa. The whole process lasted 2 hours. In order to optimize nitriding process conditions, the process was repeated in three different concentrations of treatment gases inside working chamber, namely:

a) 50% H, 50% N, i.e. 100 ml/min H_2 + 100 ml/min N_2,
b) 35% H, 65% N, i.e. 70 ml/min H_2 + 130 ml/min N_2,
c) 20% H, 80% N, i.e. 40 ml/min H_2 + 160 ml/min N_2.

All analysed samples are summarised in Tab. 2.

Tab. 2. Specimens summary table

Series no.	Quenching temperature (°C)	Tempering temperature (°C)	Surface machining	Plasma nitriding; working gas compositon
1	1030	250	polishing	-
2			sandblasting	-
3	1030	390	polishing	-
4			sandblasting	-
5	1030	605	polishing	-
6			sandblasting	-
7	1030	250	polishing	50% H_2 + 50% N_2
8			sandblasting	
9			polishing	35% H_2 + 65% N_2
10			sandblasting	
11			polishing	20% H_2 + 80% N_2
12			sandblasting	

Polarisation studies were performed electrochemically in 0.9 wt% NaCl aqueous solution to investigate the electrochemical corrosion behaviour of the conventionally heat treated and the plasma nitrided specimens. Potentiodynamic polarisation scans were carried out using a computer controlled ATLAS 9833 (Atlas-Sollich) corrosion system. The NaCl solution was maintained at 25°C open to air. A constant scan rate of 0.001 V/s was used. All potentials were measured with respect to a saturated calomel electrode (SCE, 0.242 V in 25°C vs. SHE at 25°C) as the reference electrode. The set consisted also of platinum auxiliary electrode and a working electrode (sample). Theoretic circular area of 50.24 mm^2 was left to maintain contact with the testing solution. Tests were performed according to the following procedures: (i)

clean sample from organic and non-organic debris in ultrasonic cleaner using ethyl alcohol in room temperature (20°C), (ii) rinse sample with deionised water, (iii) place the sample in a three-neck flask pre-filled with 250 cm^3 fresh, un-deaerated 0.9% NaCl solution, (iv) stabilise for 120 minutes, (v) perform polarisation scan from -0.6 V to a potential of up to +2 V. Test control, data logging and processing were achieved by a POL99-win computer software.

The morphology and pit structure of specimens were studied by scanning electron microscopy (SEM - Hitachi S-3000N microscope), confocal laser scanning microscopy (CLSMO – Olympus LEXT OLS 4000 microscope) and energy-dispersive X-ray analysis (EDX).

3. RESULTS AND DISCUSSION

The applied heat and thermo chemical treatments parameters resulted in a change in the corrosion resistance of tested steel, as shown in Figs. 1-5.

The first group of investigated samples consisted of conventionally heat treated specimens. Figure 1 illustrates the polarisation curves of 440B steel tempered in 250°C. It is noticeable that sandblasted sample is characterised by significantly lower corrosion currents density and corrosion potential shift towards positive potentials, what is typical of better corrosion resistance. In investigated measuring range, no transpassivation has been observed. Curves are mild, free of current jumps.

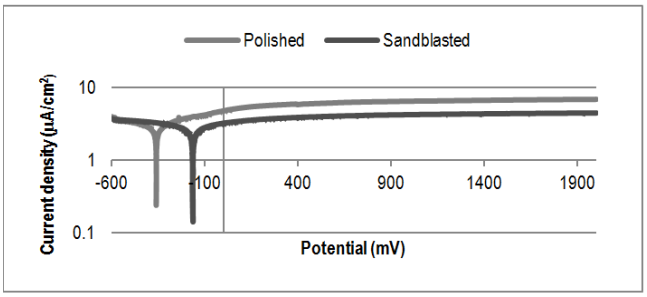

Fig. 1. Polarisation curves of tempered in 250°C 440B steel in 0.9 wt% NaCl solution (undeaerated, unstirred)

A similar trend can be observed considering steel tempered in 390°C (Fig. 2). However, in this case current density jumps can be noticed for both polished and sandblasted specimens. Such behaviour is characteristic for corrosion pits nucleation. What is important, current density jump of sandblasted sample occurs at significantly greater corrosion potential value than of the polished one. This is a factor indicating better corrosion resistance of non-polished material.

It could be expected that surface roughness reduction obtained by polishing would have a positive influence on examined steel corrosion characteristics. However, an inverse relationship can be observed. This fact can be explained by sandblast induced material reinforcement. Workpiece surface sandblasting entails preferred from both corrosion resistance and hardness increase compressive stresses emergence. It can be deduced that sandblasted areas do not conduce to pits nucleation, and even layer of corrosion products seems to confirm this thesis. In contrast, surface grinding and polishing can lead to microscopic local defects development, which act as pits nucleation areas. As a result, sandblasted 440B steel exhibits better corrosion properties than the polished one.

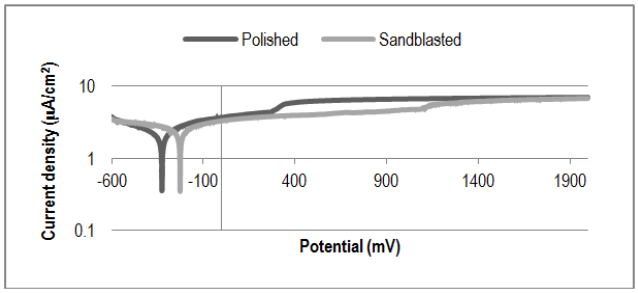

Fig. 2. Polarisation curves of tempered in 390°C 440B steel in 0.9 wt% NaCl solution (undeaerated, unstirred)

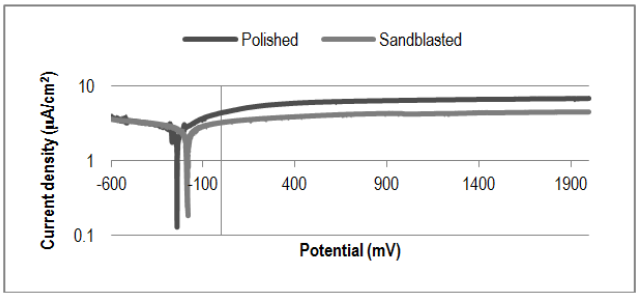

Fig. 3. Polarisation curves of plasma nitrided in 35:65 H_2:N_2 gaseous mixture 440B steel in 0.9 wt% NaCl solution (undeaerated, unstirred)

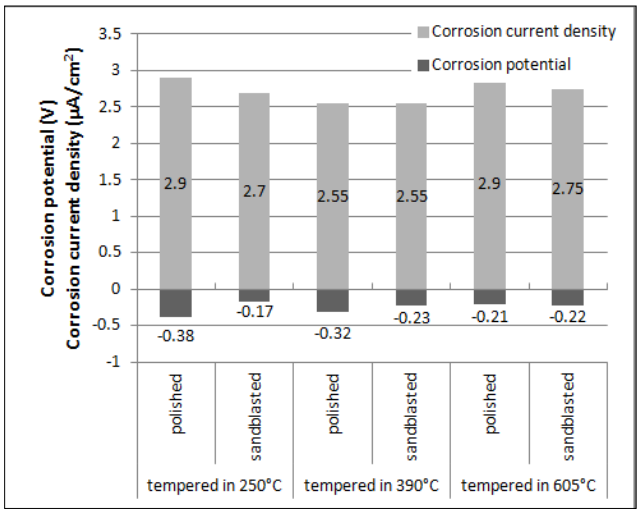

Fig. 4. Conventionally heat treated specimens corrosion potentials and corrosion currents densities

Analysis of nitrided samples polarisation curves also showed that the initial state of material surface has an effect on its corrosion characteristics. In the first two nitriding options – with reactive gas mixture 50:50 and 35:65 H_2 to N_2 ratio – the initial specimens surface topography affected their corrosion resistance after the nitriding process, while the third reaction gas mixture variation (80:20) had virtually no impact on considered properties.

For example, the plasma nitrided in 35:65 H_2:N_2 gaseous mixture sandblasted steel exhibited slightly greater corrosion potential and lower corrosion current value (Fig. 3). The curves are mild, after some elapsed experiment time both of them achieve rectilin-

earity – the polished one approximately at 200mV, and the sandblasted one – after reaching 0 mV.

Figs. 4 and 5 present corrosion potentials and corrosion current densities obtained from graphical Tafel approximation. According to the findings, plasma nitriding can be recommended as a corrosion resistance enhancing method only for details that have already been polished. Admittedly, a significant decrease in corrosion currents is not achieved, but the curve shift towards positive potentials is observed. Therefore, the polarisation characteristics can be modified, what leads to passivation time extension. In this case, when applying plasma nitriding regardless of the reactive gaseous mixture composition, an additional approximately 0.2 V cathodic polarisation potential is provided.

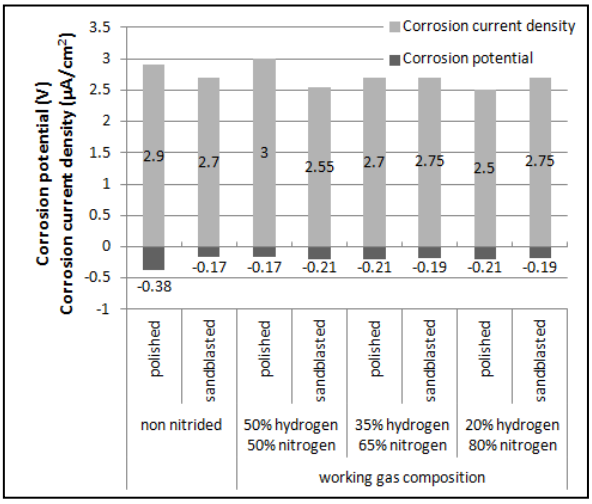

Fig. 5. Tempered in 250°C specimens after conventional heat treatment or plasma nitriding - corrosion potentials and corrosion currents densities comparison

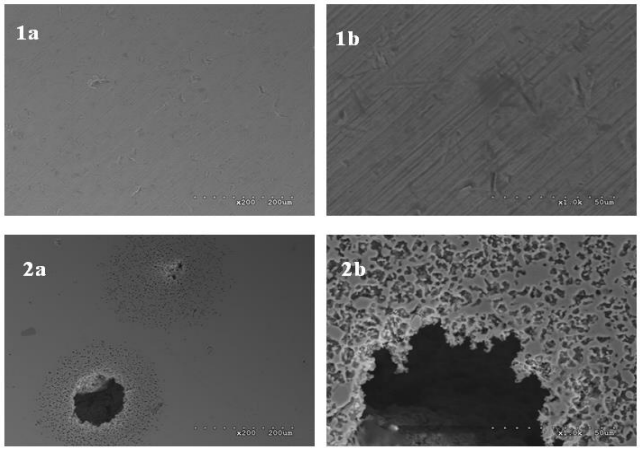

Fig. 6. Corroded surface morphologies of tempered in 250°C 440B steel after potentiodynamic polarisation scans; 1a, 1b – sandblasted steel, 2a, 2b – polished steel. SEM photographs, 200× (1a, 2a) and 1000× (1b, 2b) magnification

The performed microscopic observations also confirmed greater corrosion resistance of sandblasted specimens. Fig. 6 illustrates tempered in 250°C sandblasted and polished specimens surfaces after corrosion analyses. It can be noticed that sandblasted sample surface (Fig. 6, 1b) is free of corrosion pits; at higher magnification only machining traces are visible. The observed corrosion was of uniform nature; the red-brown colour of saline solution indicates presence of iron (III) oxide-hydroxide. The superficial material perforation was present round the vast corrosion damages (Fig. 6, 2a). If the solution is not mixed, formation of fine corrosion pits around the greater damages may be induced by dynamic processes occurring in the directly contacting sample surface aqueous environment.

Different corrosion damages were observed on plasma nitrided specimens. Relatively small samples dimensions (height = 6 mm, diameter = 8 mm) constitute difficulties in obtaining uniform nitrided layers on surrounded by long edges flat surfaces. Irregular reactive mixture propagation makes impossible to obtain planned layer thickness and composition. Specimen rims present distinct surface layer, while the core remains in the same state as before the whole process began or some traces of transitional layer can be observed (Fig. 7). Obtained findings indicate that the nitriding gas concentration has a significant effect on the extent of nitrided layer zone. It can be observed that the greater the hydrogen to nitrogen ratio disproportion is, the less satisfactory surface modification is achieved.

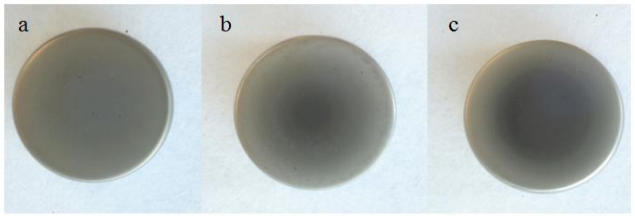

Fig. 7. Plasma nitrided polished specimens; a – 50% H_2:50% N_2, b – 35% H_2:65% N_2, c – 20% H_2:80% N_2; macro photographs

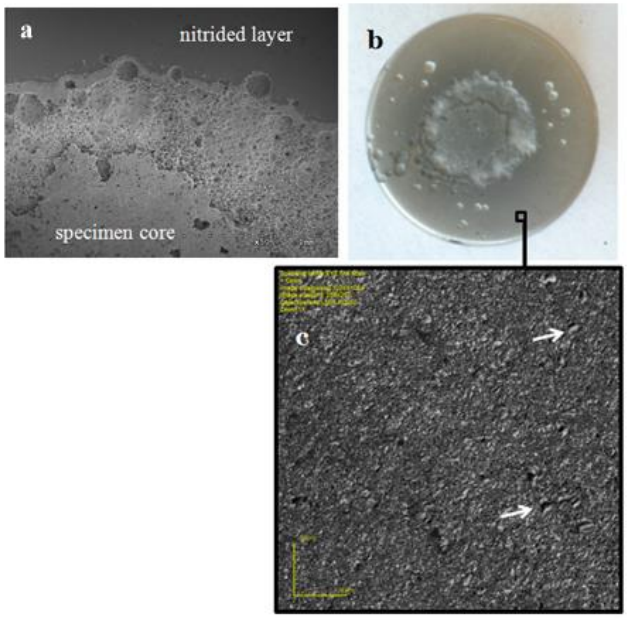

Fig. 8. Corroded surface morphology of plasma nitrided in 35:65 H_2:N_2 working gas mixture 440B steel; a – SEM photograph, magnification 50×; b – macro photograph; c – confocal microscope photograph in 1080× magnification, arrows – transition phase particles

Uneven nitrided layer adversely affects discussed steel corrosion resistance in chemically aggressive environment. The pres-

ence of varying in chemical composition areas leads to selective dissolution of the material, resulting in extensive damages at the edge-core interface (Fig. 8). The tightly covered with external layer area assumes the role of the cathode, while the specimen core – material that was to be protected – becomes the progressively dissolved anode. What is important, in these circumstances the original surface finish – sandblast or polishing - becomes insignificant when considering its influence on corrosion processes dynamics. Therefore, a predominant influence on corrosion processes has the modified layer extent.

4. SUMMARY

The aim of conducted study was to evaluate corrosion resistance of 440B type martensitic stainless steel after conventional heat treatment and plasma nitriding. The obtained findings analysis enabled authors to draw following conclusions:

- Material tempered in 250 or 390°C is characterised by similar corrosion resistance. High temperature tempering is not recommended due to martensitic steel sensitisation to intergranular corrosion.
- The 440B stainless steel plasma nitriding applied in order to extend the surgical instruments life cycle does not significantly affect its corrosion resistance as far as the uniform nitride layer over the entire detail surface is obtained.
- The nitrided layer heterogeneity results in intensification of corrosion processes, making the material even more susceptible to corrosion than after conventional heat treatment, and contributing to severe, visible even with the unaided eye damages development.

REFERENCES

1. **Baszkiewicz J., Kamiński F.** (2006), *Materials corrosion,* Publishing Office of Warsaw University of Technology, Warszawa.
2. **Bell T., Sun Y.** (2002), Low temperature plasma nitriding and carburising of austenitic stainless steels, *Advanced Materials And Processes,* Vol. 160, No. 6, 49-51.
3. **Głowacka M.** (1996), *Metallography,* Publishers of Gdansk Technical University, Gdansk.
4. **Gösta W.** (1985), *Base of corrosion and metals protection*, WNT, Warszawa.
5. **Grubb J. F.** (2011), *Martensitic stainless steels* in *Uhlig's Corrosion Handbook* (by Revie R. W.) , John Wiley and Sons, Hoboken.
6. **Hedström P.** (2007), *Deformation and Martensitic Phase Transformation in Stainless Steels,* Lulea University of Technology, Lulea.
7. **Li C. X, Bell T.** (2006), Corrosion properties of plasma nitrided AISI 410 martensitic stainless steel in 3.5% NaCl and 1% HCl aqueous solutions, *Corrosion Science,* Vol. 48, No. 8, 2035-2049.
8. **Marciniak J.** (1992), *Biomaterials in bone surgery,* Publishers of Silesian University of Technology, Gliwice.
9. **Mingolo N., Tschiptschin A. P., Pinedo C. E.** (2006), On the formation of expanded austenite during plasma nitriding of an AISI 316L austenitic stainless steel, *Surface and Coatings Technology,* Vol. 201, No. 7, 4215-4218.
10. **Paszenda Z., Tyrlik-Held, J.** (2003), *Surgical instrument,* Publishers of Silesian University of Technology, Gliwice.
11. **Pinedo C. E., Monteiro W. A.** (2004), On the kinetics of plasma nitriding a martensitic stainless steel type AISI 420, *Surface and Coatings Technology,* Vol. 179, No. 2-3, 119-123.
12. **Rudnik S.** (2006), *Metallography,* PWN, Warszawa.
13. **Samandi M., Shedden B. A., Smith D. I., Collins G. A., Hutchings R., Tendys J.** (1993), Microstructure, corrosion and tribological behaviour of plasma immersion ion-implanted austenitic stainless steel,*Surface and Coatings Technology,* Vol. 59, No. 1-3, 261-266.
14. **Tuckart W., Forlerer E., Iurman L.** (2007), Delayed cracking in plasma nitriding of AISI 420 stainless steel, *Surface & Coatings Technology,* Vol. 202, No. 1, 199-202.
15. **Wu K., Liu G. Q., Wang L., Xu B. F.**(2010) Research on new rapid and deep plasma nitriding techniques of AISI 420 martensitic stainless steel, *Vacuum,* Vol. 84, No.6, 870-875.
16. **Xi Y., Liu D., Han D.** (2008a), Improvement of corrosion and wear resistances of AISI 420 martensitic stainless steel using plasma nitriding at low temperature, *Surface & Coatings Technology,* Vol. 202, No. 12, 2577–2583.
17. **Xi Y., Liu D., Han D.** (2008b) Improvement of erosion and erosion–corrosion resistance of AISI420 stainless steel by low temperature plasma nitriding, *Applied Surface Science,* Vol. 254, No. 18, 5953–5958.
18. **Yang S., Wang Z. J., Kokawa H., Yutaka S. S.** (2007). Grain boundary engineering of 304 austenitic stainless steel by laser surface melting and annealing, *Journal of Materials Science,* Vol. 42, No. 3, 847-853.
19. **PN-EN ISO 7153-1:2002** Surgical instruments. Metallic materials. Stainless steel.
20. **PN-EN ISO 8044:2002** Corrosion of metals and alloys - Basic terms and definitions.
21. **PN-EN 10088-1:2005** Stainless steels. List of stainless steels.

Acknowledgement: This scientific work was supported by the Faculty of Mechanical Engineering, Bialystok University of Technology, project No S/WM/1/2009.

IDENTIFICATION OF LAYERS DISTRIBUTION IN THE COMPOSITE COUPON USING FINITE ELEMENT METHOD AND THREE POINT BENDING TEST

Łukasz MAZURKIEWICZ*, Jerzy MAŁACHOWSKI*, Krzysztof DAMAZIAK*, Paweł BARANOWSKI*, Paweł GOTOWICKI*

*Department of Mechanics and Applied Computer Science, Faculty of Mechanical Engineering,
Military University of Technology, ul. Kaliskiego 2, 00-908 Warszawa, Poland

lmazurkiewicz@wat.edu.pl, jerzy.malachowski@wat.edu.pl, kdamaziak@wat.edu.pl, pbaranowski@wat.edu.pl, pgotowicki@wat.edu.pl

Abstract: The main objective of the study is to develop experimentally validated FE model and perform numerical analysis of layered composites made by hand lay-up techniques during tension and bending test. The research object is glass - polyester laminate made of four unidirectional layers. In order to validate the numerical models experimental test were performed. Due to the very different stiffness modulus in tension and bending loading the material properties obtained from standard test are not suitable to apply in numerical model. Significantly different behaviour compared to experimental test was obtained for tree point bending where the numerical model becomes too stiff. Simple coupons, relatively easy to manufacture presented in the paper have very low quality. The differences in actual and theoretical bending stiffness (obtained from tension stiffness) exceed 70%. In order to represent the actual structure the layers of the composite were divided by resin layers and also additional resin layer at the top and bottom of the model were defined. Single stage optimization process was used to adjust the material layout. After layer set-up modification very significant improvement can be seen for flexural behaviour.

Key words: Fibre Reinforced Composite, FE Analysis, Hand Lay-Up Technique, Experimental Validation

1. INTRODUCTION

Composite materials, particularly fibre reinforced laminates, due to many advantages, are used as structural materials in many industries. They are characterized by high relative strength, high relative stiffness, weather resistance and quite low costs of production. However due to complex structure of such materials modelling of such structures is very difficult (Gama et al., 2011; Xiao et al. 2007; Mazurkiewicz et al., 2013).

The main objective of this study is to develop experimentally validated FE model and perform numerical analysis of layered composites made by hand lay-up techniques during tension and bending test. It has to be pointed out that those techniques are still the most popular method of composites elements production. On the other hand the hand lay-up composites are very sensitive to manufacture quality which is human factor dependent.

In the literature many authors discuss the problem of composite flexural stiffness. In the paper (Dong et al., 2013) authors presents study on the flexural behaviour of hybrid composites reinforced by S-2 glass and T700S carbon fibres, where different layout set-ups are tested in 3-point bending. The flexural strength is improved using numerical optimization. The good agreement of flexural moduli form FE analysis and experiments is a result of high-quality samples used in research. It also can be seen that the flexural modulus obtained experimentally is usually slightly lower than obtained from FE. In another publication (Nunes et al., 2012) a flexural behaviour of composite disc was studied. This time the difference between experimental and simulated values of the flexural stiffness was up to 13%. Also in (Khalid et al., 2005) where the glass/epoxy I-beams where subjected to three and four point bending, following dissimilarity can be seen between experimentally and numerically obtained flexural stiffness.

Our paper is focused on the problem of manufacture quality influence on decrease of structure bending stiffness and development of FE model with adequate flexural stiffness.

2. RESEARCH OBJECT

The research object is the glass fibre reinforced composite made of four unidirectional layers $[90]_4$. E-glass fabrics produced by Owens Corning Co., USA were used as reinforcement, i.e. D-610 (Weft 90°, uniaxial fabric, 607 g/m^2 – fibre set 595 g/m^2 and transverse stitching 12 g/m^2). The matrix constitutes Polimal 104 N-1 P/p-503 polyester resin, i.e. elasticized and incombustible Polimal 104 resin produced by Organika-Sarzyna Co., Poland.

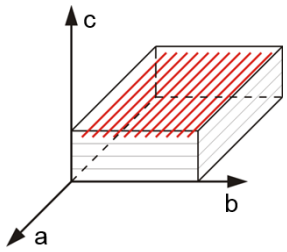

Fig. 1. Layer set-up of glass – polyester composite

3. STUDIED CASES

Two load cases were considered – tension and bending tests. The bending test is necessary to prepare more adequate multilayered plate model. The dimensions of the specimen used in those test and loading directions were presented in Fig. 2 and 3.

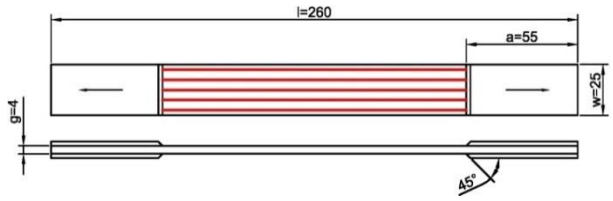

Fig. 2. Nominal dimensions of specimens and defined load for tension tests

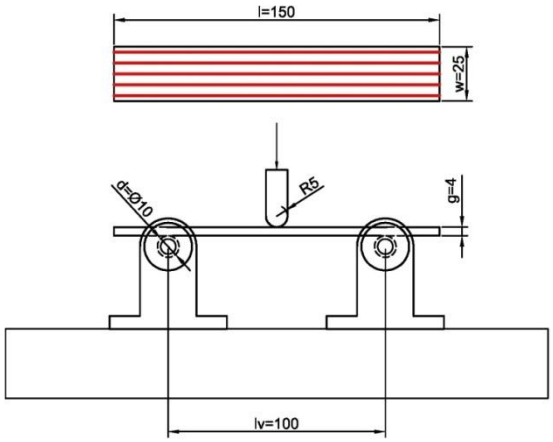

Fig. 3. Nominal dimensions of specimens and defined load for three point bending tests

4. EXPERIMENTAL TESTS

4.1. Properties identification

The material properties of FRC composite (Tab. 1) was obtained from the following experimental tests:

- tension test in fibre direction;
- tension test in cross-fibre direction;
- compression test in fibre direction;
- compression test in cross-fibre direction;
- shear test in plane *"ab"*;
- shear test in plane *"ba"*;
- shear test in plane "*cb*";

It should be mentioned that hand lay-up made composite can have relatively high thickness changes over the element, which can introduce additional error in stiffness parameters.

Tab. 1. Results of experimental test of FRC

E_{aa}^t [GPa]	E_{bb}^t [GPa]	E_{aa}^c [GPa]	E_{bb}^c [GPa]
21.7	6.05	22.4	7.48
ν_{ab} [-]	ν_{ba} [-]	ν_{bc} [-]	G_{ab} [GPa]
0.19	0.099	0.40	3.20
G_{ba} [GPa]	G_{cb} [GPa]	R_{aa}^t [MPa]	R_{bb}^t [MPa]
2.24	1.67	402	34.4
R_{aa}^c [MPa]	R_{bb}^c [MPa]	S_{ab} [MPa]	S_{ba} [MPa]
375	110	45.8	47.7
S_{ca} [MPa]	e_{aa}^t [-]		
33.7	0.02		

Data provided by M. Klasztorny, P. Gotowicki, D. Nycz, Military University of Technology, Department of Mechanics and Applied Computer Science

where: E_{aa}^t, E_{bb}^t, E_{aa}^c, E_{bb}^c – Young modulus in direction "*a*" or "*b*" for tension (***t***) and compression (***c***); ν_{ab}, ν_{ba}, ν_{bc} – Poisson ratio in plane *ab*, *ba* and *bc*; G_{ab}, G_{ba}, G_{cb} – shear modulus in plane "*ab*", "*ba*" and "*cb*"; R_{aa}^t, R_{bb}^t, R_{aa}^c, R_{bb}^c – tensile (***t***) and compressive (***c***) strength in direction "*a*" and "*b*"; S_{ab}, S_{ba}, S_{ca} – shear strength in plane *"ab"*, *"ba"* and *"ca"*, e_{aa}^t – tensile failure strain in direction *"a"*.

Additionally the material properties of matrix resin Polimal 104 N-1 (Tab. 2) were obtained from experimental tests:

- tension test;
- compression;
- shear test;

Tab. 2. Results of experimental test of polyester resin

E^t [GPa]	E^c [GPa]	ν [-]	G [GPa]
3.21	3.31	0.17	1.58
R^t [MPa]	R^c [MPa]	S [MPa]	e^t [-]
60.6	189	46.9	0.026
e^c [-]			
0.39			

Data provided by M. Klasztorny, P. Gotowicki, D. Nycz, Military University of Technology, Department of Mechanics and Applied Computer Science

where: E^t, E^c – Young modulus for tension *(**t**)* and compression *(**c**)*; ν – Poisson ratio; G – shear modulus; R^t, R^c – tensile *(**t**)* and compressive *(**c**)* strength; S – shear strength; e^t, e^c – tensile *(**t**)* and compressive *(**c**)* failure strain.

4.2. Validation tests

In order to validate the numerical models two experimental test tension and three point bending (Fig. 4) were taken into consideration. As authors stated before, bending test is necessary to prepare more adequate multi-layered plate model. Due to available equipment the three point bending test was performed, which is commonly used in flexural stiffness investigations (Dong et al., 2013).

In further research authors are planning to compare the presented results with those obtained from four point bending test which eliminates the shear influence and guarantees pure flexure mode. Such comparison of both test methods is presented in Khashaba et al., (2006) where better performance of 4-point bending tests is highlighted. It is also pointed out that in case of 3-point bending, the load concentration causes early micro cracking of the matrix as well as catastrophic failure. According to the authors, failure under bending is mainly caused by excessive delamination in the compression side of the specimen. However, in our experimental test this effect didn't appear and the failure was caused by damage in tension side.

Static experimental tests were performed on an INSTRON 8802 testing machine, with pressure force and punch displacement under registration (kinematic excitation at 2 mm/min velocity).

The validation tests revealed that the tensile and flexural stiffness moduli are very different from each other. In fact, this phenomenon is the main aim of the study.

Fig. 4. Tension and bending experimental tests set-ups respectively

5. PRELIMINARY ANALYSES

5.1. Discrete models

The discrete models were developed using Belytschko-Tsay shell elements (Fig. 5-6). The number of integration points through thickness was determined by a number of defined layers.

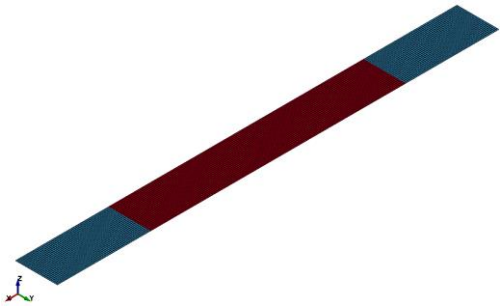

Fig. 5 Discrete models of FRC composite for tension test

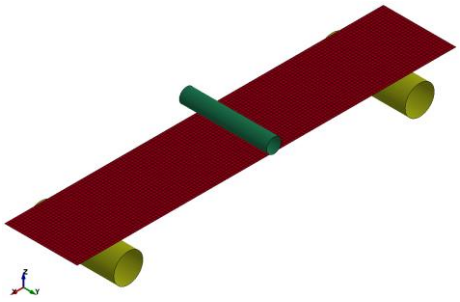

Fig. 6. Discrete models of FRC composite for bending test

Mesh sensitivity studies were performed with element sizes from 0.1 to 5 mm. As a result the simulation with element size of 1 mm revealed the best proportion between computational time and accuracy.

The models contain 1690 and 845 shell elements respectively for tension and bending tests. Additionally 9600 rigid shell elements were used to very accurately describe the rollers and the loading head and consequently to avoid unwanted contact problems.

The prescribed motion enforcement was applied to simulate the load. Selected nodes (corresponding to the place where crosshead was clamped and whole loading head part respectively in tension and bending test) were linearly displaced to final location. For the second load case (bending) the contact algorithm with penalty function was used. The contact stiffness is based on a minimum of master segment and slave node stiffness. The thickness of the shell elements is also considered in contact algorithm.

To reduce the computational time only the quarter of the models were analysed with symmetry boundary conditions applied.

5.2. Material model

From the number of composite materials models available in the LS-Dyna software, material model called Enhanced Composite Damage with failure criteria developed by Chang and Chang was chosen to describe the layered composite. This material model is specially designated to model failure mechanisms observed in composite materials. Besides usual static orthotropic properties, the various types of failure can be specified (LS-Dyna Keyword Manual):

– for the tensile fibre mode

$$\sigma_{aa} > 0 \;\; then \;\; e_f^2 = \left(\frac{\sigma_{aa}}{X_t}\right)^2 + \beta\left(\frac{\sigma_{ab}}{S_c}\right)^2 - 1 \begin{cases} \geq 0 & failed \\ < 0 & elastic \end{cases} \qquad (1)$$
$$E_a = E_b = G_{ab} = \nu_{ba} = \nu_{ab} = 0$$

– for the compressive fibre mode

$$\sigma_{aa} < 0 \;\; then \;\; e_c^2 = \left(\frac{\sigma_{aa}}{X_c}\right)^2 - 1 \begin{cases} \geq 0 & failed \\ < 0 & elastic \end{cases} \qquad (2)$$
$$E_a = \nu_{ba} = \nu_{ab} = 0$$

– for the tensile matrix mode

$$\sigma_{bb} > 0 \;\; then \;\; e_m^2 = \left(\frac{\sigma_{bb}}{Y_t}\right)^2 + \left(\frac{\sigma_{ab}}{S_c}\right) - 1 \begin{cases} \geq 0 & failed \\ < 0 & elastic \end{cases} \qquad (3)$$
$$E_b = \nu_{ba} = 0 \rightarrow G_{ab} = 0$$

– for the compressive matrix mode

$$\sigma_{bb} < 0 \;\; then \;\; e_d^2 = \left(\frac{\sigma_{bb}}{2S_c}\right)^2 + \left[\left(\frac{Y_c}{2S_c}\right)^2 - 1\right]\frac{\sigma_{bb}}{Y_c} - 1 \begin{cases} \geq 0 & failed \\ < 0 & elastic \end{cases} \qquad (4)$$
$$E_b = \nu_{ba} = \nu_{ab} = 0 \rightarrow G_{ab} = 0$$
$$X_c = 2Y_c \;\; for\, 50\%\; fiber\, volume$$

In the implemented constitutive model an erosion can occurs when:

– the tensile fibre strain is greater than ε_{max}^{+} or smaller than ε_{max},
– the effective strain is greater than ε_{fs}.

This means that, when a failure occurs in all of the composite layers (through-thickness integration points), the element is deleted.

In the preliminary analyses numerical models had four unidirectional composite layers with the properties defined based on experimental identification tests (Tab 1). Layers were uniformly distributed over the thickness and symmetrical with respect to neutral plane. Due to a small difference between compression (E_{aa}^{c}) and tension (E_{aa}^{t}) moduli (Tab. 1) average value was implemented in the numerical model. Authors assumed that application of model with separate stiffness properties for tension and compression would bring an insignificant improvement in obtained results for this particular composite material. Nevertheless for materials with higher differences between tension and compression modulus this approach should be used.

5.3. Numerical solution

The LS-Dyna software was used in our studies. Incremental static analysis was performed using full Newton-Rapshon algorithm. Equation solved in this stage had the following form (Hallquist, 2006):

$$K_i \Delta x_{i-1} = \Delta Q_i \tag{5}$$

where: K_i – stiffness matrix, Δx_{i-1} – displacement vector, ΔQ_i – external force vector.

The residual displacement and energy criteria were used to control the solution:

$$\frac{|\Delta u_i|}{u_{max}} < \varepsilon_d \quad \text{and} \quad \frac{|\Delta u_i Q_i|}{|\Delta u_0 Q_0|} < \varepsilon_e \tag{6}$$

where: Δu_i – increment in displacement in current step, u_{max} – maximum displacement, Δu_0 – desired increment in displacement, Q_0 – desired load, Q_i – load in current step.

5.4. Preliminary analysis results

The results of preliminary tests indicated that the model with four unidirectional layers defined and material properties obtained from standard tests behave correctly in tension test (Fig. 7).

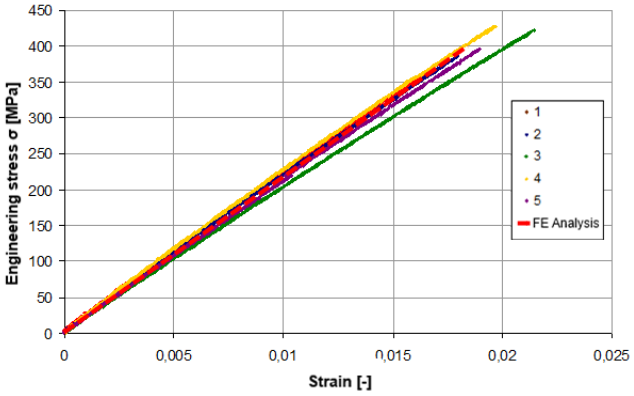

Fig. 7. Experimental (1-5) and numerical curves of engineering stress versus strain during tension test

Significantly different behaviour comparing to experimental tests results was obtained for three point bending tests, where the numerical model becomes too stiff (Fig. 8). The last point in FE analysis with a sudden decrease of a force indicates the numerical process of coupon failure occured.

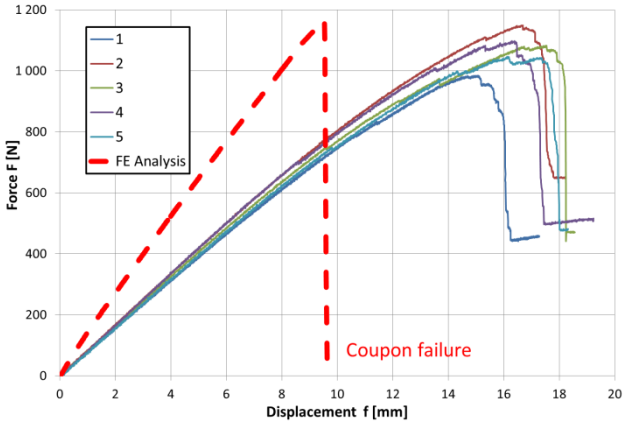

Fig. 8. Experimental (1-5) and numerical curves of force versus displacement during three point bending

6. LAYERS LAYOUT MODIFICATION

6.1. Method used

Due to the very different stiffness modulus in tension and bending loading the material properties obtained from standard test are not suitable to apply in numerical model. Authors assume that this is the result of the hand lay-up production and non-uniformly distributed layers of composite through thickness. Therefore a modified representation of composite structure is proposed. The reverse approach to a homogenisation was performed (Boczkowska et al., 2000). The layers of the composite were divided by resin layers and also an additional resin layers at the top and bottom of the model were defined. Resultant thickness of a the composite coupon remains unchanged.

The models were developed based on two parameters:

– composite volume fraction

$$V = \frac{n \cdot g_c}{g_{res}} \tag{7}$$

– external matrix volume fraction

$$V_z = \frac{2 \cdot g_e}{g_{res}\,(1-V)} \tag{8}$$

where: g_c – actual composite layer thickness, g_i – internal matrix layers thickness, g_e – external matrix layers thickness, g_{res} – resultant composite thickness, n – number of composite layers

The resultant layer set-up is presented in Fig. 9.

The material properties for matrix layers were defined based on resin experimental test, but to simplify the model linear elastic material was used. Therefore, to represent the actual matrix behaviour the reduced Young modulus equals to $E_m = R^t/e^t$ was used.

Reversing the simple plain stress homogenisation theory for laminar materials, the stiffness and strength properties for composite layers were obtained according to (Boczkowska et al., 2000):

$$E_{res} = E_c V + E_m(1-V) \rightarrow E_c = \frac{E_{res} - E_m(1-V)}{V} \quad (9)$$

where: E_{res} – resultant stiffness modulus (obtained from experiments), E_m – matrix layer stiffness modulus (obtained from experiments), E_c – composite layer stiffness modulus, V – composites volume fraction.

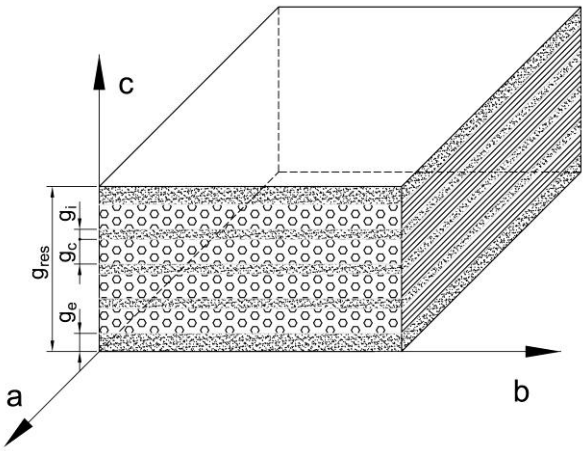

Fig. 9. Layers layout after model modification

6.2. Layout optimization

To explore the sensitivity of the model and to find the correct layer layout the model was submitted to a single stage optimization process (Stander et al., 2009). The LS-Opt software was used to run the optimization process for bending test. The following analysis parameters were defined:

variables:
- composite volume fraction $V = (0.3 \div 0.99)$
- external matrix volume fraction $V_Z = (0.4 \div 0.99)$

dependent variables:
- stiffness parameters,
- strength parameters,
- density,
- layers thickness

objectives:
- stiffness error $\Delta S = |S_{num} - S_{exp}|/S_{num}$ where $S = |F_{max}/f_{max}|$
- force error $\Delta F = |F_{num} - F_{exp}|/F_{num}$
- displacement error $\Delta f = |f_{num} - f_{exp}|/f_{num}$

constrains:
- resultant thickness g_{res}

The procedure was performed for 16 sampling points and the genetic algorithm implemented in LS-Opt software where used for optimization.

Optimized layer obtained from this procedure consist of following layers:
- layer 1 – polyester resin – $g_e = 0.7218$ mm
- layer 2 – composite – $g_c = 0.396$ mm
- layer 3 – polyester resin – $g_i = 0.3168$ mm
- layer 4 – composite – $g_c = 0.396$ mm
- layer 5 – polyester resin – $g_i = 0.3168$ mm
- layer 6 – composite – $g_c = 0.396$ mm
- layer 7 – polyester resin – $g_i = 0.3168$ mm
- layer 8 – composite – $g_c = 0.396$ mm
- layer 9 – polyester resin – $g_e = 0.7218$ mm

6.3. Results

The resultant model with layout obtained from optimization process was submitted to numerical tension and bending tests. Results for the tension test are the same as the one from preliminary results due to equivalent resultant Young modulus and strength parameters.

However, a significant improvement can be seen for flexural behaviour (Fig. 10). The model stiffness is nearly identical with the coupon stiffness. Also, the maximum force is comparable to the experimental one. The difference in stiffness and maximum force can be caused by a simplified linear elastic model of matrix, numerical representation of damage process and element erosion.

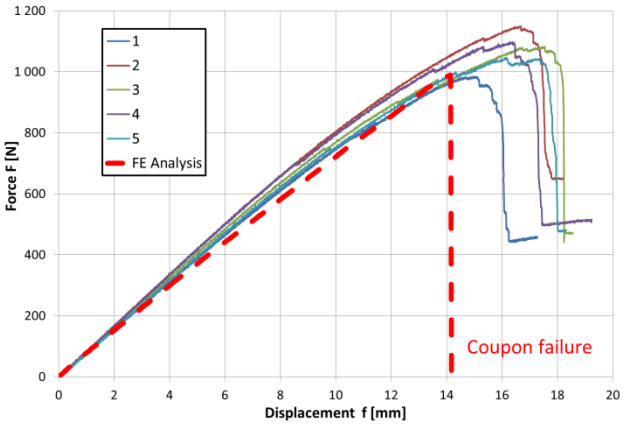

Fig. 10. Experimental (1-5) and numerical curves of force versus displacement during three point bending – modified numerical model with optimized layer layout

7. SUMMARY

The industrially made composite elements using hand lay-up techniques have very non-uniformly distributed layers. Presented in the paper simple rectangular coupons, which are relatively easy to manufacture, have very low quality. In effect the differences in actual and theoretical bending stiffness (obtained from tension stiffness) exceed 70%.

Results presented in this paper clearly show that the tensile test is not enough to validate the developed discrete model. To obtain the proper flexural stiffness the validation in tensile and bending test is required.

The method of fibre reinforcement composite FE model validation which takes the advantage of numerical optimization procedure of layers distribution adjustment is proposed. This method can be efficient way for composite model development where the structure layout is dependent on coupons quality.

The presented method can be extended to be applicable for the materials with large dissimilarities in tensional and compressive modulus by adopting a constitutive model with separate tension and compression stiffness parameters.

REFERENCES

1. **Boczkowka A., Kapuściński J., Puciłowski K, Wojciechowski S.,** (2000), *Composities*, Warszawa (in Polish).

2. **Dong C., Davies I.J.,** (2012), Optimal design for the flexural behaviour of glass and carbon fibre reinforced polymer hybrid composites, *Materials and Design,* 37, 450–457
3. **Gama B.A., Gillespie Jr J.W.,** (2011), Finite element modeling of impast, damage evolution and penetration of thick-section composites, *International Journal of Impact Engineering*, 38, 181-197.
4. **Hallquist J.O.,** (2006), LS-Dyna Theory manual, Livermore Software Technology Corporation (LSTC).
5. **Khalid Y. A., Ali F. A., Sahari B.B., Saad** (2005), Performance of composite I-beams under axial compression and bending load modes, *Materials and Design*, 26, 127–135.
6. **Khashaba U.A., Seif M.A.,** (2006), Effect of different loading conditions on the mechanical behaviour of [0/±45/90]s woven composites, *Composite Structures*, 74, 440–44.
7. **LS-Dyna Keyword User's Manual Volume I**, (2012) February 14, (revision: 1197), Version 971, Livermore Software Technology Corporation (LSTC).
8. **Mazurkiewicz L., Damaziak K., Malachowski J., Baranowski P.**, (2013), Parametric study of numerically modelled delamination proces in a copmposite structure subjected to dynamic loading, *Engineering Transactions*, 61 (1), 15-31.
9. **Nunes J.P., Pouzada A.S., Bernardo C.A.,** (2002), The use of a three-point support flexural test to predict the stiffness of anisotropic composite plates in bending, *Polymer Testing,* 21, 27–33.
10. **Stander N., Roux W, Goel T., Eggleston T., Craig K.,** (2009) *LS-OPT User's Manual*, Livermore Software Technology Corporation (LSTC).
11. **Xiao J. R., Gamma B.A., Gillespie Jr J.W.,** (2007), Progressive damage and delamination in plain weave S-2 glass/SC-15 composites under quasi-static punch-shear loading, *Composite Structures*, 78, 182–196.

The research was carried out under a research grant from Polish Ministry of Science and Higher Education no. 0097/R/T00/2010/12. This support is gratefully acknowledged.

DEPENDENCE OF CREEP FAILURE PROBABILITY ON THE SIZE OF METALLIC SPECIMENS

Krzysztof NOWAK*

*Faculty of Civil Engineering, Strength of Material Department, Cracow University of Technology, ul. Warszawska 24, 31-155 Kraków

kn@limba.wil.pk.edu.pl

Abstract: The occurrence of statistical size effect is considered for damage in creep conditions. The numerical and experimental analysis have been performed. The obtained results are ambiguous. Numerical models confirm the scale effect which can be statistical or deterministic one. But this effect has no experimental verification. It may suggest that the weakest link model cannot be applied in creep conditions. Explanation of this needs further investigations.

Key words: Size Effect, Creep Damage, Cellular Automata

1. INTRODUCTION

As is well-known, the specimen or structural element size influences the value of fatigue strength (Kocańda and Szala, 1991). When the size of element is larger the strength of specimen is lower. This phenomenon, known as size effect, can be described by probabilistic Weibull model (1939). The damage in creep conditions has many common aspects to fatigue failure. So it can be expected that creep strength dependence upon the specimen size is similar. But there are not so much papers describing size effect or lack of it for creep (e.g. Yatomi et al., 2003) so, evidence of this is not obvious.

2. THE STATISTICAL AND DETERMINISTIC SIZE EFFECT

The size effect described by Weibull is called statistical, as its nature is connected with statistical dispersion of material properties. This effect can be modelled by the so-called weakest link model (see Fig. 1). It assumes that specimen is made of many chains of random strength. The chains are linked in series, and therefore the strength of the whole specimen is determined by the weakest link. The longer specimen is, the probability of lower strength is larger.

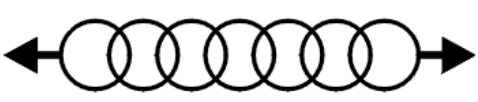

Fig. 1. The weakest link model

Any characteristic dimensions do not occur in the statistical size effect. It is caused mainly by nonhomogeneity of material or variability of specimen cross-section. The serial connections of chains correspond to situation when occurrence of first defect in specimen cause all the specimen to failure. In case of fatigue it is often related to existence of microcracks or microdefects, where the fatigue failure can arise. For larger specimen the probability of existence of critical defect is larger and the failure can occur at lower number of cycles (Carpinteri et al, 2002, 2004, 2009, 2010).

In statistical size effect the power law is used for description of dependence of element size:

$$\mathrm{f}(D) = c_0 D^s \tag{1}$$

where f(D) is a function describing examined parameter (e.g. strength), D is the structural element size, and c_0, s are material constants. The power law is the only one, which allows us to describe size dependency without any characteristic length (Bažant, 1999).

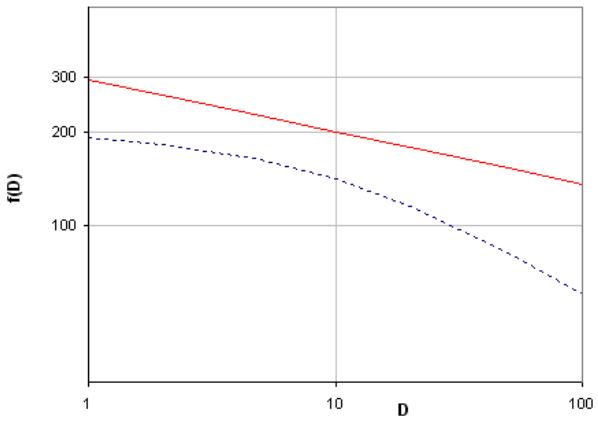

Fig. 2. Comparison of statistical and deterministic size effects. Solid red line - statistical size effect, eq. (1) for s=-1/6, dashed blue line - deterministic size effect, eq. (2)

In contradiction to statistical size effect the characteristic length can occur in deterministic size effect. In this case not only statistical dispersion, but also relation of specimen size to some characteristic material dimension, is responsible for size effect. It makes the size effect more deterministic. This phenomenon is well described for materials with large inhomogeneities like

concrete, rocks. Exemplary law for such effect can be stated in form of equation (Bažant, 1984):

$$\mathrm{f}(D) = f_0\left(1+\frac{D}{D_0}\right)^{-1/2} \tag{2}$$

where D_0 is characteristic dimension and f_0 material constant. Comparison of statistical and deterministic size effect laws is shown in Fig. 2.

It can be shown for the weakest link model that the mean value of nominal strength is (Bažant, 1999):

$$\bar{\sigma} = s_0\Gamma\left(1+m^{-1}\right)\left(\frac{V_0}{V}\right)^{1/m} \tag{3}$$

and the coefficient of variation:

$$v = \sqrt{\frac{\Gamma\left(1+2m^{-1}\right)}{\Gamma\left(1+m^{-1}\right)}-1} \tag{4}$$

where m is the Weibull modulus, s_0 is a material parameter, V is the examined volume of material, V_0 is the volume of the smallest possible test specimen, Γ - is the gamma function. In equation (4) the value of the coefficient of variation depends only on modulus m, so it is often used to determine this parameter. It usually varies from 5 to 50. The small value of m gives strong dependency upon the specimen dimensions and also large value of coefficient of variation. When the scatter, represented by coefficient of variation, of any variable is known it is possible to estimate the sensitivity of this variable to size effect. Not always the value of the modulus m determined from equation (4) corresponds to the mean value determined from equation (3). It means that the deterministic size effect exists, what is characteristic for concrete or other quasi-brittle materials (Bažant, 1999).

3. RANDOMNESS OF CREEP FAILURE

The phenomenon of creep is characterised by large randomness. It causes that the scatter of basic parameters describing creep failure (time to failure, strain at failure) is significant. It is caused mainly by not identical conditions of creep tests (variations of temperature, eccentricity, see Hayhurst, 1974). But even ensuring special accuracy in test performance, the scatter of results is significant (e.g. Farris et al., 1990, obtained scatter of times to failure in test of copper with coefficient of variation about 60%). This variability of the results can be explained by nonhomonegeity of material connected with its microstructure.

Estimation of Weiibull modulus from equation (4) by fitting to coefficient of variation equal to 60% gives m=1.7. This value defines very strong dependency on specimen size, e.g. two times larger specimen should give reduction of creep resistance of about 33%. Existing experimental data shows that there is no size effect for creep of metallic materials or it is very small. E.g. Yatomi et al. (2003) made comparison of creep crack growth for welds of sizes: 15, 25 and 50 mm and claimed no size effect.

4. TIN WIRE EXPERIMENTS

The creep experiments are very time consuming. Therefore there is not much data allowing to draw conclusions about probabilistic behaviour of material, i.e. the nature of scale effect. This is the reason why own experiments were performed for wire made of tin alloy Sn60Pb40, which has small melting temperature (460 K) and creeps in room temperature. The specimens have 1mm of diameter and were loaded by constant force giving nominal stress 11.8 MPa. Two lengths of specimens were examined: short - 54 mm, and long - 93 mm. The obtained times to failure are shown in Table 1.

Tab. 1. Experimental results for tin alloy wire

length of specimen [mm]	number of probes	mean time to failure [s]	coefficient of variation
54	14	1617.3	15.6%
93	11	1777.3	20.8%

The observed in experiment scale effect is reverse to the expected one. The mean time to failure for longer specimens is about 10% greater than for shorter ones. The explanation of this phenomenon requires much more experiments to perform to exclude any accidental cause of this behaviour.

5. NUMERICAL ANALYSIS

5.1. FEM model

In order to numerically verify statistical size effect, series of simulations were performed by author. Rectangular specimen 5x2.5mm was modelled in plane strain state by the finite element method. ABAQUS code was used. Keeping constant mesh density the simulations were performed for lengths: 10, 20, 40, 80 and 160 mm. The specimen of 20 mm was chosen as a reference one. The material model was Hook-Norton-Kachanov (equations after Bodnar and Chrzanowski, 2002):

$$\varepsilon_{ij} = \varepsilon^e_{ij} + \varepsilon^c_{ij} \tag{5a}$$

$$\varepsilon^e_{ij} = D^{-1}_{ijkl}\sigma_{kl} \tag{5b}$$

$$\frac{\partial \varepsilon^c_{ij}}{\partial t} = B\left(\frac{\sigma_{eff}}{1-\omega}\right)^n \frac{\partial \sigma_{eff}}{\partial \sigma_{ij}} \tag{5c}$$

$$\frac{\partial \omega}{\partial t} = A\left(\sigma_{eq}\right)^{\mu} \tag{5d}$$

$$\sigma_{eq} = \alpha\frac{\sigma_{\max}}{1-\omega} + (1-\alpha)\frac{\sigma_{eff}}{1-\omega} \tag{5e}$$

where: $\varepsilon_{ij}, \varepsilon^e_{ij}, \varepsilon^c_{ij}$ – total, elastic and creep strain tensors, respectively, σ_{kl} - stress tensor, D_{ijkl} – elastic constants matrix, B, n, A, m, α – steady-state creep and damage material constants, σ_{max}, σ_{eff}, σ_{eq} – main positive principal stress, Huber-Mises effective stress and equivalent stress, respectively, ω – scalar damage parameter ($0<\omega<1$), t – time.

The material constants were fitted to data for copper in temperature 723K and mean grain diameter 30 microns obtained by Feltham and Meakin (1959): elastic constants – Young modulus 82.7GPa, Poisson ratio 0.33, creep constants – B=1.18MPa^{-n}s^{-1},

n=4.17 damage constants – A=5.04MPa$^{-\mu}$s^{-1}, μ=2.87, α=1. In order to ensure randomness of results, the random initial damage parameter was introduced. Its values were spread over a volume of specimen according to exponential distribution with expected value ω_0=0.006.

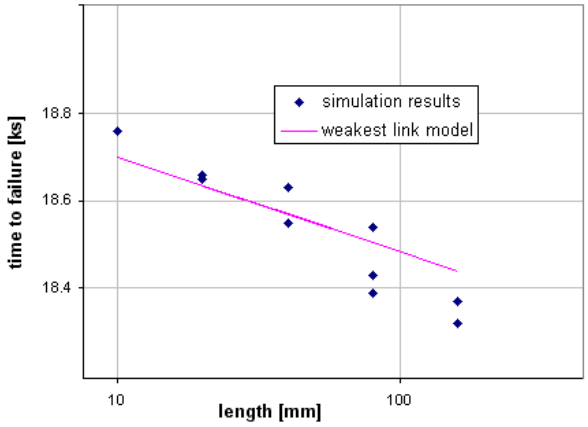

Fig. 3. Size dependency of time to failure obtained from numerical simulation in comparison with the weakest link model - eq. (6)

The scatter of creep test results in FEM model was obtained from 8 probes performed for reference size of specimen. Every probe had unique random configuration of initial damage parameter. For uniaxial tensile loading corresponding to equivalent stress σ_{eq}=34.6MPa, the obtained scatter was very small. The mean value of time to failure was 18635s and coefficient of variation was 0.65%. This coefficient corresponds to Weibull modulus m=196 according to equation (4). Despite the relation is very weak it is possible to compare the values resulting from the weakest link model with results of numerical simulations (see Fig. 3). According to the weakest link model and the Monkman-Grant relation (1956), the size dependency of time to failure can be calculated as follows:

$$t_f = t_{f0}\left(\frac{l_0}{l}\right)^{1/m} \tag{6}$$

where: l is length of specimen, l_0 is length of reference specimen, t_{f0} is value of time to failure for reference size. The correlation of simulation results with the model is quite good, although the size effect is very weak due to uniform material properties over the volume of specimen. The influence of characteristic size, which in this case is finite element size, is also very small. Therefore it can be stated that the numerical model confirms the statistical size effect.

5.2. Multiscale model

The second model analysed is the multiscale CAFE model (see Nowak, 2011). It allows to introduce nonhomogeneity of microstructure of material resulting in large scatter of simulation results. The model consists of two main parts describing deformation and damage. They operate on different scales and use different methods of analysis.

The deformation is modelled on macro level using discretised version of constitutive equation (7):

$$\dot{\varepsilon}_c = B_1 \varepsilon_c^{-2}\left(\frac{\sigma}{1-\omega}\right)^{n_1} \tag{7}$$

where n_1, B_1 are creep constants fitted to primary creep behaviour according to Chrzanowski's (1972) proposal of description of primary, secondary and tertiary creep.

The damage development processes is modelled by Cellular Automata (CA) technique (see Raabe, 2002, for review). It operates on microstructure of polycrystalline material using Representative Volume Element (RVE) approach. The CA model reflects the discrete nature of material. The state value of a single cell and its neighbourhood allows to distinguish if cell belongs to grain interior or grain boundary, it also allows to model voids or cracks. Also the randomness of creep process can be modelled by CA very easily by introduction the random microstructure and by random process of damage development. The algorithm uses in current simulation prefer development of intergranular cracks, as size effect is more significant in brittle failure. The relative length of longest crack inside the RVE is used as damage parameter ω in deformation equation (7). In turn the deformation obtained by FE model influences the current size of RVE. It results in mutual coupling of both scales.

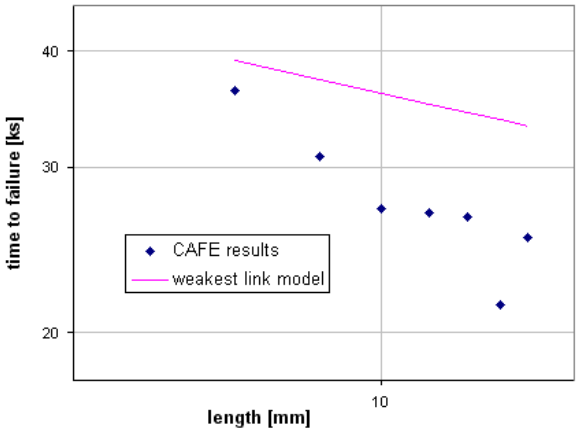

Fig. 4. Size dependency of time to failure obtained from CAFE simulation in comparison with the weakest link model

Similar to the previous case, the simulations were performed for specimen of 5 mm width and different lengths from 5 to 20mm, keeping constant the density of FE mesh and size of RVE (in cells). The material parameters were also fitted to results of experiment for copper by Feltham and Meakin (1959) but the loading in uniaxial tensile test was σ_{eq}=30.0MPa. The reference length was 5mm. The scatter of results was produced by different initial microstructure of grains of mean diameter about 100 cells, where RVE size was 320 cells. For 8 tests of reference length size the mean value of time to failure was 39100s with coefficient of variation equals to 14.1%. This scatter is comparable with scatter of experiments results (cf. Garofalo et al., 1961, and Tab. 1). According to equation (4) corresponding Weibull modulus is m=8.5. Comparison of the simulations results for different specimen length with values predicted by equation (3) gives much strongest relation with scale (see Fig. 4). This indicates that this size effect cannot be considered as only statistical one. Existence

of at least two characteristic dimensions like grain size and RVE size results in deterministic size effect. The effect is strong as they are quite close one to another.

6. CONCLUSIONS

It has been shown that the numerical simulations performed by the author can be used in the description of scale effect in creep tests.

The scatter of results obtained by means of multiscale model coincides with scatter of times to failure obtained from experiments. This scatter should cause statistical scale effect described by weakest link model. However, the results of own and also other experiments do not show such effect. The reason of that is not clear. The explanation of that phenomenon requires more experimental and numerical investigations.

REFERENCES

1. **Bažant Z.P.** (1984), Size Effect in Blunt Fracture: Concrete, Rock, Metal, *J. Eng. Mech*., 110, 518–535.
2. **Bažant Z.P.** (1999), Size effect on structural strength: a review, *Archive of Applied Mechanics*, 69, 703-725.
3. **Bodnar, A., Chrzanowski, M.** (2002), On creep rupture of rectangular plates, *ZAMM*, 82, 201-205.
4. **Carpinteri A., Spagnoli A.** (2004), A fractal analysis of size effect on fatigue crack growth, *Int. J. of Fatigue*, 26, 125–133.
5. **Carpinteri A., Spagnoli A., Vantadori S.** (2002), An approach to size effect in fatigue of metals using fractal theories, *Fatigue Fract. Engng. Mater. Struct.*, 25, 619-627.
6. **Carpinteri A., Spagnoli A., Vantadori S.** (2009), Size effect in S–N curves: A fractal approach to finite-life fatigue strength, *Int. J. of Fatigue*, 31, 927–933.
7. **Carpinteri A., Spagnoli A., Vantadori S.** (2010), A multifractal analysis of fatigue crack growth and its application to concrete, *Eng. Fract. Mech.*, 77, 974–984.
8. **Chrzanowski M.** (1972), On the Possibility of Describing the Complete Process of Metallic Creep, *Bull. Ac. Pol. Sc. Ser. Sc. Techn.*, XX, 75-81.
9. **Farris J.P., Lee J. D., Harlow D. G., Delph T.J.** (1990), On the scatter in creep rupture times, *Metallurgical and Materials Transactions*, 21A, 345-352.
10. **Feltham P., Meakin J.D.** (1959), Creep in Face-Centred Cubic Metals with Special Reference to Copper, *Acta Metallurgica*, 7, 614-627.
11. **Garofalo F., Whitmore R.W., Domis W.F., Gemmingen F.** (1961), Creep and creep-rupture relationships in an austenitic stainless steel, *Trans. Metall. Soc. AIME*, 221, 310-319.
12. **Hayhurst D.R**. (1974), The effects of test variables on scatter in high-temperature tensile creep-rupture data, *International Journal of Mechanical Sciences*, 16, 829-841.
13. **Kocańda S., Szala J.** (1991), Podstawy obliczeń zmęczeniowych, PWN, Warszawa (in Polish).
14. **Monkman F.C., Grant N.J.** (1956), An Empirical Relationship between Rupture Life and Minimum Creep Rate in Creep-Rupture Test, *Proc. ASTM*, 56, 593-620.
15. **Nowak K.** (2011), Uncertainty of lifetime for CAFE creep damage model, *Computer Methods in Materials Science*, 11, 315-323.
16. Raabe D. (2002), Cellular Automata in Materials Science with Particular Reference to Recrystallization Simulation, *Ann. Review of Materials Research,* 32, 53-76.
17. **Weibull W.** (1939), The Phenomenon of Rupture in Solids, *Proceedings of Royal Swedish Institute for Engineering Research*, 153, 5-55.
18. **Yatomi M., Nikbin K.M., O'Dowd N.P.** (2003), Creep crack growth prediction using a damage based approach, *International Journal of Pressure Vessels and Piping*, 80, 573-583.

THE ANALYSIS OF TRIBOLOGICAL PROCESSES IN THE INKING UNIT OF THE OFFSET PRINTING MACHINE

Yuriy PYRYEV [*], Zofia Maria PIĘTAK [*]

[*] Faculty of Production Engineering, Institute of Mechanics and Printing, Division of Graphic Art Technologies, Warsaw University of Technology, ul. Konwiktorska 2, 00-217 Warszawa, Poland

yu_pyryev@wp.pl, z.pietak@gmail.com

Abstract: In this paper is proposed the mathematical description of the temperature distribution resulting from the friction between the two inking rollers (one of which is made off steel and the second one has elastic layer) in the offset printing machine. So-called in printing industry steel vibrator roller perform simultaneously rotary and reciprocating motion. This reciprocating motion is the main source of the heat generation. Using the Laplace transform method for heat conduction equations with boundary conditions taking into account the real processes taking place in the inking unit in contact area we obtained and analyzed the solution that could be useful for determination and regulation of parameters in order to decrease time of process stabilization.

Key words: Printing, Friction, Inking Unit, Laplace Transform, Heat Distribution, Roller/Roller Contact

1. INTRODUCTION

During the printing process in the offset printing machine, temperature of the rollers in the inking unit and surrounding air increases gradually. This phenomena bases on the influence of the pressure between rotating rigid steel and rubber coated rollers and influence of the reciprocating motion along the roller pivot. The phenomena of temperature variations in the inking unit of the printing machines, particularly the offset printing machines which are characterised by a complex inking unit, is inevitable. Even in the machines, in which the inking units (more precisely selected inking rollers) are thermostatted, the fluctuations of the temperature are considerable (Chou et al., 1996). The main cause of temperature increase in the inking unit is the friction between the flexible and rigid axially oscillating rollers. Temperature variations affect the quality of prints. The temperature increase in the inking unit leads to:

- changes of the rheological ink properties (especially viscosity);
- the instability of emulsion of ink and dampening solution;
- the deposition of dust on a rubber blanket;
- increased demand for dampening solution.

This all negatively affects quality of prints. Therefore it seems to be important and reasonable to study this phenomena more carefuly and to built and solve the appriopriate mathematical model. Mathematical models describing the various processes in the mechanical frictional contact presented by Awrejcewicz et al. (2013), Olejnik et al. (2013), Talati et al. (2009), Yevtushenko et al. (2009, 2012) were studied in order to compare various approaches and choose the own path.

2. GEOMETRY AND ASSUMPTIONS OF MODEL

In the inking unit of the offset press the ink is transported from the ink fountain to the plate cylinder through a set of rotating and being in contact rigid and covered with flexible layer rollers. Particular importance for the warm-up phenomenon have steel vibrator rollers which simultaneously perform a rotary (frequency Ω) and reciprocating motion.

Due to the high real speed of rotating rollers (rigid vibrator roller is cooled by the liquid flowing inside the roller), the problem of the roller pair is simplified and reduced to the problem of the roller with liquid coolant inside $T_1^0(t) = \theta_1^0 h_1(t)$ and roller's surrounding, which on the border with the surrounding reaches the temperature ambient (surrounding) temperature $T_2^0(t) = \theta_2^0 h_2(t)$ (Pyryev et al., 2010). The generated heat is a result of friction on the contact surface between rollers. The heat flux acts on the border of the roller $R = R_0$ and surrounding (Fig. 1).

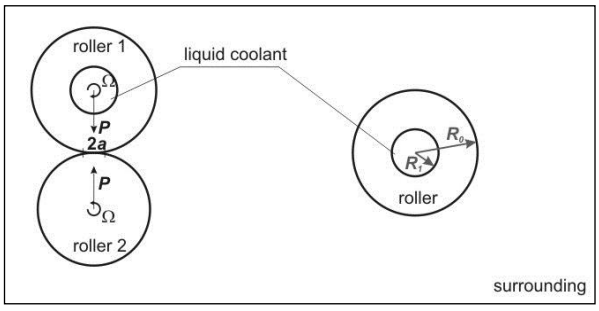

Fig. 1. The transition from the real issue to the model

In the case of axisymmetric state of roller temperature T_1 state the heat conduction equation for an isotropic body in cooperation with cylindrical coordinates (R, φ, z) given by Carslaw et. al (1959) will take the form as follows:

$$\frac{\partial^2 T_1(R,t)}{\partial R^2} + \frac{1}{R}\frac{\partial T_1(R,t)}{\partial R} = \frac{1}{k_1}\frac{\partial T_1(R,t)}{\partial t}, \quad R_1 < R < R_0 \qquad (1)$$

with following boundary conditions (after Awrejcewicz et al., 2009):

$$\lambda_1 \frac{\partial T_1(R_1,t)}{\partial R} - \alpha_1^T [T_1(R_1,t) - \theta_1^0 h_1(t)] = 0 \tag{2}$$

$$\lambda_1 \frac{\partial T_1(R_0,t)}{\partial R} + \alpha_2^T [T_1(R_1,t) - \theta_2^0 h_2(t)] = Q(t) \tag{3}$$

and initial conditions:

$$T_1(R,0) = 0\,,\ R_1 < R < R_0 \tag{4}$$

Above we have taken indications as follows: $T_1(R,t)$– temperature increase of the roller, t – time, $Q(t) = \theta_0^0 h_0(t)$ – power density of friction, k_1 – thermal diffusivity of a roller, α_n^T – heat transfer coefficient: $(n = 1)$ between the coolant and material which the roller is made of (forced water flow in the pipe), $(n = 2)$ between the surrounding (air) and material which the roller is made of (forced air flow near the surface of the roller), λ_1 – thermal conductivity of the roller, $h_n(t)$ – dimensionless internal $(n = 1)$ and external $(n = 2)$ temperature, $T_1^0(t) = \theta_1^0 h_1(t)$, $T_2^0(t) = \theta_2^0 h_2(t)$ – temperature increase of the coolant and sorrounding.

We assume that the reciprocating movement (and resulted from it friction) is the source of heat, and hence we assumed the formula of the friction power density:

$$Q(t) = (1-\eta_1)\eta_2\, f(V_r) V_r\ p_0 \tag{5}$$

where: p_0 – average contact pressure, associated with a contact force P by formula $p_0 = P/2a$, where contact area width $2a$ is found from Herz problem solution for two rollers (Jurkiewicz et al., 2011), V_r – relative velocity of being in contact rollers, $f(V_r)$ – kinematic friction coefficient, η_1 – coefficient responsible for the part of the power which is lost e.g. because of wear, η_2 – coefficient depending on time.

After Blok (1940) we assume that kinematic friction coefficient: $f(V_r) = f_0 sgn(V_r)$ and therefore we obtain:

$$Q(t) = (1-\eta_1)\eta_2\ f_0 |V_r|\, p_0 \tag{6}$$

The construction and operation of the inking unit (rotary and reciprocating motion of the roller) results that the relative movement of being in contact rollers along the axis changes periodically:

$$Z(t) = Z_0 \sin \omega t \tag{7}$$

where: – maximum relative displacement of the rollers, ω – frequency of relative displacement of rollers (from the construction of the inking unit $\omega = \Omega$).

The fact that the heat is generated by friction in changing contact area:

$$S(t) = 2a\left(L - |Z(t)|\right) \tag{8}$$

where: $S(t)$ – contact area between rollers, L – length of the roller,is included by entering the depending on the time coefficient η_2 into the formula (6) of the heat flux $Q(t)$:

$$\eta_2 = S(t)/S_1 \tag{9}$$

where: S_1 – area of the cylinder side $S_1 = 2\pi R_0 L$.

Hence the coefficient:

$$\eta_2 = \frac{2a\left(L - |Z(t)|\right)}{2\pi R_0 L} = \frac{a}{\pi R_0}\left(1 - \frac{Z_0}{L}|\sin \omega t|\right) \tag{10}$$

The heat flux can now be written as:

$$Q(t) = (1-\eta_1)\frac{a f_0 \omega Z_0 p_0}{\pi R_0}\left(1 - \frac{Z_0}{L}|\sin \omega t|\right)|\cos \omega t| \tag{11}$$

Assuming:

$$Q(t) = \theta_0^0 h_0(t) \text{ i } z_0 = \frac{Z_0}{L} \tag{12}$$

we obtain:

$$\theta_0^0 = (1-\eta_1)\frac{a f_0 \omega Z_0 p_0}{\pi R_0} \tag{13}$$

$$h_0(t) = \left(1 - z_0 |\sin \omega t|\right)|\cos \omega t| \tag{14}$$

Below, in Fig. 2, there is shown an exemplary graph of the function $h_0(t)$ for $z_0 = 0.2$.

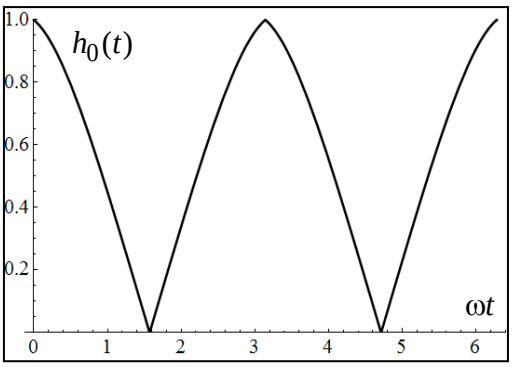

Fig. 2. The evolution of the heat flux due to the rollers' reciprocation motion

3. NON-STATIONERY SOLUTION

On the proposed model equation (1) we perform Laplace transform (Carslaw et al., 1959; Abramowitz et al., 1965) defined by the relationship (s – transform parameter):

$$\left\{\overline{T}_1(R,s), \overline{h}_n(s), \overline{Q}(s)\right\} = \int_0^\infty \left\{T_1(R,t), h_n(t), Q(t)\right\} e^{-st} dt \tag{15}$$

As a result of the Laplace transform we obtain second-order differential equation (*modified Bessel equations*):

$$\frac{\partial^2 \overline{T}_1(R,s)}{\partial R^2} + \frac{1}{R}\frac{\partial \overline{T}_1(R,s)}{\partial R} = \frac{s}{k_1}\overline{T}_1(R,s)\,,\ R_1 < R < R_0 \tag{16}$$

and boundary conditions:

$$\lambda_1 \frac{\partial \overline{T}_1(R_1,s)}{\partial R} - \alpha_1^T \left[\overline{T}_1(R_1,s) - \overline{T}_1^{\,0}(s)\right] = 0 \tag{17}$$

$$\lambda_1 \frac{\partial \overline{T}_1(R_0,s)}{\partial R} + \alpha_2^T \left[\overline{T}_1(R_0,s) - \overline{T}_2^{\,0}(s)\right] = \overline{Q}(s) \tag{18}$$

The general solution of the equations system (16)-(18) has the form (Carslaw et al., 1959; Abramowitz et al., 1965):

$$\overline{T}_1(R_1,s) = C_3^1 I_0(q_1 R) + C_4^1 K_0(q_1 R),\ q_1 = \sqrt{\frac{s}{k_1}} \tag{19}$$

We find required differential (Abramowitz et al., 1965):

$$\frac{d\overline{T}_1(R,s)}{dR} = q_1 C_3^1 I_1(q_1 R) - q_1 C_4^1 K_1(q_1 R) \tag{20}$$

After introducing equations (19)-(20) into the boundary conditions (17)-(18) we get a set of two equations with two unknowns: C_1^1 and C_2^1:

$$\lambda_1\left(s_1 C_3^1 I_1(s_1 R_1) - s_1 C_4^1 K_1(s_1 R_1)\right) - \alpha_1^T\left(C_3^1 I_0(s_1 R_1) + C_4^1 K_0(s_1 R_1)\right) = -\alpha_1^T \theta_1^0 \overline{h}_1(s) \tag{21}$$

$$\lambda_1\left(s_1 C_3^1 I_1(s_1 R_0) - s_1 C_4^1 K_1(s_1 R_0)\right) + \alpha_2^T\left(C_3^1 I_0(s_1 R_0) + C_4^1 K_0(s_1 R_0)\right) = +\alpha_2^T \theta_2^0 \overline{h}_2(s) + \overline{Q}(s) \tag{22}$$

By entering constants obtained from the equations (21)-(22) into the general solution (19) we receive the final solution and write it in form:

$$\overline{T}_1(R,s) = \sum_{n=0}^{2}\left[\frac{\overline{\theta}_{1n}(R,s)}{\Delta(s)}\theta_n^0 \overline{h}_n(s)\right] \tag{23}$$

where: $\Delta(s) = Bi_2 Q_2^{(1)}(R_0,R_1,s) + Q_1^{(1)}(R_0,R_1,s)$

$\overline{\theta}_{10}(R,s) = R_0\lambda_1^{-1}Q_2^{(1)}(R,R_1,s) = (\alpha_2^T)^{-1}Bi_2 Q_2^{(1)}(R,R_1,s)$

$\overline{\theta}_{11}(R,s) = Bi_1 Q_1^{(2)}(R_0,R,s)$, $\overline{\theta}_{12}(R,s) = Bi_2 Q_2^{(1)}(R,R_1,s)$

$Q_2^{(1)}(x,y,s) = Bi_1 Z_{00}^{(1)}(x,y,s) + Z_{10}^{(1)}(y,x,s)$

$Q_1^{(2)}(x,y,s) = Bi_2 Z_{00}^{(1)}(x,y,s) + Z_{10}^{(1)}(x,y,s)$

$Z_{00}^{(1)}(x,y,s) = I_0(q_1 x)K_0(q_1 y) - I_0(q_1 y)K_0(q_1 x)$

$Z_{11}^{(1)}(x,y,s) = I_1(q_1 x)K_1(q_1 y) - I_1(q_1 y)K_1(q_1 x)$

$Z_{10}^{(1)}(x,y,s) = q_1 x\left(I_1(q_1 x)K_0(q_1 y) + I_0(q_1 y)K_1(q_1 x)\right)$

By entering obtained from set of equations (21)-(22) constants into general solution (20) we receive the form of heat flux:

$$\overline{Q}_1(R,s) = \lambda_1\frac{\partial\overline{T}_1(R,s)}{\partial R} = \sum_{n=0}^{2}\left[\frac{\overline{Q}_{1n}(R,s)}{\Delta(s)}\theta_n^0 \overline{h}_n(s)\right] \tag{24}$$

where:

$\overline{Q}_{10}(R,s) = \lambda_1 R_0\left(Bi_1 Z_{10}^{(1)}(R,R_1,s)/R - q_1 q_1 R_1 Z_{11}^{(1)}(R_1,R,s)\right)$

$\overline{Q}_{11}(R,s) = \lambda_1 Bi_1 Q_1^{(2)}(R_0,R,s) = \lambda_1 Bi_1\left(-Bi_2 Z_{10}^{(1)}(R,R_0,s)/R - q_1 q_1 R_0 Z_{11}^{(1)}(R_0,R,s)\right)$

$\overline{Q}_{12}(R,s) = \lambda_1 Bi_2 Q_2^{(1)}(R,R_1,s) = \lambda_1 Bi_2\left(Bi_1 Z_{10}^{(1)}(R,R_1,s)/R - q_1 q_1 R_1 Z_{11}^{(1)}(R_1,R,s)\right)$

$Q_2^{(1)}(x,y,s) = Bi_1 Z_{00}^{(1)}(x,y,s) + Z_{10}^{(1)}(y,x,s)$

$Q_1^{(2)}(x,y,s) = Bi_2 Z_{00}^{(1)}(x,y,s) + Z_{10}^{(1)}(x,y,s)$

Above we have taken indications as follows: $I_m(z)$, $K_m(z)$ – modified mth-order Bessel functions, of first and second kind respectively Abramowitz et al., 1965), $B_{i1} = R_1\alpha_1^T/\lambda_1$, $B_{i2} = R_0\alpha_2^T/\lambda_1$ – Biot's numbers (Carslaw et al., 1959). Temperature transform $\overline{T}_1(R,s)$ and heat flux transform have been written in forms (23) and (24) by means of functions $Z_{ml}^{(n)}(x,y,s)$, which are defined above.

The Laplace transform of periodic function (14) has the form:

$$\overline{h}_0(s) = \frac{2\omega e^{\pi s/2\omega} - s + se^{\pi s/\omega}}{(e^{\pi s/\omega}-1)(s^2+\omega^2)} - \frac{3z_0(e^{\pi s/2\omega}+1)}{(e^{\pi s/2\omega}-1)(s^2+4\omega^2)} \tag{25}$$

4. ANALYSIS

The analysis of obtained Laplace transforms shows that the peculiarities of these transforms can be only zero points of the characteristic function $\Delta(s)$ and the peculiarities of Laplace transforms $\overline{h}_n(s)$.

Using the Laplace transform method and Borel convolution theorem we find the solution and write roller temperature and the heat flux in the forms as follows (Piętak et al., 2011; Jurkiewicz et. al., 2011):

$$T_1(R,t) = \sum_{n=0}^{2}\left[\frac{\overline{\theta}_{1n}(R,0)}{\Delta(0)} + \sum_{k=1}^{\infty}\frac{\overline{\theta}_{1n}(R,s_k)}{s_k\Delta'(s_k)}\exp(s_k t)\right] * \frac{d}{dt}\left(\theta_n^0 h_n(t)\right) \tag{26}$$

$$Q_1(R,t) = \sum_{n=0}^{2}\left[\frac{\overline{Q}_{1n}(R,0)}{\Delta(0)} + \sum_{k=1}^{\infty}\frac{\overline{Q}_{1n}(R,s_k)}{s_k\Delta'(s_k)}\exp(s_k t)\right] * \frac{d}{dt}\left(\theta_n^0 h_n(t)\right) \tag{27}$$

where: $\Delta'(s_k) = d\Delta(s)/ds|_{s=s_k}$.

Roots s_k of the characteristic equation $\Delta(s) = 0$ lie on the negative part of the real axis of complex plane of Laplace transform parameter, i.e.: $s_k = -\mu_k^2$.

For example, the thermostatted vibrator roller in the machine Heidelberg XL105 (according to technical drawing) has a diameter $2R_0 = 84.8\cdot10^{-3}\mathrm{m}$ and length $L = 1085\cdot10^{-3}\mathrm{m}$, width of the contact zone $2a = 5\cdot10^{-3}\mathrm{m}$, displacement of the roller along the axis $z_0 = 17.5\cdot10^{-3}\mathrm{m}$, coolant flow diameter $2R_1 = 15\cdot10^{-3}\mathrm{m}$. We assume that:

- the roller is made of steel (according to VanSant (1983): $\lambda_1 = 21\ W/(m°\mathrm{C})$, $k_1 = 0.7\cdot10^{-5}\mathrm{m}^2/s$);
- the cooling fluid is the water at a temperature $\theta_1^0 h_1(t)$ under conditions of forced flow into the pipe ($\alpha_1^T = 2000W/(m°\mathrm{C})$);
- and the surrounding is the air at the temperature $\theta_2^0 h_2(t)$ under conditions of forced flow near the surface of the roller ($\alpha_2^T = 10W/(m°\mathrm{C})$).

The preliminary analysis was performed for the case when functions $h_n(t)$ for $n = 0, 1, 2$ are Heaviside step functions $H(t)$ ($H(t) = 0$ for $t < 0$ and $H(t) = 1$ for $t < 0$). Instead of periodic function $h_0(t)$ with the period π/ω we took in to account also the Heviside function $H(t)$ with the amplitude equel to the average value h_0 of this function:

$$h_0 = \frac{\omega}{\pi}\int_0^{\pi/\omega} h_0(t)dt = \frac{2-z_0}{\pi} \tag{28}$$

We examine the case where at the surface of the roller $R = R_0$ due to the friction acts the heat flux Q with amplitude $\theta_0^0 = 4000\mathrm{W/m}^2$, the surrounding temperature increases in amount of $\theta_2^0 = 5°\mathrm{C}$, and the coolant temperature is lower in amount of $\theta_1^0 = -20°\mathrm{C}$.

First roots of the characteristic equation $\Delta(s) = 0$ are as follows: $s_1 = -3.39 \cdot 10^{-3}$, $s_2 = -8.55 \cdot 10^{-2}$, $s_3 = -2.68 \cdot 10^{-1}$, $s_4 = -5.57 \cdot 10^{-1}$, $s_5 = -9.57 \cdot 10^{-1}$, $s_6 = -1.47$, $s_7 = -2.09$, $s_8 = -3.83$.

Taking into account the the first 17 roots of the chareacteristic equation in the formula (26) we show in Fig. 3 the evolution of the changes in the temperature of the roller surface $R = R_0$ (curve 1).

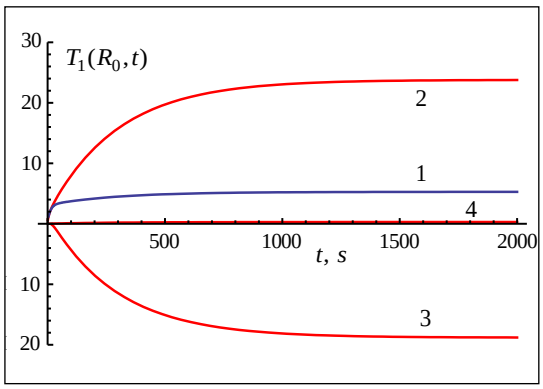

Fig. 3. The evolution of temperature changes at the roller surface $R = R_0$

Curve 2 presents roller surface temperature changes in case when the surrounding temperature increase and the coolant temperature change are both zero. The change of the roller surface temperature ($R = R_0$) in time in case when there is no friction and no changes of the surrounding temperature shows the curve 3 in Fig. 3. The change in roller surface temperature ($R = R_0$) caused by the increase of the surrounding temperature illustrates the curve 4 in Fig. 3.

The evolution of the roller temperature at surface $R = R_1$ we present in Fig. 4 (curve 1). Curve 2 in Fig. 4 describes evolution of roller internal surface ($R = R_1$) temperature which is a result of the heat flux operating at the surface $R = R_0$ in case when the surrounding temperature is constant ($\theta_1^0 h_1(t) = 0$) and there is no change in the coolant temperature. Changes in the temperature at internal roller surface in case when there is no friction and no changes in surrounding temperature are presented by curve 3 in Fig. 4. Changes in the temperature at internal surface $R = R_1$ caused by increase in the surrounding temperature shows curve 4 in Fig. 4.

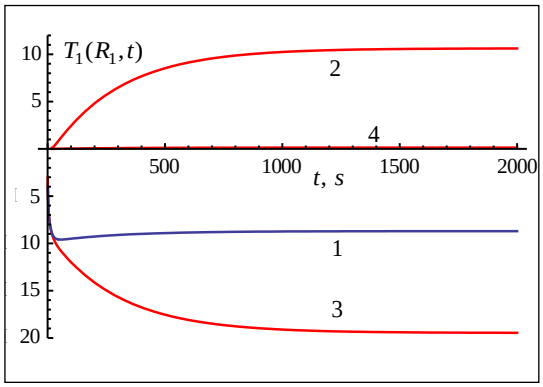

Fig. 4. The evolution of temperature changes at the roller surface $R = R_1$

The roller temperature distribution $T_1(R,t)$ along the roller radius R is shown in Fig. 5. Curves 1-5 correspond to the temperature distribution, respectively at time $t = 10,\ 50, 100,\ 500, 2000$ s.

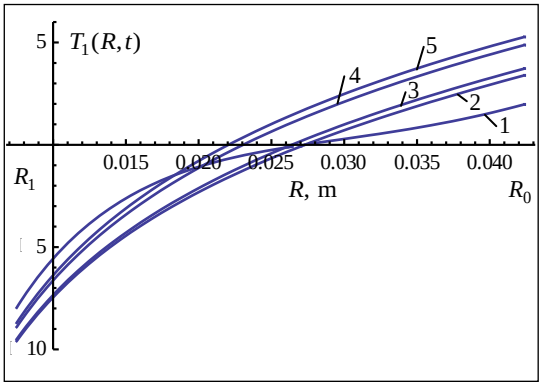

Fig. 5. The temperature distribution along the roller radius at different time instants

5. CONCLUSIONS

We obtain an analytical solution of the heat conduction problem for the inking unit in the offset printing machine. It has been proven that the functions $Z_{ml}^{(n)}(x,y,s)$, which we entered into transforms' formulas of the roller temperature (23) and the heat flux (24), are analytic functions.

It is worth noting, that the first terms of obtained formulas of roller temperature (26) and heat flux (27) corresponds to the stationary solution ($t \to \infty$ of this problem received in the earlier work (Piętak et al., 2011) for the case when the functions $h_n(t)$ where $n = 0, 1, 2$ are Heaviside step functions (unit step function).

We assume that the inking is at temperature $22°C$. During the printing process (when machine is working) the heat flux is generated at the surface of the vibrator roller ($R = R_0$) as a result of friction. The heat flux causes heating of the roller. If there is no cooling, the temperare increase overe time in amount of $24°C$ and reaches the level of $46°C$ (curve 2, Fig. 3). Offset printing technology requires lower temperature of the roller surface and of the ink transported by the roller. Therfore, in modern inking units rollers are thermostatted. When we take into account the coolant inside the roller we receive an increase of roller surface temperature in amount of only $5°C$ (curve 1 in Fig. 3). This way our model allows to simulate the temperature distribution in one of the elements of the prinitng unit of the offset printing machine and to regulate coolant temperature depending on the surrounding temperature changes and printing parameters, such as speed and properties of the ink.

The obtained solution makes it possible to determine and to regulate the time necessary to reach the stationery coditions of the temperature. Stationery conditions of the temeperature gurantee the stability of the printing process and less paper waste. In this way we can affect the amount of foracasted paper and ink waste.

We woluld like also notice that various forms of solutions for the cylinder (roller) are showed, e.g. in works of Carslaw et al. (1959) and VanSant (1983).

REFERENCES

1. **Abramowitz M, Stegun I.** (1965) *Handbook of mathematical functions: with formulas, graphs, and mathematical tables*, Dover Publications Inc., New York
2. **Awrejcewicz J., Grzelczyk D.** (2013) Modeling and analysis of thermal processes in mechanical friction clutch-numerical and experimental investigations, *International Journal of Structural Stability and Dynamics,* Vol. 13, No. 7, 1340004-1-18.
3. **Awrejcewicz J.**, **Pyryev Y.** (2009) *Nonsmooth Dynamics of Contacting Thermoelastic Bodies*, Springer Varlag.
4. **Blok H.** (1940) Fundamental mechanical aspects of boundary lubrication, *S.A.E. J*., 40, 2, 54-68.
5. **Carslaw H. S., Jaeger J. C.** (1959) *Conduction of heat in solids,* Clarendon Pres, Oxford.
6. **Chou, S.M., L.J. Bain, R. Durand, Sanderson E.** (1996) Novel printing press for waterless lithography. *In: TAPPI Proceedings, International Printing & Grpahic Arts Conference. Atlanta*, 165–174.
7. **Jurkiewicz A., Krzyżkowski J., Piętak Z., Pyr'yev Y.** (2011) Modeling of selected phenomena which occur in offset printing presses, [In:] *Scientific basis of modern technologies: experience and prospects*, Shalapko Y. I., Dobrzanski L. A., Jaremche, 154-168.
8. **Olejnik P., Awrejcewicz J.** (2013) Low-speed voltage-input tracking control of a DC-motor numerically modelled by a dynamical system with stick-slip friction, *Differential Equations and Dynamical Systems*, Vol. 21, No. 1-2, 3-13.
9. **Piętak Z. M., Pyryev Y.** (2011) Mathematical modelling and description of friction and temperature phenomena in inking unit of the offset printing machine, *Challenges of Modern Technology*, Vol. 2, No. 1, 41-44.
10. **Pyryev Y., Piętak Z.M.** (2010) Modelowanie i opis matematyczny zjawisk tarciowych w zespole farbowym offsetowej maszyny drukującej, *VI International Conference "Friction 2010". Modelling and Simulation of the Friction Phenomena in the Physical and Technical Systems*, Warszawa, 111- 116.
11. **Talati F., Jalalifar S.** (2009) Analysis of heat conduction in a disk brake system, *Heat Mass Transfer*, Vol. 45, No. 8, 1047–1059.
12. **VanSant J. H.** (1983) *Conduction heat transfer solution*s, CA: Lawrence Livermore National Laboratory, University of California, Livermore.
13. **Yevtushenko A., Kuciej M.** (2009) Temperature in a frictionally-heated ceramic-metal patch and cast iron disc during braking, *Numerical Heat Transfer, Part A: Applications: An International Journal of Computation and Methodology,* Vol. 56, No. 2, 97-108.
14. **Yevtushenko A., Kuciej M.** (2012) One-dimensional thermal problem of friction during braking: The history of development and actual state, *International Journal of Heat and Mass* Transfer, Vol. 55, No. 15-16, 4148-4153.

Acknowledgment: The work has been supported by the European Union in the framework of European Social Fund through the Warsaw University of Technology Development Programme.

SIMULATION OF POWDER SINTERING USING A DISCRETE ELEMENT MODEL

Jerzy ROJEK[*], Szymon NOSEWICZ[*], Katarzyna PIETRZAK[*,], Marcin CHMIELEWSKI[**]**

[*]Institute of Fundamental Technological Research, Polish Academy of Sciences, ul. Pawińskiego 5B, 02-106 Warsaw, Poland
[**]Institute of Electronic Materials Technology, ul. Wólczyńska 133, 01-919 Warsaw, Poland

jrojek@ippt.gov.pl, snosew@ippt.gov.pl, katarzyna.pietrzak@itme.edu.pl, chmielem@poczta.fm

Abstract: This paper presents numerical simulation of powder sintering. The numerical model introduced in this work employs the discrete element method which assumes that material can be modelled by a large assembly of discrete elements (particles) of spherical shape interacting among one another. Modelling of sintering requires introduction of the cohesive interaction among particles representing inter-particle sintering forces. Numerical studies of sintering have been combined with experimental studies which provided data for calibration and validation of the model. In the laboratory tests evolution of microstructure and density during sintering have been studied. Comparison of numerical and experimental results shows a good performance of the numerical model developed.

Key words: Powder Sintering, Simulation, Discrete Element Method

1. INTRODUCTION

Sintering is a manufacturing process used for making various parts from metallic or ceramic powder mixtures. Sintering consists in consolidation of loose or weakly bonded powders at elevated temperatures, close to the melting temperature with or without additional pressure. This is a complex process affected by many factors. Numerical simulation of sintering can be used to optimize and to understand better the process and improve the quality of sintered components.

Modelling of sintering process is still a challenging research task. There are different approaches in modeling of sintering processes, ranging from continuum phenomenological models (Abouaf et al., 1988; Duva and Crow, 1992; Cocks, 1989; Sofronis and McMeeking, 1992; Ponte Castañeda, 1991) to atomistic ones (Zeng et al., 1998; Zachariah and Carrier, 1999; Zhu and Averback, 1995; Huilong and Averback, 1996; Matsubara, 1999; Kadau et al., 2002). Growing capabilities of computational techniques increased the possibilities to employ particle sintering models. Sintering models have been implemented within the discrete element method which allows us to model interaction of large collections of particles (Parkami and McMeeking, 1998; Martin et al., 2006; Luding et al., 2005; Olmos et al., 2009; Kadushnikov et al., 2001; Henrich , 2007; Henrich et al., 2007; Wonisch et al., 2009). In the paper of the Parhami and McMeeking (1998) it have been implemented the particle sintering model derived by Coble (1958) in the quasi-static formulation of the lattice type discrete element method to study free and pressure-assisted sintering. The concepts of Parhami and McMeeking have been incorporated in the dynamic formulation of the discrete element method by Martin et al. (2006) and used for investigation of free sintering of metallic powders. A similar model has been applied by Henrich et al. (2007) to simulate the free and pressure-assisted solid state sintering of powders with special attention to the grain rearrangement during sintering. The effect of particle size distributions on sintering has been studied by Wonisch et al. (2009).

In the presented work the discrete element method is adopted as a modelling tool. The discrete model has been performed to predict micro- and macroscopic changes during sintering process. The discrete model allows to determine interaction of grains and evaluate the density of material. The numerical model is validated using the results of experimental studies of a sintering process.

2. EXPERIEMENTAL STUDIES OF A SINTERING PROCESS

Experimental studies of sintering have been performed in the laboratory of Institute of Electronic Materials Technology. Sintering has been carried out in a Thermal Technology Astro uniaxial hot press shown in Fig. 1. Morphology of the NiAl powder used for sintering is presented in Fig. 2. The samples of the sintered material are shown in Fig. 3. Sintering has been performed under pressure of 30 MPa and at temperature of 1400 ^{O}C. Temperature variation during the process is plotted in Fig. 4. The process was interrupted at different time instants in order to study the evolution of microstructure and kinetics of sintering. The measurement points are marked on the plot in Fig. 4. The kinetics of sintering can be evaluated by investigation of the bulk density change in time. The macroscopic shrinkage of the porous material during sintering leads to the increase of the bulk density. The evolution of the bulk density obtained in our studies is given in Tab. 1. The value of the bulk density close to the theoretical density has been obtained. It means that the material with very low porosity has been obtained by keeping the sample at sintering temperature for a sufficiently long time. The evolution of the bulk density obtained in our studies will be used in calibration of the numerical model.

During sintering particulate material is converted into polycrystal. In the initial stage cohesive bonds (necks) are formed between grains. Microstructure at an early stage of sintering is shown in Fig. 5a. When the sintering process is continued the necks between particle grow (Fig. 5b). Grain rearrangement and increase of grain compaction can be observed during sintering. With the advancement of the sintering process, gradual reduction and elimination of porosity is observed (Figs. 5b and 5c).

Fig. 1. Thermal Technology Astro uniaxial hot press

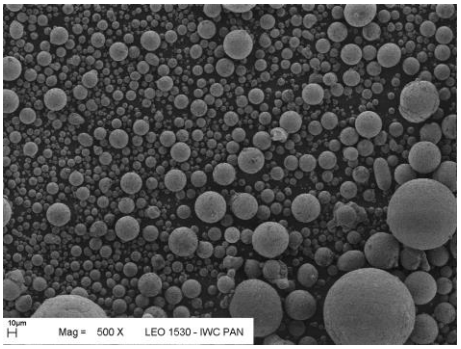

Fig. 2. Morphology of the NiAl powder

Fig. 3. Samples of sintered material

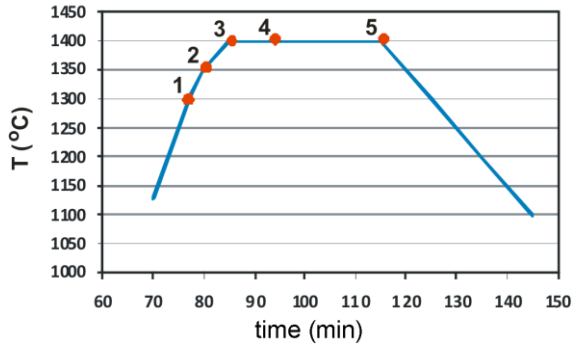

Fig. 4. Temperature variation during sintering of NiAl with measurement points

a)

b)

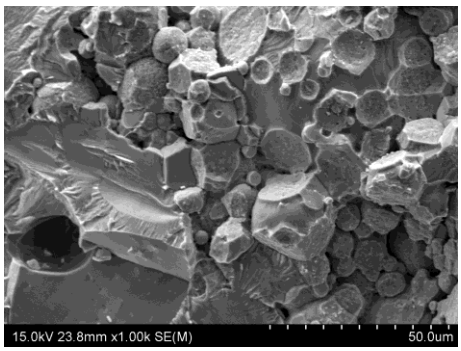

c)

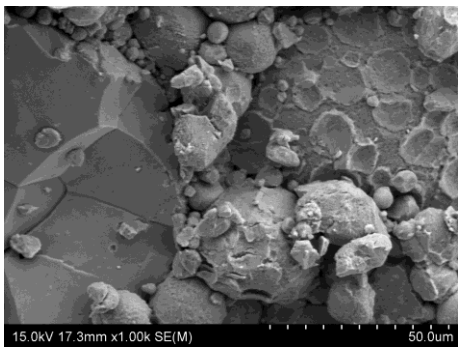

Fig. 5. Microstructure evolution during sintering of NiAl: a) early stage (measurement point P1), b) intermediate stage (P4), b) final stage (P5)

Tab. 1. Density evolution of NiAl during sintering (theoretical density of NiAl: 5.91 g/cm^3)

Measurement point	bulk density (g/cm3)	relative density (%)
1	5.25	88.8
2	5.35	90.5
3	5.42	91.7
4	5.78	97.8
5	5.86	99.1

3. NUMERICAL MODEL OF SINTERING

Numerical model of sintering is developed within the framework of the discrete element method which assumes that a particulate material can be represented as a collection of spherical particles interacting mutually, thus the discrete element model takes explicitly into account the particulate nature of the sintered material (Rojek et al., 2011). The numerical model of sintering has been implemented in the finite/discrete element code DEMPack (Rojek et al., 2011).

3.1. Discrete element method formulation

In the discrete element method, the translational and rotational motion of rigid spherical elements (particles) is governed by the standard equations of rigid body dynamics. For the *i*-th spherical particle we have:

$$m_i \ddot{\mathbf{u}}_i = \mathbf{F}_i \tag{1}$$

$$J_i \dot{\boldsymbol{\omega}}_i = \mathbf{T}_i \tag{2}$$

where $\mathbf{u}_i$ is the element centroid displacement in a fixed (inertial) coordinate frame $\mathbf{X}$, $\boldsymbol{\omega}_i$ – the angular velocity, m_i – the element mass, J_i – the moment of inertia, $\mathbf{F}_i$ – the resultant force, and $\mathbf{T}_i$ – the resultant moment about the central axes. Equations (1) and (2) are integrated in time using the explicit central difference time integration scheme. Taking appropriate contact model we can obtain desired macroscopic behaviour. Therefore the contact model in the discrete element method can be considered as a micromechanical material model. Modelling of sintering requires special model of contact interaction. Below the contact models for powder compaction and powder sintering will be presented.

3.2. Contact interaction model for powder compaction

Powder compaction prior to sintering is modelled using the cohesionless contact model with friction. The rheological scheme of this model is shown in Fig. 6. The normal contact interaction is represented by the Kelvin-Voigt element consisting of a spring and a dashpot connected in parallel. The normal contact force F_n is a sum of the elastic force in the spring F_e and the viscous component F_d

$$F_n = F_e + F_d \tag{3}$$

The elastic part of the normal contact force F_e can be evaluated assuming a linear force–displacement relationship:

$$F_e = k_n u_n \tag{4}$$

where k_n is the normal contact stiffness and u_n is the penetration of the two particles, calculated as:

$$u_n = d_{ij} - R_i - R_j \tag{5}$$

where d_{ij} is the distance of the particle centres, and R_i and R_j their radii.

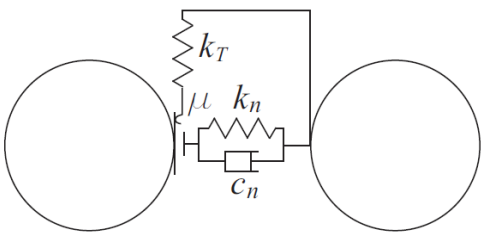

Fig. 6. Rheological scheme of the contact interaction for powder compaction

No cohesion is allowed, so no tensile normal contact forces are allowed:

$$F_e \leq 0 \tag{6}$$

The viscous component of the normal force is assumed to be a linear function of the normal relative velocity v_n at the contact point:

$$F_d = c_n v_n \tag{7}$$

The value of the viscosity coefficient c_n can be taken as a fraction ξ of the critical damping C_{cr} for the system of two rigid bodies with masses m_i and m_j, connected with a spring of the stiffness k_n:

$$c_n = \xi C_{cr} \tag{8}$$

where the critical damping can be calculated:

$$C_{cr} = 2\sqrt{\frac{m_i m_j k_n}{m_i + m_j}} \tag{9}$$

The tangential reaction F_t at the contact point is brought about by the friction opposing the relative motion. In our model, friction is modelled using the regularized Coulomb friction model characterized by the tangential contact stiffness k_t and friction coefficient μ.

3.3. Contact interaction model for sintering

When during heating the sintering temperature is reached the interaction model type is switched from that representing powder compaction to the model appropriate for sintering. Conversely, when the temperature drops below the sintering temperature during cooling or when the sintering process reaches equilibrium, the interaction model is switched back to the model presented in Sec. 3.2.

Modelling of sintering requires introduction of a cohesive interaction among particles representing inter-particle sintering forces. As a result of the stresses in the neck and the surface tension the particles are attracted to each other leading to shrinkage of the system (Hosford, 2006). Considering the relationship between the diffusion and stress state Coble (1958), Johnson (1969) and De Jonghe & Rahaman (1988) formulated mathematical models for sintering force between two particles. The discrete element method provided a suitable framework for more general application of these models (Parhami and McMeeking, 1998; Martin et al., 2006).

In our model, the particle interaction during sintering is described by the equation derived by Parhami and McMeeking (1998):

$$F_n = \frac{\pi a^4}{8 D_b} v_n - \pi \gamma_s \left[4R \left(1 - cos\frac{\Psi}{2} \right) + asin\frac{\Psi}{2} \right] \tag{10}$$

where F_n is the normal force between two particles, v_n – the normal relative velocity, R – the particle radius, a – the sintering contact radius, Ψ – the dihedral angle, γ_s – the surface energy and D_b – the effective grain boundary diffusion coefficient. The geometric parameters used in Eq. (10) are defined in Fig. 7. In our model the translational motion will be considered only, assuming that the rotational motion is negligible in sintering. The tangential component is assumed as small in comparison with the normal one and is neglected.

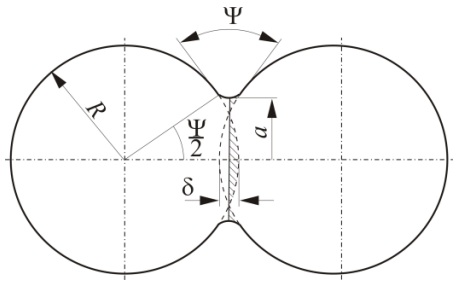

Fig. 7. Model parameters definition

The effective diffusion coefficient is given by the following equation, cf. (Parhami and McMeeking, 1998):

$$D_b = \frac{D_g \delta_g \Omega}{kT} \tag{11}$$

where D_g – diffusion coefficient, δ_g– thickness of the grain boundary, Ω – atomic volume, k – Boltzmann constant, T – sintering temperature. The initial neck radius a_0 depends on the initial penetration u_0 induced by the compaction. From simple geometrical considerations we have:

$$a_0 = \sqrt{\frac{R u_{n0}}{2}} \tag{12}$$

The growth of the radius of the interparticle grain boundary is governed by the following evolution law:

$$\dot{a} = -\frac{R v_n}{a} \tag{13}$$

The grain boundary radius a grows until the sintering process is stopped. Its maximum at the equilibrium state is given by the following geometric relationship:

$$a_{max} = R \sin\frac{\Psi}{2} \tag{14}$$

where: Ψ is the dihedral angle determined according to the Young's law which assumes that in the system consisting of two grains and a gas in the pore in the equilibrium we have equlibrium of surface tensions.

The model described by Eq. (10) has been derived for identical particles. Following (Martin et al., 2006) it can be generalized for different size particles by replacing the radius R in Eqs. (10)–(13) with the equivalent particle radius $\bar{R}$ given by the following formula:

$$\bar{R} = -\frac{2R_i R_j}{R_i + R_j} \tag{15}$$

On the right-hand side of Eq. (10) we have two terms, the first term has a character of viscous resistance to the particle approaching caused by the sintering attracting force represented by the second term. Denoting these force components, F^v and F^{sint}, respectively, Eq. (10) can be rewritten as follows:

$$F_n = F^v + F^{sint} \tag{16}$$

where:

$$F^v = \frac{\pi a^4}{8 D_b} v_n \tag{17}$$

$$F^{sint} = -\pi\gamma_s \left[4R\left(1 - cos\frac{\Psi}{2}\right) + asin\frac{\Psi}{2}\right] \tag{18}$$

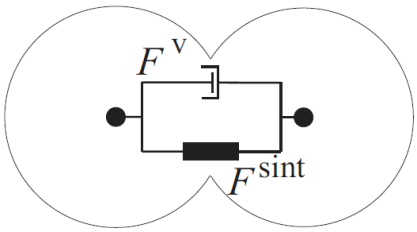

Fig. 8. Rheological scheme of the sintering model

The decomposition (15) of the interaction force in the sintering model can be represented by the rheological scheme shown in Fig. 8.

4. SIMULATION OF SINTERING OF A CYLINDRICAL SPECIMEN

The model implementation has been validated using the results of laboratory tests of sintering of NiAl powder presented in Sec. 2 Maintaining the original grain size (particle mean diameter 25 μm), a cylindrical container of diameter 200 μm has been filled with 350 particles (Fig. 9a). It has been assumed that such a reduced geometric model represents correctly sintering process in a real specimen with diameter of 120 mm. This assumption is justified provided the parameters characterizing sintering are uniformly distributed in a real specimen volume.

The particles in equilibrium under gravity (Fig. 9a) have been subjected to linearly rising compressive pressure of the rigid punch until the final load of 30 MPa has been achieved. Then the increase of temperature to 1400 ^{O}C has been prescribed and the sintering process has been activated. The sintering has been treated as an isothermal process. The final configuration of the particles after sintering for 30 mins is shown in Fig. 9b. A significant reduction of the specimen height due to macroscopic shrinkage can be clearly observed.

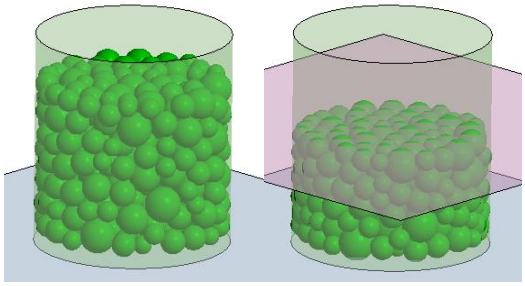

a) b)

Fig. 9. Simulation of sintering: a) initial configuration, b) final configuration

The model parameters are given in Tab. 2. In the calibration procedure, the effective diffusion coefficient, has been treated as a fitting parameter similarly as in Wonisch et al., (2009). The other parameters have been kept constant during calibration. Their values have been estimated based on literature data.

In order to increase numerical efficiency of the simulation based on the explicit time integration mass scaling has been employed. Mass scaling is typically used in the explicit time integration to increase a critical time step value. Since the

process is very slow, it is possible to increase algorithmically inertial terms without affecting much the whole solution.

The calibration procedure has been based on fitting the density evolution to experimental results The relative density evolution obtained in the numerical simulation shown in Fig. 10 agrees well with experimental measurements which demonstrates a good performance of the numerical model.

Tab. 2. Material data and model parameters for NiAl sintering

Parameter name	Parameter value
Density,	5.91 g/cm^3
Contact stiffness, k_n and k_t	7·10^5 N/m
Damping coefficient, ξ	0.7
Friction coefficient, μ	0.05
Diffusion coefficient, $D_g\delta_g$	1.8·10^{-19} m^3/s
Atomic volume, Ω	1.21·10^{-29} m^3
Surface energy, γ_s	1.58 J/m^2
Dihedral angle, Ψ	150^O

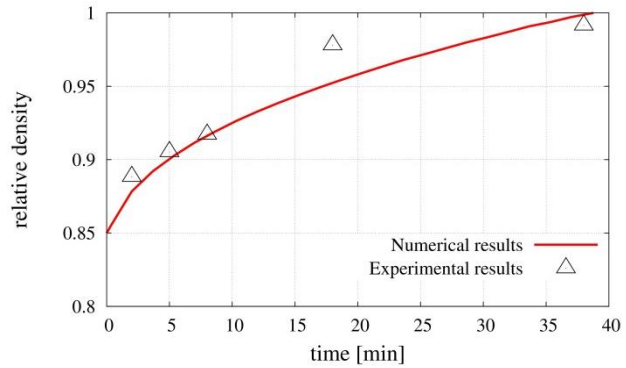

Fig. 10. Evolution of relative density during sintering process

5. CONCLUDING REMARKS

The results presented in the paper show a big potential of the presented numerical model in simulation of powder sintering. The discrete element method is a suitable tool to model powder sintering. The model reproduces correctly mechanism of sintering under pressure (shrinkage, change of density). The evolution of the density has been studied in this paper, however, the model can also be used to investigate other phenomena of a sintering process such as stresses during and after process. Further work on extension of the model is ongoing.

REFERENCES

1. **Abouaf M., Chenot J.L., Raisson G., Bauduin P.** (1988), Finite element simulation of hot isostatic pressing of metal powders, *International Journal for Numerical Methods in Engineering*, 25, 191–212.
2. **Coble R.L. (**1958), Initial Sintering of Alumina and Hematite, *J. Amer. Ceramic Soc*., 41, 55-62.
3. **Cocks A.C.F.** (1989), Inelastic deformation of porous materials, *Journal of the Mechanics and Physics of Solids*, 37 (6), 693–715.
4. **De Jonghe L.C., Rahaman M.N**. (1988), Sintering Stress of Homogeneous and Heterogeneous Powder Compacts, *Acta Metall*., 36, 223-229.
5. **Duva J.M., Crow P.D.** (1992), The densification of powders by power-law creep during hot isostatic pressing, *Acta Metallurgica et Materialia*, 40, 31–35.
6. **Henrich B**. (2007), (PhD thesis) Partikelbasierte Simulationsmethoden in Pulvertechnologie und Nanofluidik, Albert-Ludwigs-Universität Freiburg im Breisgau.
7. **Henrich B., Wonisch A., Kraft T., Moseler M., Riedel H.** (2007), Simulations of the influence of rearrangement during sintering, *Acta Materialia*, 55, 753–762.
8. **Hosford W.F.** (2006)**,** *Material Science*, Cambridge University Press.
9. **Huilong Z., Averback R.S.** (1996), Sintering processes of two nanoparticles: a study by molecular-dynamics simulations, *Phil. Mag. Let*., 73(1), 27–33.
10. **Johnson D.L**. (1969), New Method of Obtaining Volume, Grain Boundary, and Surface Diffusion Coefficients from Sintering Data, *Journal of Applied Physics*, 40, 192-200.
11. **Kadau K., Entel P., Lomdahl P.S.** (2002), Molecular-dynamics study of martensitic transformations in sintered Fe–Ni nanoparticles, *Computer Physics Communications*, 147, 126–129.
12. **Kadushnikov R.M., Skorokhod V.V., Kamenin I.G., Alievskii V.M., Yu Nurkanov E., Alievskii D.M.** (2001), Theory and technology of sintering, heat, and chemical heat-treatment processes computer simulation of spherical particle sintering. *Powder Metallurgy and Metal Ceramics*, 40(3-4), 154–163.
13. **Luding S., Manetsberger K., Müllers J.** (2005)**,** A discrete model for long time sintering, *Journal of Mechanics and Physics of Solids*, 53, 455–491
14. **Martin C.L., Schneider L.C.R., Olmos L., Bouvard D**. (2006), Discrete element modeling of metallic powder sintering, *Scripta Materialia*, 55, 425–428.
15. **Matsubara H.** (1999), Computer simulations for the design of microstructural developments in ceramics, *Computational Materials Science*, 14, 125–128.
16. **Olmos L., Martin C.L., Bouvard D.** (2009), Sintering of mixtures of powders: experiments and modelling, *Powder Technology*, 190, 134–140.
17. **Parhami F., McMeeking R.M**. (1998), A network model for initial stage sintering,Mechanics of Materials, 27, 111-124.
18. **Ponte Castañeda P.** (1991), The effective mechanical properties of nonlinear isotropic composites, *Journal of the Mechanics and Physics of Solids*, 39, 45–71.
19. **Rojek J., Pietrzak K., Chmielewski M., Kaliński D., Nosewicz S.** (2011), Discrete Element Simulation of Powder Sintering, *Computer Methods in Materials Science*, 11, 68-73.
20. **Sofronis P., McMeeking R.M.** (1992), Creep of power-law material containing spherical voids, *ASME Journal of Applied Mechanics,* 59, S88–S95.
21. **Wonisch A., Kraft T., Moseler M., Riedel H.** (2009), Effect of different particle size distributions on solid-state sintering: A microscopic simulation approach, *J. Am. Ceram. Soc*., 92, 1428–1434.
22. **Zachariah M.R., Carrier M.J.** (1999), Molecular dynamics computation of gas-phase nanoparticle sintering: a comparison with phenomenological models, *Journal of Aerosol Science*, 30, 1139–1151.
23. **Zeng P., Zajac S., Clapp P.C., Rifkin J.A.** (1998), Nanoparticle sintering simulations, *Materials Science and Engineering*, A252, 301–306.
24. **Zhu H., Averback R.S.** (1995), Molecular dynamics simulations of densification process in nanocrystalline materials, *Materials Science and Engineering A*, A204(1-2), 96–100.

Acknowledgements: The results presented in this paper have been obtained within the project "KomCerMet" (contract no. POIG.01.03.01-14-013/08-00 with the Polish Ministry of Science and Higher Education) in the framework of the Operational Programme Innovative Economy 2007-2013.

CFD MODEL OF A MAGNETORHEOLOGICAL FLUID IN SQUEEZE MODE

Bogdań SAPIŃSKI*, MarcinSZCZĘCH*

*AGH University of Science and Technology, Faculty of Mechanical Engineering and Robotics,
al. Mickiewicza 30, 30-059 Kraków, Poland

deep@agh.edu.pl, szczech@agh.edu.pl

Abstract: The study briefly outlines a CFD model of a magnetorheological (MR) fluid operated in squeeze mode with a constant interface area using the CFD (Computational Fluid Dynamics) approach. The underlying assumption is that the MR fluid is placed between two surfaces of which at least one can be subject to a prescribed displacement or a force input. The widely employed Bingham model, which fails to take into account the yield stress variations depending on the height of the gap, has been modified. Computation data obtained in the ANSYS CFX environment are compared with experimental results.

Key words: MR Fluid, Squeeze Mode, CFD Model, Bingham Model

1. INTRODUCTION

MRfluids are heterogeneous suspensions of ferromagnetic particles suspended in a carrier liquid (typically oil or water) whose rheological properties can be controlled through the action of a magnetic field. The fluids can be operated in valve mode, in direct shear/clutch mode or in squeeze mode. When operated in squeeze mode, properties are dependent on application requirements. In the case of vibration damping systems, of particular importance is the ability to generate significant forces when MR fluid is displaced from the squeeze zone and to provide for a wide variability range of rheological parameters. Two cases of squeeze mode operation of MR fluids are considered: with the constant volume or with the constant interface area. Stresses experienced by this fluid when squeezed approach 100-150 kPa with displacements of the orderof several millimeters.

MR fluids operated in squeeze mode experience some characteristic effects, one of them being the displacement of the carrier fluid from squeeze zone. As a result, the properties of the fluid will change during its operation in squeeze mode. Another phenomenon involves the change of the fluid structure: in the presence of a magnetic field, ferromagnetic particles arranged in column-like chain structures get deformed due to compression loading. In the consequence, the MR fluid provides increased resistance to compressive loading and its yield stress tends to increase. Another aspect of the fluid behavior in squeeze mode is the “clumping behavior”(Farjoud et al., 2011) which involves aggregation of fluid particles leading to formation of ferromagnetic particle aggregate clumps in the fluid. As a result, progressively increasing force will develop in consecutive test runs.

One has to bear in mind, however, that until recently literature on the subject would abound in reports on the valve and coupling modes whilst the reports on squeeze mode were but a few. In recent years, however, squeeze mode has received a great deal of attention. The modeling of squeezeing force is investigated inFarjoud et al., (2009) and Horak (2013). However, models presented there are most complicated and hardly applicable in engineering design. This study is focused on the CFD model of MR fluid operated in squeeze mode with the constant interface area (Fig 1). It is assumed that fluid is found in between two parallel surfaces. A widely employed Bingham model has been modified as it fails to take into account the yield stress variations depending on the height of the gap. The numerical calculations were performed in the ANSYS CFX environment (ver. 12). Computation data are compared with experimental results, summarised in Sapiński et al., (2013).

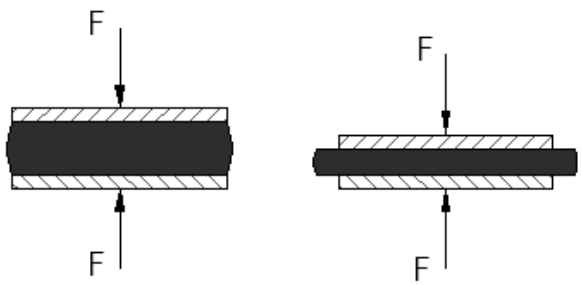

Fig. 1. MR fluid in squeeze mode with the constant interface area

2. MRFLUID MODEL

MR fluids are non-Newtonian, shear-thinned fluids. When exposed to the action a magnetic field, the structure of ferromagnetic particles changes, giving rise to stress. The dynamic viscosity and the yield stress will change, too. To capture the variability of these parameters we rely on the model of apparent viscosity of a MR fluid implemented in the ANSYS CFX environment:

$$\mu_{app} = \frac{\tau_0}{\dot{\gamma}} + \mu \qquad (1)$$

where: μ_{app}– apparent viscosity,τ_0 – yield stress, $\dot{\gamma}$ – shearing rate, μ– dynamic viscosity.

This model has been effectively used in several applications

and theoretical analyses, including (Gavin, 2001; Mazlan, 2008). When the yield stress (dependent on the magnetic field strength) is exceeded, the MR fluid begins to yield. In squeeze mode, the yield stress is also dependent on the height of the fluid gap (Wang et al., 2011).

3. EXPERIMENTS

Squeeze force testing was done in the experimental set-up comprising a rheometer(Salwiński et al., 2013) with a fluid gap, formed by two parallel, flat plates. One of these plates remained immobile whilst the other moved in the progressive-retractivemotion.This configuration is used when testing the properties of magnetic fluids, particularly with the use of Anton Paar-rheometers (http://www.anton-paar.com).

MRfluid selected for testing is the MRF-122G manufactured by the Lord Corporation (http://www.lord.com), which is recommended for use in vibration dampers. Its properties are: density: 2.38g/cm3, saturation magnetization: 359kA/m, volumetric fraction of ferromagnetic particles in the carrier fluid: 22%.

3.1. Test rig

The use of a rheometer enables the magnetic fluids to be investigated when exposed to the magnetic field, both in the shear and squeeze mode. The schematic diagram of the test chamber is shown in Fig. 2.

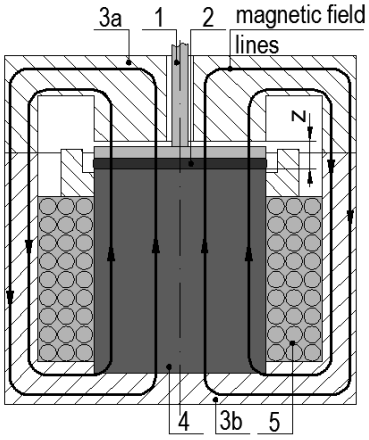

Fig. 2. Schematic diagram of the test chamber: 1−plate, 2−MR fluid, 3a−upper housing, 3b−lower housing, 4−electromagnet core, 5−coil

In the course of the experiment the height of the fluid gap was varied in accordance with the predetermined function governing the plate position (with the use of a step motor). This plate is an element with non-magnetic properties. The accuracy of the plate position measurement was 0.001mm. The squeezing force was measured with a force sensor. Experiments were conducted in thermally-stabilised conditions, the ambient temperature being 25 ^{0}C. Magnetic field was generated by current flowing in the electromagnet windings. The magnetic core and the chamber housing are magnetic circuit components and are made of ferromagnetic materials. Fluid being squeezed was in the lower section of the fluid gap.

The measurement and control system used in the experiments comprised a computer with a card National Instruments USB-6211, supported by the LabView software (version 2009) (www.ni.com). Measurements were taken of the plate position, of velocity of a linear motor, the squeeze force and of temperature inside the test chamber. The measurement and control system was also used to control the intensity of current flowing in the electromagnet coil and the drive of the step motor.

The cross-section of the fluid gap is shown in Fig. 3. The mobile plate was placed between the electromagnet core and the housing with the diameter d=45mm. The gap height z=10mm between the core and the chamber's upper lid allows an unconstrained movement of the plate. The volume of the tested fluid sample was 1.6ml and the initial plate height was h=1mm. The plate's position was varied by Δh=0.2mm and the squeezing time was t=5s.This rheometer configuration ensures an almost uniform magnetic field distribution in the gap.The analysis of the magnetic field distribution in the rheometer used in tests is presented elsewhere (Sapiński et al., 2013).

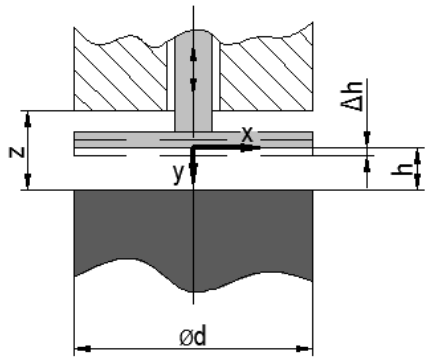

Fig. 3. Gap cross-section in the test chamber

3.2. Results

Experiments were performed for the maximal gap height, under the magnetic field with the flux density B: 70, 100, 140, 200, 270 mT.

The plot of squeezing force in the function of time is shown Fig. 4, for the given initial values of magnetic flux density. The plate's position during the experiments is indicated with the dotted line. The curves obtained for the first two applied excitations B are nearly linear in shape. In the remaining cases (140, 200, 270mT), it appears that the force would increase at a faster rate for Δh from the range (0÷0.03 mm) than (0.03÷0.2mm).

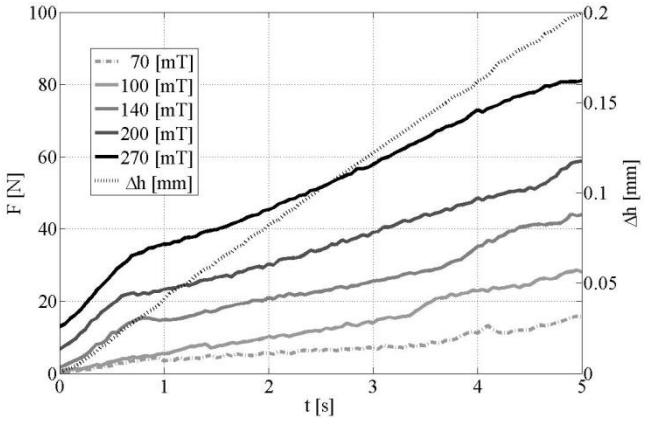

Fig. 4. Squeezing force F and position Δh vs time

For the flux density range (100÷270mT) and for the initial plate position (i.e. for the maximal gap height), a nonzero normal force was registered (Fig. 5). It is the result of pressure generated in the MR fluid under the action of magnetic field, and its value is obtained from the formula (Rosenweig, 1985):

$$p = \mu_0 MH \qquad (2)$$

where: p – pressure, μ_0 – magnetic permeability in the vacuum, M – magnetisation, H – magnetic field strength.

A detailed analysis of this phenomenon is provided in the work (Salwiński and Horak, 2012). This pressure is not considered in rheological models of MRfluids, including the Bingham model adopted by the author.

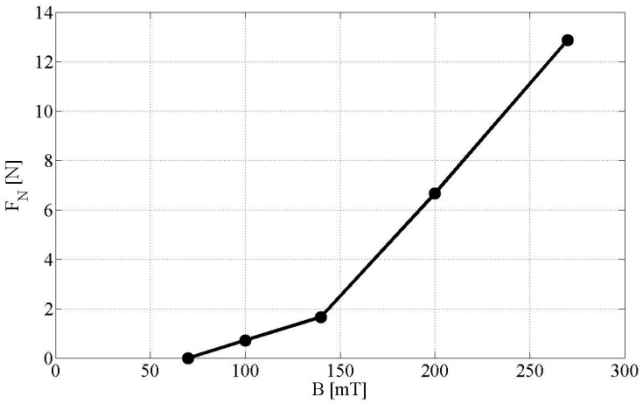

Fig. 5. Normal force F_N vs magnetic flux density B

4. NUMERICAL CALCULATIONS

In the adopted configuration, the distributions of velocity and MR fluid pressures registered in squeeze mode will vary. For that very reason, the squeezing force is not easily defined on the basis of mathematical equations and the numerical procedure was applied instead, using the ANSYS CFX environment (http://www.lord.com). This is a dedicated program for modeling the flows of fluids, gases, mixtures and chemical reactions. The calculation procedure is based on the finite volume method (FVM).

The case considered in this study is axi-symmetrical. To reduce the number of finite elements and to shorten the calculations, the procedure was applied to 1/12th of the entire model (15^0). The symmetry conditions were defined on the edges of the cut-out area. As the rate of changes of the plate's position was rather small, the numerical procedure was restricted to the laminar flow model as no turbulent flows were encountered (Horak, 2013). The finite elements in the modeled system are pyramids with the average height 0.1mm. The numerical simulations neglect the thermal processes in the system (an isothermal system). As the height of the fluid in the gap is rather small (h=1 [mm]), the effects of gravity are neglected. No slip wall boundary conditions were imposed on the upper and lower surfaces, respectively.

Underpinning the CFD simulations is the Bingham model. The plot of measured squeeze forces for B=100mT is shown in Fig. 6, providing also the numerical data obtained for the constant value of yield stress τ_0=10000Pa in the Bingham model. This value was assumed basing on the MR fluid manufacturer's specifications (http://www.lord.com).

The squeezing force determined by the CFD calculations was about 10N and it increased slightly with the elevation of the plate's position. The differences between the calculation and measurement data are significant for an MR fluid in squeeze mode with the constant yield stress. Thus determined squeeze force fails to capture the real behavior of fluid.

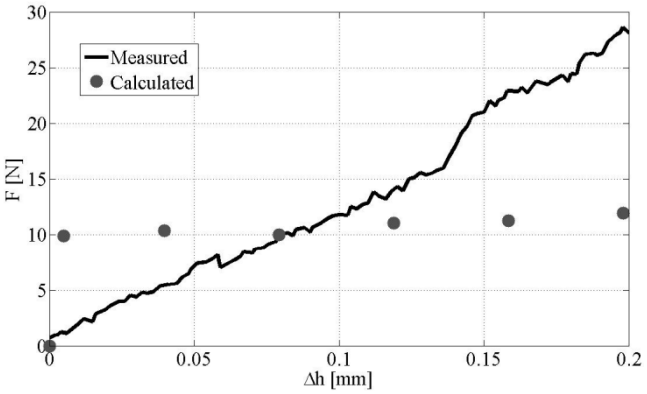

Fig. 6. Squzeeing force F vs position Δh;
magnetic flux density B=100mT, yield stress τ_0= const

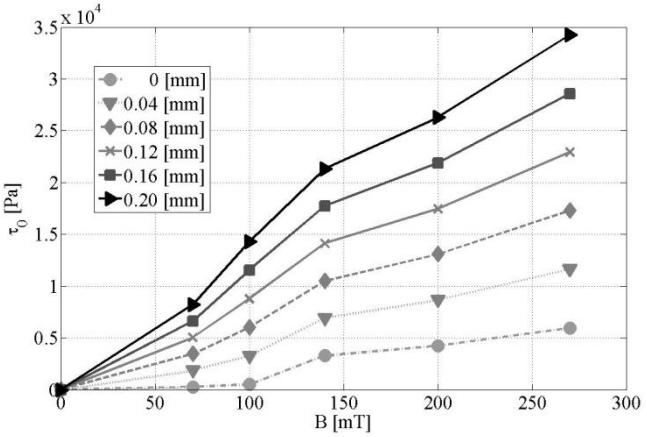

Fig. 7. Yield stress τ_0 vs magnetic flux density B
for various plate positions Δh

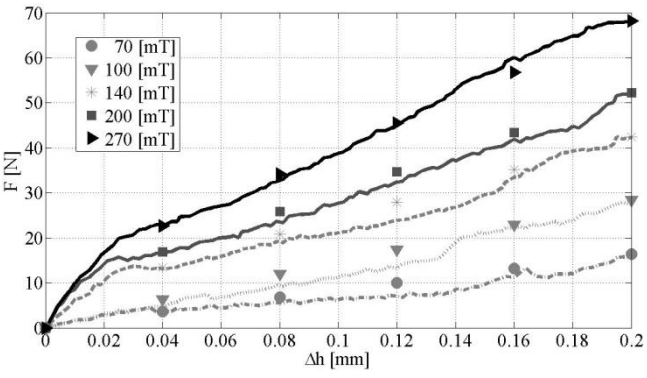

Fig. 8. Squeezing force F vs plate position Δh
for variousmagneticflux density B

The further numerical procedures were applied to ensure a better agreement between the proposed model and experimental data (the determination coefficient being R^2=0.95÷0.99).This coefficient is one of the basic measures of the goodness of fit, widely employed in statistics. It is assumed that in the case considered here the yield

stress of the MR fluid is a function of magnetic flux density and of the plate position Δh. The plot of the yield stress in the function of magnetic flux density and the plate position is shown in Fig. 7.

This dependence was then explored by Bingham model simulations. Comparison of CFD calculation data with experimental results is shown in Fig.8. The numerical simulation data are indicated with markers. It is apparent that in the analyzed cases the numerical model well captures the squeezing force variability.

5. SUMMARY

This study explores the CFD model of a MR fluid, based on the Bingham model whereby the yield stress is dependent on the height of the fluid gap and flux density in the gap. This model may be useful in design of semi-active and passive devices containing MR fluid, which are being investigated by the authors under the current research project.

Experiments results were obtained for a commercially available MR fluid MRF-122EG (manufactured by Lord Corporation), operated in squeeze mode. The relationship was established between the yield stress and the position of the plate. The proposed viscosity model agrees well with experimental data.

The analysis of MR fluid's behavior in squeeze mode is a major challenge for researchers. In the next step the proposed model should be verified under different excitations applied to the plate and for higher values of the magnetic flux density, taking into account other types of fluids and the real MR devices operated in squeeze mode. The current version of the CFD model fails to take into account the extension of fluids. Preliminary results reveal different values of yield stress when squeezed and when under tension.

REFERENCES

1. **Farjoud A., Cavey R., Ahmadian M., Craft M.** (2009), Magnetorheological fluid behavior in squeeze mode, *Smart Materials and Structures*, 18(9), 1-7.
2. **Farjoud A., Craft M., Burke W., Ahmadian M.** (2011), Experimental investigation of MR squeeze mounts. *Journal of Intelligent Material Systems and Structures*, 22:1645–1652.
3. **Gavin HP.** (2001), Mulit-duct ER dampers, *Journal of Intelligent Material Systems and Structures*, 12(5), 353-360.
4. **Horak W.** (2013),Theoretical and experimental analysis of magnetorheological fluids in squeeze mode, *PhD Thesis*, AGH University of Science and Technology, Krakow.
5. **Mazlan S.** (2008), The behaviour of magnetorheological fluids in squeeze mode, *PhD Thesis*, Dublin City University.
6. **Rosensweig R.E.** (1985), Ferrohydrodynamics, Cambridge University Press, Cambridge.
7. **Salwiński J. Horak W.** (2012), Measurement of normal force in magnetorheological and ferrofluid lubricated bearings, *Key Engineering Material, vol. 490, 25-32.*
8. **Salwiński J., Horak W., Szczęch M.** (2013), Experimental apparatus for examination of magnetic fluid lubricated thrust bearing, *XXVI Symposium Fundamentals of Machine Design*, Szczyrk, Poland.
9. **Sapiński B., Horak W., Szczęch M.** (1-4.06.2013), Investigation of MR fluids in the oscillatory squezee mode, *VII –th International Symposium on Mechanics materials and Structures*, Augustow, Poland.
10. **Wang H., Zhang B. J., Liu X. Z., Luo D. Z., Zhong S. B.** (2011), Compression resistance of magnetorheological fluid, *Advanced Materials Research*, 143-144, 624–628.
11. ANSYS Corporation, http://www.ansys.com
12. LORD Corporation, http://www.lord.com
13. Anton-Paar Corporation, http://www.anton-paar.com
14. Labview Corporation, www.ni.com

This research is supported by the National Centre for Research and Development under grant No. PBS 1/A6/3/2012.